EDGE GRADIENT AND SAFETY FACTOR EFFECTS ON ELECTROSTATIC TURBULENT TRANSPORT IN TOKAMAKS

by

ING HWIE TAN

A thesis submitted in partial fulfillment of the
requirements for the degree of

Doctor of Philosophy
(Physics)

at the
UNIVERSITY OF WISCONSIN-MADISON
1992

EDGE GRADIENT AND SAFETY FACTOR EFFECTS ON ELECTROSTATIC TURBULENT TRANSPORT IN TOKAMAKS

Ing Hwie Tan
Under the supervision of Professor Stewart C. Prager
at the University of Wisconsin-Madison

ABSTRACT

Electrostatic turbulence and transport measurements are performed on the Tokapole-II tokamak at the University of Wisconsin-Madison, as the safety-factor (and concomitantly, the energy confinement time) and the edge equilibrium gradients are varied substantially. Tokapole-II is a poloidal divertor tokamak capable of operating at a wide range of safety factors ($<q_a>$ is varied from 1 to 4 in this work) due to its unique magnetic limiter configuration. It also has retractable material limiters in a large scrape-off region, which permits the study of edge boundary conditions like density and temperature gradients. The turbulence is independent of safety factor, but strongly sensitive to the local density gradient, which itself depends upon the limiter configuration. When a material limiter is inserted in a high $<q_a>$ discharge, the density gradient is increased locally (while the temperature gradient remains the same) together with a local increase of the turbulence. On the other hand, limiter insertion in low $<q_a>$ discharges did not increase the density gradient as much, (but in this case increasing the temperature gradient somewhat) and the turbulence properties are unchanged with respect to the magnetic limiter case. It is concluded then, that electrostatic turbulence is caused by the density gradient. Although the electrostatic fluctuation driven transport is enhanced in the large density gradient case, it is in all cases too small to explain the observed energy confinement times. To explore instabilities with small wavelengths, a 0.5 mm diameter spherical Langmuir probe was constructed, and its power compared with the power measured by larger cylindrical probes (3 mm and 1 cm in length). Smaller probes did measure more power than larger ones, but only at higher frequency ranges (f > 500 kHz) and the extra power is too small to contribute significantly to transport.

Acknowledgements

I am glad that my advisors in Brasil convinced me to come to Madison for my Ph. D., despite my fears of spending six months of the year under snow and subfreezing temperatures, in a "tinny little town" of only 200 thousand inhabitants. The cold wasn't that bad after all, and I learned the advantages of living in a smaller community.

I would like to thank my advisor Prof. Stewart Prager, for his guidance and patience. His always positive attitude helped me to achieve the goals of all these years of graduate school. I also want to thank Prof. Richard Dexter for his interest in my work, and his many tips on probe design, specially on miniature probes.

Tokamak research is a team work: I benefited from my colleagues' advice, discussions and friendship. Mike LaPointe taught me almost everything I know about computers. Learning spectral analysis was a lot easier with the help of Dale Graessle and Saeed Assadi. Thanks to David Kortbawi for his help on the electronic circuits, and Trudy Rempel for her advice on Langmuir probes. Ed Haines made the review on η_e modes a lot easier. John Goetz helped to keep Tokapole running for all these years. I would like to thank Dr. Zhaoyuan Ning, for his help during the small spatial scale research. To Kay, Tom Lovell, Jerry Frank, the hackers and all the hourlies, thanks for being there when I needed.

I want to thank CAPES (Scholarship Agency, Brazilian Ministry of Education) for financial support.

This work was supported by the USDoE.

Dedico esta tese `as pessoas responsáveis pela minha perseverança durante todos estes anos de estudo. Aos meus pais estarei sempre em dívida, pela dedicação e amor que sempre me deram. Minhas irmãs tornaram as horas de solidão menos dolorosas pois sempre tive a certeza de que estavam do meu lado. Ao meu querido esposo Alcides, obrigada por tornar estes últimos anos, os melhores da minha vida.

Ao povo brasileiro, agradeço os dólares enviados `as custas de tanto sacrifício. Espero um dia honrar esta dívida, na luta por uma educação mais justa e democrática em nosso pais.

Table of Contents

2. Electrostatic Fluctuations and Transport in Tokamaks

3. Device Description and Diagnostics

4. < q(a) > Scaling of Electrostatic Fluctuations in Tokapole-II

5. Limiter and Edge Gradient Effects on Electrostatic Fluctuations

6. Conclusions for < q(a) > Scaling and Limiter Effects on Electrostatic Turbulence in Tokapole-II

7. Small Spatial Scale Electrostatic Fluctuations in Tokapole-II

7.3 Experimental results

CHAPTER 1

Introduction

Tokamaks are one of the most promising devices for fusion energy generation. One of the major problems in tokamak (and in toroidal devices in general) confinement however, is the observed anomalous electron heat conductivity, which exceeds neoclassical predictions significantly. Classical transport in a tokamak results from Coulomb collisions in straight magnetic field lines. In neoclassical transport field curvatures and gradients increase plasma transport due to particle drifts. Experimental observations however show that electron heat losses are typically two orders of magnitude larger than neoclassical values.[1]

Fluctuations have been the strongest candidate to explain anomalous transport. Electrostatic turbulence can cause transport by **ExB** drifts experienced by the particles in a fluctuating electric field. There is strong evidence for this mechanism in fluctuation induced fluxes measured in edge plasmas, in the vicinity of material limiters. In tokamaks, these fluxes can account for the observed energy loss,[2-5] and in reversed field pinches (RFPs), it explains the observed particle fluxes (although the induced energy flux is small).[6-7] Transport by magnetic fluctuations can arise from particle motion parallel to a fluctuating field, and it can be important in tokamaks at high beta,[8] tokamaks at the L-H transition,[9] and in RFPs.[10]

Edge plasmas are measured to be strongly turbulent, which makes theoretical work very complex. Simplifications not always satisfied experimentally have to be made, so an identification of the instabilities present is very difficult. The most successful theories on electrostatic turbulence are the dissipative drift waves,[11] driven unstable by the density gradient, and the rippling mode,[12] driven unstable by the resistivity gradient.

This thesis is composed of three main parts. First we study the effects of material limiters and edge gradients on electrostatic turbulence. Second, the dependence of electrostatic turbulence on the safety factor is investigated, and third, electrostatic turbulence is studied at spatial scales smaller than those typical of drift waves and rippling modes in order to explore other instabilities.

The importance of edge boundary conditions like the presence of a limiter and changes in the various energy sources (gradient drives) have not yet been studied in detail. In most machines, limiters or divertor plates are always present, and the plasma is close to the vessel walls. Tokapole-II is a poloidal divertor tokamak equipped with retractable limiters, in a scrape-off region (the distance from the separatrix to the vessel wall) about the size of the plasma radius itself. This permits the study of the importance of the presence of a material limiter and the gradients of various edge parameters (which are affected by the limiter) so the energy sources can be investigated. Our results show that in Tokapole-II, electrostatic turbulence is caused by the density gradient. In the magnetic limiter configuration (without material limiters) density and temperature profiles are allowed to slowly decay radially and the turbulence is small, not explaining the observed energy confinement times by at least two orders of magnitude. When a material limiter is inserted the density gradient is increased (the temperature profile is not affected much) causing an increase in the turbulence. When the limiter is inserted without steepening the density profile (and in this case the temperature profile is steepened) at low q_a values, the turbulence characteristics remain as in the magnetic limiter case.

The relative importance of electrostatic and magnetic turbulence is still an open question. Tokapole-II is capable of operating in a wide range of edge safety factors due to its unique magnetic limiter configuration. Previous work on this machine[13] showed a very strong dependence of the magnetic turbulence on the safety factor (q_a): radial magnetic fluctuations increased by two orders of magnitude as the safety factor was decreased from 5 to values below 1, in which case the magnetic turbulence could explain the observed energy confinement times. In RFP's where $q_a << 1$ the energy transport is likely dominated by magnetic turbulence. A q_a scaling study (in the present work q_a is varied from 4 to 1) of electrostatic turbulence in Tokapole-II shows that electrostatic turbulence is independent of q_a, unlike the magnetic case. Although the q_a scan was done only for magnetically limited discharges, we believe the results to be valid also in material limited plasmas, because the insertion of the limiter does not alter the safety factor.

Electrostatic turbulence has been widely studied on spatial scales larger than the ion gyroradius, which are typical scales for drift waves and rippling modes. Theoretical work has been done, however, on smaller scale instabilities like the η_e mode. This instability has wavelengths on the order of the electron gyroradius and some studies suggest the formation of turbulent structures with spatial scales of the size of the plasma skin depth c/ω_{pe} (c is the velocity of light and ω_{pe} is the plasma frequency).[14-15] The dependence of transport coefficients on c/ω_{pe} is particularly attractive because the density dependence agrees with the so-called Alcator scaling for confinement times. To study small wavelength instabilities, miniature Langmuir probes were constructed, and their power compared with larger nearby probes. Although smaller probes do measure more power than larger ones (up to a factor of four in amplitude), this enhanced fluctuation power is very small, occurring only at higher frequencies and certainly not responsible for transport.

This thesis is organized as follows: Chapter 2 gives a review of the present status of electrostatic turbulent transport research in tokamaks, with emphasis on edge measurements and the most successful theories in explaining the experiments. Chapter 3 is a description of the machine and the experimental setup in general: the probes and their circuitry, and the data analysis methods employed. In Chapters 4 and 5 the q_a scaling and limiter effects results are presented. The conclusions on these topics are presented in Chapter 6. Finally, Chapter 7 describes the work done on small spatial scales, with a brief summary on the theoretical work, followed by the results and conclusions.

References

1. Liewer, P., Nuc. Fus. **25** (1985), 543

2. Zweben, S. J., Liewer, P. C., Gould, R. W., J. Nucl. Mater. **111 & 112**(1982), 39

3. Ritz, Ch. P., et al., Phys. Rev. Lett. **62** (1989), 1844

4. Levinson, S. J., Beall, J. M., Powers, E. J., Bengston, R. D., Nuc. Fus. **24** (1984), 527

5. Howling, A. A., Robinson, D. C., in Turbulence and Anomalous Transport in Magnetized Plasmas, Cargese Workshop 1986, edited by D. Gresilon and M. Dubois, p. 115

6. Ji, H., et al., Phys. Rev. Lett. **67**, 62 (1991)

7. Rempel, T. D. et al., Phys. Rev. Lett. **67** (1991), 1438

8. Carreras, B. A. et al., Phys. Rev. Lett. **50** (1983), 503

9. Ohyabu, N. et al., Phys. Rev. Lett. **58** (1987), 120

10. Hutchinson, I. H. et al., Nucl. Fusion **24** (1984), 59

11. Terry, P. W., Diamond, P. H., Phys. Fluids **28** (1985), 1419

12. Callen, J. D., Carreras, B. A., Diamond, P. H., Benchikh-Lehocine, M. E., Garcia, L., Hicks, H. R., in Plasma Physics and Controlled Nuclea Fusion Research (Proceedings of the 9th Int. Conf., Baltimore, 1982), vol. 1, IAEA, Vienna (1983), p. 297

13. Graessle, D. E., Prager, S. C., Dexter, R. N., Phys. Rev. Lett. **62** (1989), 535

14. Horton, W., Hong, B. G., Tajima, T., Comments on Plasma Physics and Controlled Fusion **E 13** (4) (1990), p. 207

15. Bekki, N., Horton, W., Hong, B. G., Tajima, T., Institute for Fusion Studies Report # 264, University of Texas-Austin (February 1989)

CHAPTER 2

Electrostatic Fluctuations and Transport in Tokamaks

In this chapter we will review the status of electrostatic fluctuation research in tokamaks and its important role in the attempt to explain electron anomalous transport. Emphasis will be given to experimental observations in the edge and how they relate to the available turbulence theories.

2.1 Experimental Observations

A complete review of the status of electrostatic fluctuation research and transport in tokamaks is available in the literature in several review articles,[1-4] so only the important and most commonly seen features will be presented here. Emphasis will be given to turbulence in the edge region, rather than in the interior, since the present work is concerned with the edge and scrape-off turbulence in Tokapole-II.

2.1.1 Fluctuation Characteristics

In the range of frequencies $10 \text{ kHz} < f < 1 \text{ MHz}$, most machines have very large (20 to 100%) turbulent density and potential fluctuations in their edge regions.[5-14] The turbulent nature can be seen in the fact that the fluctuations are broadband ($\Delta\omega/\omega \sim \Delta k_\theta/k_\theta \sim 1$) and have very short autocorrelation times (~ 10 μsec.). Perpendicular wavenumbers are in the range $k_\theta \sim$ (1-3) cm^{-1} which corresponds to poloidal mode numbers m ~ 50. Some measurements show that $k_\theta \rho_s \sim$ (0.05 - 0.1) where ρ_s (typical scale length for drift waves) is the ion gyroradius calculated with the electron temperature. The fluctuations are not quite isotropic[9] : $k_r < k_\theta$, $\Delta k_r \sim 2\Delta k_\theta$. Parallel wavenumbers are much smaller $k_{//} \sim$ (0.0005 - 0.01) cm^{-1}. Poloidal correlation lengths are of the order of 1 cm. The frequencies and wavenumbers observed are in the range expected for drift waves, which are driven unstable by the density gradient.

The fluctuation levels are slightly higher but on the order of drift wave mixing level estimates which predicts that saturation should be reached when the density gradient drive is flattened by the turbulence (the turbulence mixes over the gradient scale length), or $\tilde{n}/n \sim (1/k_r L_n)$, where L_n is the density gradient scale length, k_r is the radial wavenumber and $\tilde{n}/n$ is the density fluctuation level.[4] The radial dependence of density and potential fluctuations often shows a non-Boltzmann behavior i.e., $\tilde{n}/n \neq \tilde{V}_p/T_e$ where Vp is the plasma potential and T_e is the electron temperature. While the density fluctuations increase with radius, the opposite is seen for the potential fluctuations. Although there is only a weak constraint with turbulent theories, it is worth mentioning that the spectral slopes observed are: [4] $\tilde{\Phi}^2 \; \alpha \; f^{-(2-4)}$, $\tilde{n}^2 \; \alpha \; k^{-(3-4)}$.

The poloidal phase velocities of the turbulent waves ($v_{ph} = \omega/k$) are on the order of several km/sec. They propagate in the electron diamagnetic drift direction just inside the limiter (edge region) and reverse to the ion direction in the scrape-off layer. This observation is consistent with waves propagating with the electron diamagnetic drift, Doppler shifted by an $E_r x B_T$ drift in the ion direction:[9] $v_{ph} = v_{de} - v_{ExB}$. The region of reversal is often called the velocity shear layer, and is coincident with the position where the plasma potential has a maximum. The radial electric field in this layer thus changes sign, changing the direction of the ExB drift and the observed phase velocities. The characteristics of the turbulence in the velocity shear layer is somewhat different than on either side: the turbulence is isotropic in the perpendicular directions.[15]

2.1.2 Transport Measurements

Electrostatic fluctuation driven particle flux occurs when density fluctuations correlate with fluctuating radial $\tilde{E}_\theta x B_T$ velocities caused by potential fluctuations: $\Gamma = <\tilde{n} k_\theta \tilde{V}_p>/B_T$ where < > denotes an ensemble averaging process. Maximum radial flux is obtained if density and electric field fluctuations are in phase, (or density and potential fluctuations are 90 degrees out of phase) and if they are perfectly correlated. The phase angles measured in most machines are close to the optimum value (70-90 degrees between density and potential), but coherencies are of the order of 0.5. Assuming poloidal symmetry, the fluctuation-induced particle flux can be determined at a single position and compared with particle balance measurements and calculations.

Although error bars are often large and poloidal asymmetries are sometimes detected, both confinement times agree, so it is believed that anomalous particle flux is due to electrostatic fluctuations.[16-18] The diffusion coefficient calculated with the fluctuation driven fluxes were on the order of the Bohm diffusion coefficient. In auxiliary-heated machines, degradation in confinement is associated with an increase in turbulence levels in the L-mode.[4]

The electron energy flux associated with electrostatic fluctuations is given by $q_e = (3/2B)\langle\tilde{p}\tilde{E}\rangle$ where $\tilde{p} = (\tilde{n}K_BT_e + nK_B\tilde{T}_e)$, B is the magnetic field and K_B is the Botzmann constant. Electron temperature fluctuations are experimentally difficult to measure but they have been estimated in many machines to be small compared to density fluctuations[19-20] (typically $\tilde{T}_e/T_e \sim (10\text{-}15)\%$). It has been neglected in the calculation of density and potential fluctuations (when Langmuir probes are used) although the issue is still being debated. Comparison of the heat loss due to convected energy fluxes $q_{econv} = (3/2)K_BT_e\Gamma$ with the heat loss calculated from power balance indicates that at least 50% of it could be accounted for by electrostatic turbulence, or even all of it considering the large error bars. Conducted energy loss $q_{econd} = (3/2)nKB\langle\tilde{T}_e\tilde{E}\rangle$ accounts for about 20% of the total.[16]

There has been an increasing interest in the influence of radial electric fields and velocity shear on edge transport. Recent experiments on the DIII-D tokamak[21] showed an increase of plasma flow and a more negative radial electric field preceding the L-H transition. Experiments with biased limiters in the CCT tokamak[22] showed that negative electric fields in the edge (enhancing the potential well which naturally occurs inside a tokamak plasma) improved the confinement. In TEXT[23], the particle flux and diffusion coefficient are decreased in the shear layer where the radial gradient of E_r and thus the velocity shear is high.

Tokamaks do not have to be necessarily turbulent. A case of nonturbulent plasma was reported on the Caltech tokamak[7] (fluctuation levels smaller than 3%), but for very high filling pressures, low temperature and low plasma current. In the TEXT tokamak at low average densities [24] ($n < 2 \times 10^{13}$ cm^{-3}) only 15% of the energy losses are estimated to be from convection due to electrostatic turbulence.

2.2 Theoretical Models

Table 2.1 (taken from reference 1) shows a classification of some of the available theories to explain anomalous transport in tokamaks. The modes are classified according to their scale length (macroscopic or microscopic), source of free energy and the set of equations used to describe them. An additional classification should be made (not shown in the table) identifying the magnetic or electrostatic character of the instability.

Macroscopic modes are usually not invoked to explain anomalous transport in most machines since although they can affect the global plasma parameters, they do not affect the confinement times, unless they are very large (causing disruptions for example).

Table 2.1

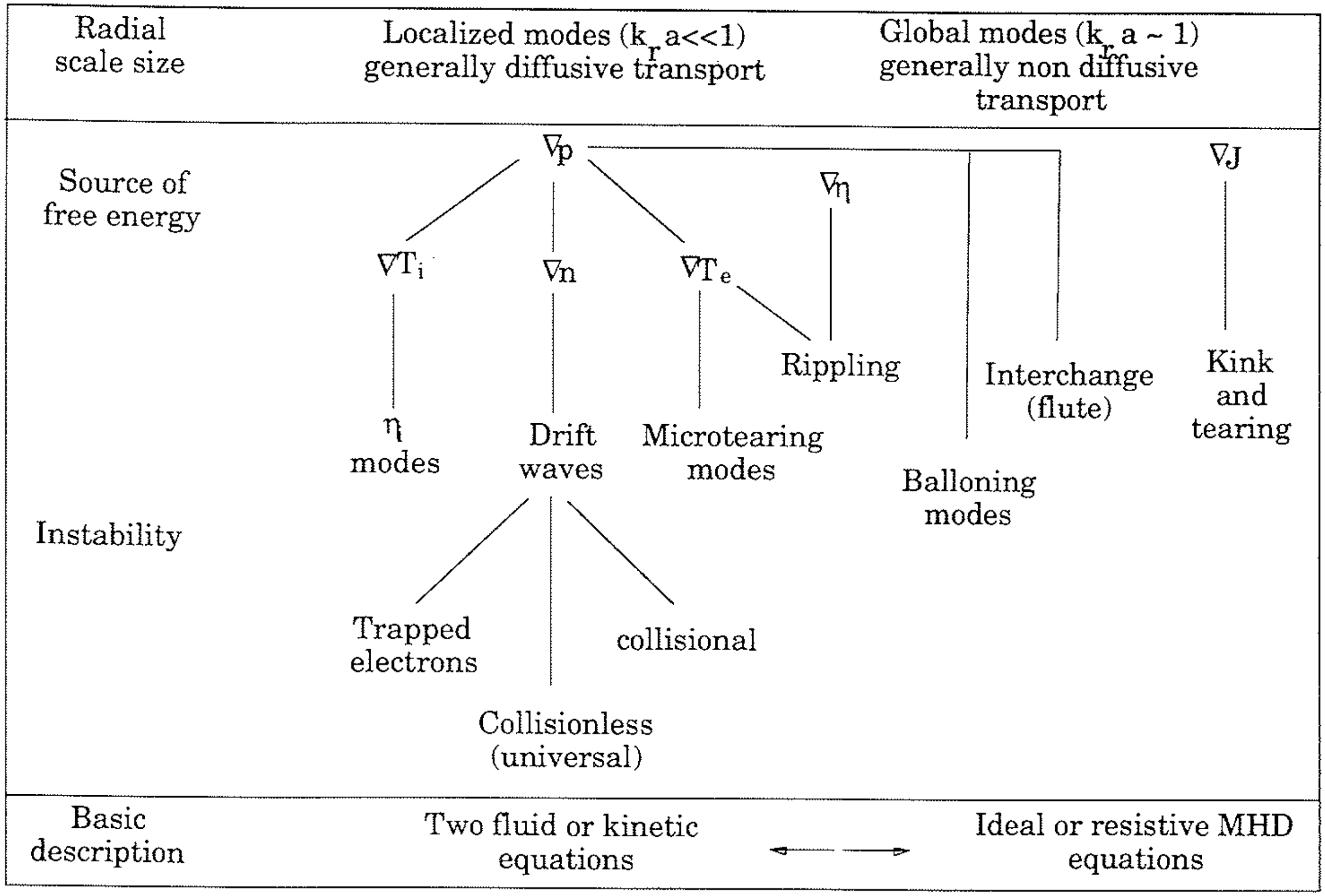
Radial scale size
Localized modes ($k_r a << 1$) generally diffusive transport
Global modes ($k_r a \sim 1$) generally non diffusive transport
Source of free energy
∇p
∇T_i
∇n
∇T_e
$\nabla \eta$
∇J
Instability
η modes
Drift waves
Microtearing modes
Rippling
Interchange (flute)
Balloning modes
Kink and tearing
Trapped electrons
Collisionless (universal)
collisional
Basic description
Two fluid or kinetic equations
Ideal or resistive MHD equations

Microscopic instabilities are believed to be responsible for anomalous transport. The highly turbulent state detected experimentally indicates that it is a state of strong nonlinear mode couplings. In weak plasma turbulence theory the low amplitudes permit the nonlinearities to be treated perturbatively. This cannot be done in strong turbulent plasmas: the nonlinearities are treated numerically or analytically with renormalization techniques. Renormalization techniques are very complex and only recently have been incorporated in the study of plasma turbulence.[1] In this theory, nonlinear mode couplings are replaced by operators representing the average effects of the plasma response to the turbulence. The plasma response is divided into coherent and incoherent parts. In coherent renormalized theories the incoherent part is neglected (this is valid for $\Delta\omega << \omega$). In the more general renormalized theories the incoherent part is taken into account, enabling the calculation of the spectral distribution function of the fluctuations $S(k,\omega)$. Since this is equivalent to finding the two point correlation function, the theory is often called the two point renormalized theory, unlike the coherent theory which is called a one point theory.

The complexity of the analysis forces the introduction of approximations not always valid experimentally. Furthermore, the addition of physical processes other than the free energy sources (like velocity shear or radiation) can affect the results significantly. Therefore, although a particular theory may fail to explain experimental observations, it does not mean that the original mode or instability drive can be totally eliminated.

The most successful theories in explaining turbulence in the rather collisional edge regions of a tokamak are based on the dissipative density gradient driven (collisional drift waves) and the resistivity gradient driven modes (rippling modes). Drift waves have for a long time been the most invoked instability to explain edge turbulence in tokamaks. It is driven unstable by the density gradient present in edge plasmas. Extensive reviews are available in the literature.[25-26] The broad spectra of the fluctuations ruled out simple weak turbulence theories. A simple two-dimensional non-linear fluid model for strong drift wave turbulence was derived by Hasegawa and Mima.[27] Although it is a collisionless model it predicted broad frequency and wavenumber spectra consistent with observations of density fluctuations in the TCA tokamak.[5]

Collisional theories are more appropriate in the edge and many authors have been partially successful in describing experimental observations. Hasegawa and Wakatani[28] derived model mode-coupling fluid equations for resistive drift-waves and solved them numerically, obtaining fluctuation levels $\tilde{n}/n \propto (\rho_s/L_n)^{1/2}$ and Bohm-type diffusion coefficients $D \sim T_e/eB_0$ with particle flux $\Gamma \propto T_e(dn/dr)/B_0$. Waltz and Dominguez[29] also applied numerical methods (using the Direct Interaction Approximation) to solve an electrostatic kinetic drift wave turbulence model which included wave-wave and wave-particle interactions in a sheared-slab geometry. They found that the fluctuation levels should saturate at the mixing level estimates $\tilde{n}/n \sim 1/(k_r L_n)$ where k_r is the dominant wavenumber with $k_r \rho_s \sim 0.3$ and the frequency spectral widths were finite but slightly smaller than those observed experimentally.

Terry and Diamond[30] developed a two-point renormalized theory of collisional drift wave turbulence which showed several features in agreement with experiment. Instead of treating the turbulence state as a collection of waves or eigenmodes they viewed it as a "soup" comprised of waves and density blobs resembling eddies. Experimentally, these density structures (blobs) would have lifetimes longer than the average correlation times. Blob like structures were observed in the Caltech tokamak[31] using a two dimensional array of Langmuir probes but could not be identified with any particular theory . They were able to solve the equations analytically in the low Reynolds number regime (a parameter indicating the relative strength between ExB convection and parallel collisional diffusion) in which many weak turbulence approximations were made ($\Delta\omega < \omega$). For large Reynolds numbers, quantitative results were not obtained, but using strong turbulence arguments they were able to infer some properties which were consistent with an extrapolation of the low Reynolds number solutions. For this regime the results showed a broad frequency spectrum with energy concentrated in low wavenumbers ($k_\theta \rho_s \sim 0.1$), fluctuation levels at $e\tilde{\phi}/T_e \propto \rho_s/L_n$, diffusion coefficient $D \sim \rho_s^2 c_s/L_n$ (or $D \propto T_e^{3/2}/B^2 L_n$, c_s is the ion sound speed) and particle flux $\Gamma \sim \rho_s^2 c_s/L_n^2$.

Drift wave models fail to explain the non-Boltzmann behavior and the phase angle between density and potential fluctuations, as well as their radial dependence.[4] Perhaps the strongest candidate for explaining edge turbulence is the resistivity gradient driven rippling modes. Linear, quasilinear and nonlinear regimes of this mode, were studied numerically by Callen et al.[32] and Carreras et al.,[33] reaching good agreement with radial and poloidal correlation and k-spectra measurements in the Macrotor tokamak[6] but predicted lower fluctuation levels than observed experimentally. The MHD rippling mode is a moderate m (m~ 5-20) mode driven unstable by a resistivity or electron temperature gradient when a plasma current flows along the magnetic field line. Parallel electron thermal conductivity partially stabilizes the mode because the resistivity fluctuation would be short-circuited by fast parallel transport, reducing its growth rate and radial extent. Saturation occurs by flattening of the resistivity profile. It is a predominantly electrostatic mode although there is a small magnetic component that creates magnetic islands localized in the rational surface, while the electrostatic perturbation is displaced relative to this surface to the region of higher resistivity.

The fully nonlinear saturated turbulent state was found to be different in character from the linear regime in a one-point renormalized theory developed by Garcia et al.[34] They stress the importance of turbulent stabilization with saturation obtained with the balance between the resistivity gradient drive and dissipation caused by parallel thermal conduction when the turbulent diffusion is large. This saturation mechanism (rather than the resistivity gradient flattening) raised the fluctuation level prediction closer to experimental values. Fluctuation levels and transport coefficients are also insensitive to the thermal conductivity which is contrary to the linear theory. Also, in the linear theory the eigenmodes are skewed to one side of the rational surface; in the fully turbulent state this asymmetry is accentuated so that the current fluctuations decouple from the potential and resistivity fluctuations eliminating the vorticity equation. A two-point renormalized calculation by Terry et al.,[35] corroborated the one-point theory and gave further estimates of spectral properties.

Hahm et al.[36] included the effect of impurity density gradient in addition to the temperature gradient in the calculation of the resistivity gradient. Contrary to the temperature, Z_{eff} can peak either on axis or in the edge, and thus can either oppose or enhance (in the edge peaked case) the temperature drive. Fluctuation levels and transport coefficients were derived and were in good agreement with experiments on TEXT,[16] Caltech[17] and Tosca[10] tokamaks, with thermal transport dominated by convection. This theory was successful also in predicting a non adiabatic response of density and potential fluctuations, which is observed experimentally.

A further refinement of the theory was the inclusion of radiative cooling due to the impurities[37] present in edge plasmas, where the radiation rate slope as a function of temperature is negative ($dI_Z/dT < 0$). A negative temperature perturbation will increase the radiation rate due to an increase in the density (assuming constant pressure). The temperature is decreased further causing the instability. This instability is sometimes called "thermal condensation". Analysis showed that fluctuation levels and transport are enhanced for high density machines. Interestingly, the impurity radiation enhancement tends to force the potential fluctuations to be greater than the density fluctuations as observed experimentally in the scrape-off regions. The particle diffusion coefficient also showed a reduced sensitivity to the loop voltage, unlike the basic resistivity gradient model. This could explain the high levels of turbulence in currentless stellarators and tokamak edge plasmas where $J_{//}=0$.

One of the biggest challenges to transport theories is the understanding of the physics of the L-H transition, and the formation of a transport barrier at the plasma edge. Recent experiments in DIII-D,[21] CCT[22], TEXT[23] and TEXTOR[45-46] tokamaks indicate a relationship between poloidal rotation and confinement. Shaing et al.[38] studied the effect of radial electric fields on resistivity-gradient-driven turbulence and found that the saturation levels were lower for a more negative value of E_r. Biglari et al.[39] considered the same question but emphasized the shear of the electric field (and thus sheared poloidal rotation). They found that it was the dominant mechanism of turbulence suppression (by fissuring large turbulent structures and thus enhancing decorrelation) and it was independent of the sign of either E_r or its shear. Kim et al.[40] calculated these effects on resistivity gradient driven turbulence. Both theories (increase in radial electric field and increase in its shear) are consistent with experimental observations. In DIII-D an increase in the negative radial electric field (which caused an increase in the poloidal rotation) and its shear is seen before the L-H transition. In CCT where an H-mode is triggered by biasing a limiter to large negative values (forcing a negative radial electric field at the edge) the same effects are seen. In TEXTOR both negative and positive electric fields can trigger an H-mode. The effects of sheared poloidal rotation was seen on TEXT where an improvement in confinement is seen in the velocity shear layer.

References

1. Liewer, P., Nuc. Fus. **25** (1985), 543

2. Robinson, D. C., in Turbulence and Anomalous Transport in Magnetized Plasmas, Cargese Workshop 1986, edited by D. Gresilon and M. Dubois, p.21

3. Surko, C. M., in Turbulence and Anomalous Transport in Magnetized Plasmas, Cargese Workshop 1986, edited by D. Gresilon and M. Dubois, p.93

4. Wootton, A. J., et al., Phys. Fluids B **2** (1990), 2879

5. Mazzucato, E., Phys. Rev. Lett. **36** (1976), 792

6. Zweben, S. J., Taylor, R. J., Nuc. Fus. **21** (1981), 193

7. Zweben, S. J., Gould, R. W., Nuc. Fus. **23** (1983),1625

8. Levinson, S. J., Beall,J. M., Powers, E. J., Bengston, R. D., Nuc. Fus. **24** (1984), 527

9. Ritz, Ch. P., Bengston, R. D., Levinson, S. J., Powers, E. J., Phys. Fluids **27** (1984), 2956

10. Howling, A. A., Robinson, D. C., in Turbulence and Anomalous Transport in Magnetized Plasmas, Cargese Workshop 1986, edited by D. Gresilon and M. Dubois, p. 115

11. Rudyj, A., et al., 17th EPS Conf. on Controlled Fusion and Plasma Heating, Amsterdam **14B** (1990), p. 1464. See also Bengston, R. D., et al., ibid, p. 1460

12. Vayakis, G., Ph.D. Thesis Univ. of Oxford 1991

13. Komori, A., et al., Nuc. Fusion **28** (1988), 1460

14. Stockel, J., et al., in Plasma Physics and Controlled Nuclear Fusion Research (Proceedings of the 12th Int. Conf., Nice 1988) (Vienna IAEA, 1989), p. 359

15. Ritz, Ch. P., et al., Nuc. Fusion **27** (1987), 1125

16. Ritz, Ch. P., et al., Phys. Rev. Lett. **62** (1989), 1844

17. Zweben, S. J., Liewer, P. C., Gould, R. W., J. Nucl. Mater. **111 & 112** (1982), 39

18. Rowan, W. L., et al., Nucl. Fusion **27** (1987), 1105

19. Liewer, P. C., et al., Phys. Fluids **29** (1986), 309

20. Lin, H., Bengston R. D., Ritz, Ch. P., Phys. Fluids B **1** (1989), 2027

21. Groebner, R. J., Burrell, K. H., Seraydarian, R. P., Phys. Rev. Lett. **64** (1990), 3015

22. Taylor, R. J., et al., Phys. Rev. Lett. **63** (1989), 2365

23. Ritz, Ch. P., Lin, H., Rhodes, T. L., Wooton, A. J., Phys. Rev. Lett. **65** (1990), 2543

24. Ritz, Ch. P., et al., J. Nuc. Mater. **145** & **147** (1987), 241

25. Horton, W., in Basic Plasma Physics, II, edited by A. A. Gallev and R. N. Sudan, (North Holland, Amsterdam, 1985), p. 383

26. Kadomtsev, B. B., Pogutse, O. P., in Reviews of Plasma Physics (Leontovich, M. A., Ed.), vol. 5, Consultants Bureau, New York (1970), 249

27. Hasegawa, A., Mima, K., Phys. Fluids **21** (1978), 87

28. Hasegawa, A., Wakatani, M., Phys. Rev. Lett. **50** (1983), 682

29. Waltz, R. E., Dominguez, R. R., Phys. Fluids **26** (1983), 3338

30. Terry, P. W., Diamond, P. H., Phys. Fluids **28** (1985), 1419

31. Zweben, S. J., Phys. FLuids **28** (1985), 974

32. Callen, J. D., Carreras, B. A., Diamond, P. H., Benchikh-Lehocine, M. E., Garcia, L., Hicks, H. R., in Plasma Physics and Controlled Nuclear Fusion Research (Proceedings of the 9th Int. Conf., Baltimore, 1982), vol. 1, IAEA, Vienna (1983), p. 297

33. Carreras, B. A., Gaffney, P. W., Hicks, H. R., Callen, J. D., Phys.Fluids **25** (1982), 1231

34. Garcia, L., Diamond, P. H., Carreras, B. A., Callen, J. D., Phys. Fluids **28** (1985), 2147

35. Terry, P. W., Diamond, P. H., Shaing, K. C., Garcia, L., Carreras, B. A., Phys. Fluids **29** (1986), 2501

36. Hahm, T. S., Diamond, P. H., Terry, P. W., Garcia, L., Carreras, B. A., Phys. Fluids **30** (1987), 1452

37. Thayer, D. R., Diamond, P. H., Phys. Fluids **30** (1987), 3724

38. Shaing, K. C., Lee, C. S., Carreras, B. A., Houlberg, W. A., Crume Jr., E. J., in Proceedings of the 12th Int. Conf.on Plasma Phys. and Cont. Nuc. Fus. Res., Nice, 1988 (IAEA, Vienna, 1989)

39. Biglari, H., Diamond, P. H., Terry, P. W., Phys. Fluids B **2** (1990), 1

40. Kim, Y. B., Diamond, P. H., Biglari, H., Terry P. W., Phys. Fluids B **2** (1990), 2143

41. Wootton, A. J., FRCR # 393, Univ. of Texas Austin, 1991

42. Graessle, D. E., Prager, S. C., Dexter, R. N., Phys. Fluids B **3** (1991), 2626 . See also
Graessle, D. E., Prager, S. C., Dexter, R. N., Phys. Rev. Lett. **62** (1989), 535

43. Rempel, T. D., et al., Phys. Rev. Lett. **67** (1991), 1438

44. Toyama, H. J., et al., Phys. Rev Lett. **67** (1991), 62

45. Weynants, R. R., et al., Proc. of the 17th. EPS Conference on Controlled Fusion and Plasma Heating. Amsterdam, June 1990, p.287

46. Nieuwenhove, R. Van, et al., Proc. of the 18th. European Conference on Controlled Fusion and Plasma Physics, Berlin, June 1991, p. I-405.

CHAPTER 3

Device Description and Diagnostics

This chapter describes the experimental procedures. The experiments were performed in the Tokapole-II tokamak, a small iron-core tokamak, built at the University of Wisconsin-Madison. A brief description of the machine and its main diagnostics are given first. The spectral analysis techniques utilized for the analysis of electrostatic fluctuations and their consequence on transport are then described. The Langmuir probes used for correlation and transport studies, small spatial scale studies and the admittance probe are described last, together with their electronic apparatus.

3.1 Tokapole-II

3.1.1 Machine Description

Since it began operation in 1978 until this last thesis, there has been numerous articles and theses describing Tokapole-II, so only a brief description of the machine will be given here. Further details of machine construction, operation, plasma formation and discharge conditions can be found in references 1 to 6.

Tokapole-II is a four node poloidal divertor tokamak. Its vacuum

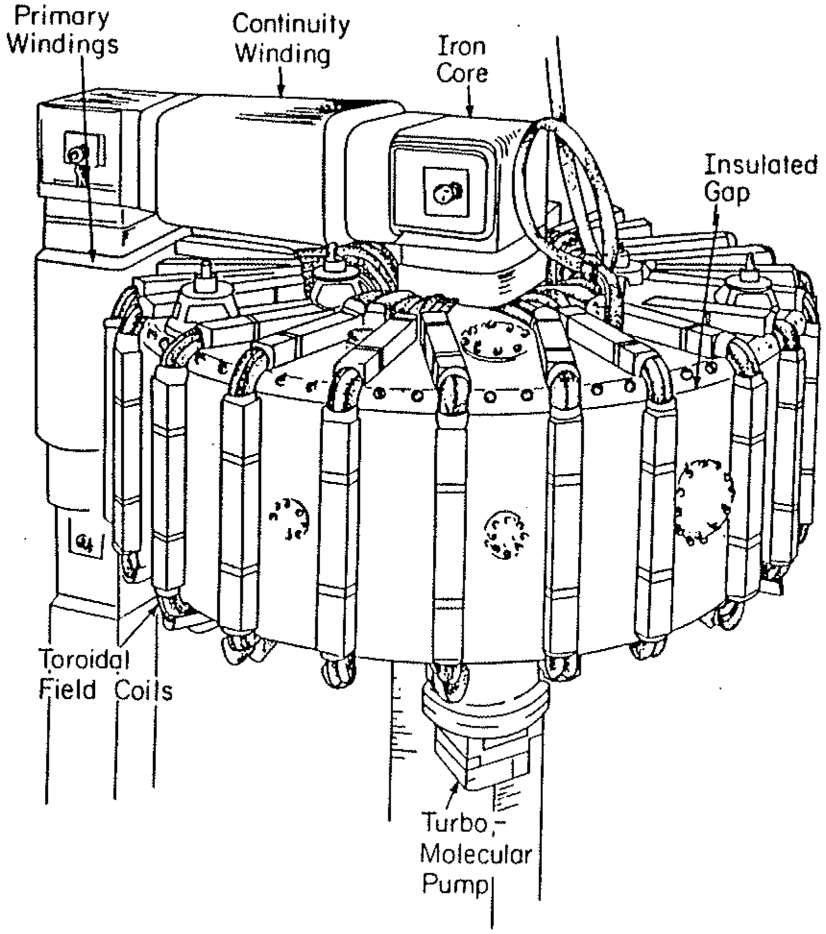

Fig. 3.1 The Tokapole-II tokamak.

vessel is made of aluminum, with 3 cm thick walls. It has a 44 cm x 44 cm square cross-section and a 50 cm major radius. There are insulated poloidal and toroidal gaps to ensure field penetration. The divertor field is generated by the inductively driven currents in four toroidal rings. Since a 1987 upgrade,[7] each chromium copper ring is supported at three points with Inconel rods (originally beryllium copper), and is capable of carrying 200 to 500 kiloAmps of current.

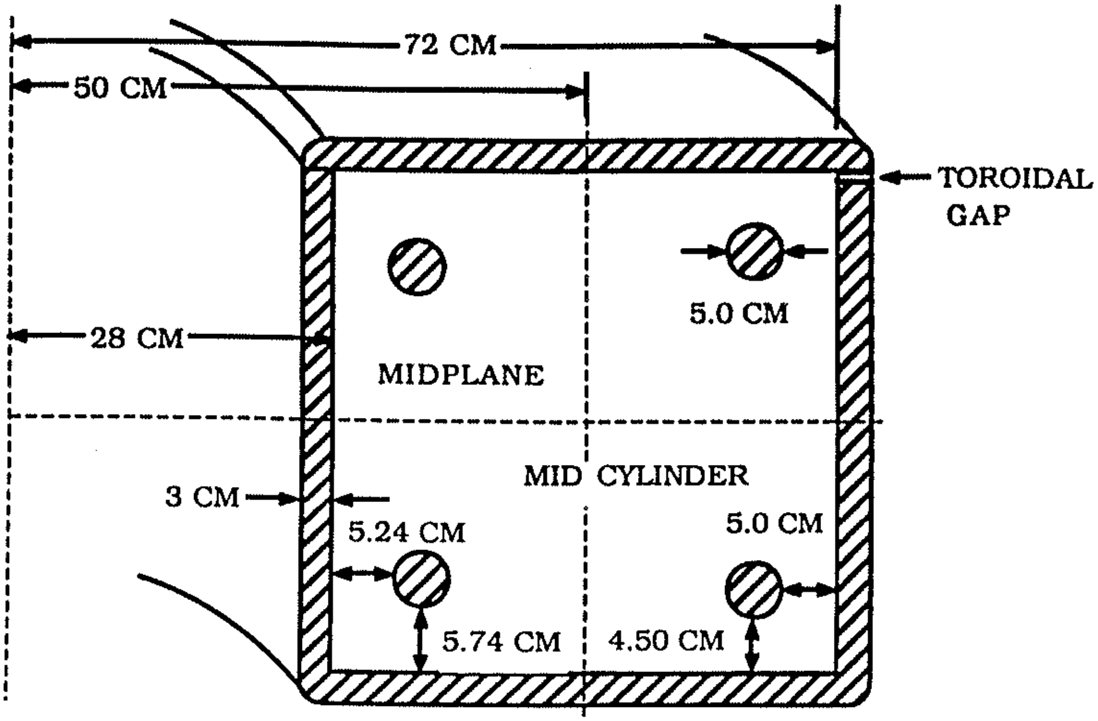

Fig. 3.2 Poloidal cross section of Tokapole-II vacuum vessel.

Figures 3.1 and 3.2 show a picture of the machine and the dimensions of its cross-section. A turbomolecular pump with a 1500 l/sec pumping speed, keeps base pressures in the mid 10^{-7} torr range. Better vacuum qualities (about a factor of two reduction in base pressures) can be achieved with titanium gettering.

The toroidal field is generated by firing a 78 mF, 5 kV capacitor bank through a winding system of 96 turns of 4/0 cable (actually four, 24 turn windings are driven in parallel). The banks are fired through a class E ignitron, and are passively crowbarred through another ignitron triggered at peak field, giving a flat field for about 10 ms. Maximum fields of about 7 kGauss could be achieved at full bank voltages, but in normal operations, toroidal fields of 5.5 kGauss or less were used.

The poloidal field system consists of an iron core transformer system (with a total flux swing of 0.17 V.sec.) in which the plasma current and the rings are the secondary windings. The primary winding consists of 80 turns of two gauge wire wound around the core so that the system runs with a 40:1 turns ratio. A 7.5 mF, 5 kV capacitor bank is fired to the primary winding through an ignitron, and the system is actively crowbarred using an electrolytic bank of 960 mF, 450 V. An optional damping resistor can be used in the circuit to give longer discharges, but lower peak currents.

The poloidal field configuration is illustrated in figure 3.3. Without a plasma current, the four ring currents generate an octupole field as shown in figure 3.3a. When the plasma is formed, a poloidal field is generated which, combined with the octupole field, results in the configuration shown in figure 3.3b. A separatrix with four x-points is formed. This surface, separates six distinct flux contour regions : four encloses a single ring current, one encloses the main plasma only (these five are called private fluxes), and one encloses all currents (the common flux). The common flux region is often called the scrape-off region, since the lines of force are interrupted by the rings' support rods.

There are four removable stainless steel limiter plates on each side of the square cross section at one toroidal location (figure 3.3b shows their location when they are inserted). They can be swiveled into the

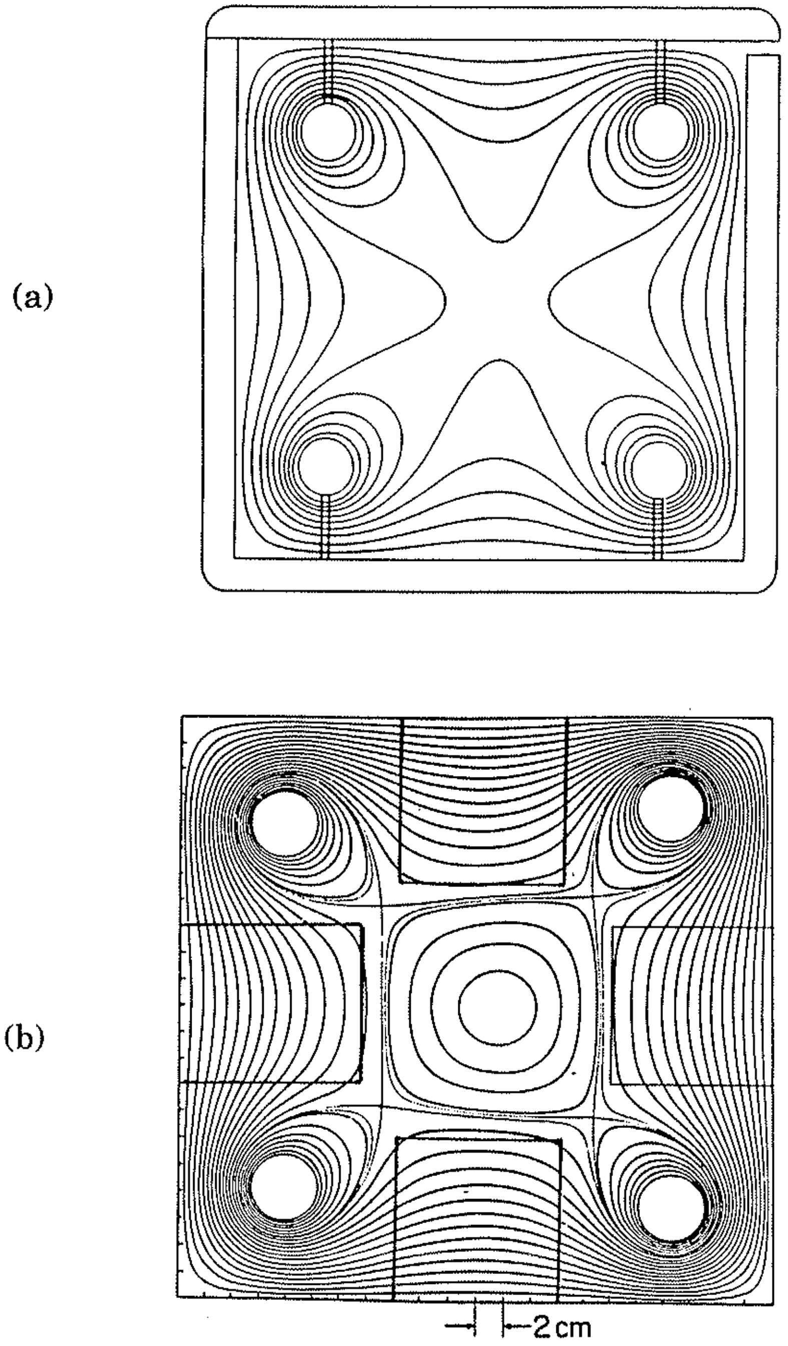

Fig. 3.3 Poloidal field flux plots: (a) octupole field due to ring currents only, (b) poloidal field with plasma current present.

discharge beyond the separatrix location, or can be retracted to the wall. When the limiters are not inserted the main central plasma is said to be magnetically limited by the separatrix, as opposed to material limited plasmas, when one or more plates are inserted.

The working gas used in Tokapole is hydrogen, which is puffed into the machine using a piezoelectric valve. Pre-ionization electrons are supplied by a fast ion gauge, and three sources of microwaves: a 100 W cw S-band (2.45 GHz), and a 10 kW pulsed X-band (9.0 GHz) or K-band (16.5 KHz), depending on the toroidal field strength. To ensure enough time for diffusion, hydrogen is puffed into the machine 16.7 ms before the ohmic banks are fired. The toroidal field is initiated 7.6 ms later so that it reaches the plateau when the main plasma is formed. Between the initiation of the toroidal field and the main plasma, the microwave sources are fired.

3.1.2 General Diagnostics

Due to the presence of the rings, routine tokamak diagnostics like plasma current, loop voltage, radius etc., cannot be directly measured. Instead, an electronic circuit model is used,[4] and these quantities are derived from two direct measurements: the poloidal gap voltage (measured with a single turn flux loop) and the primary current (measured with a 1 mΩ shunt). Details of the model assumptions can be found in reference 4 and 5. Assuming that the plasma current can be treated as if it was all concentrated in the geometric axis and using the circuit model of figure 3.4, the plasma current is given by:

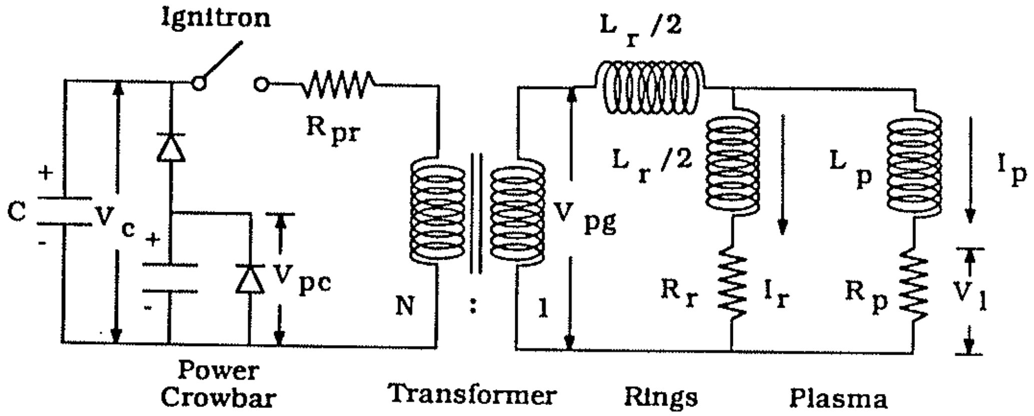

Fig. 3.4 Circuit model (from reference 4) to model Tokapole-II

$$I_p = \frac{N}{\alpha} I_{pr} - \frac{1}{\alpha L_r}\int V_{pg} dt + \frac{1}{\alpha L_r}\int I_r R_r dt \qquad I_r = N I_{pr} - I_p \tag{3.1}$$

where α = private flux/common flux in the absence of plasma (~ 0.5), N is the primary turns ratio (40), I_{pr}, I_p, I_r are the primary, plasma and ring currents in kiloAmps, R_r and L_r are ring resistance (in ohms) and inductance (in henrys), and V_{pg} is the poloidal gap voltage in volts. This equation is solved with an analog circuit and have been shown to agree with direct ring current measurements to within 25 %.

Once I_p is known, other quantities can be deduced, following certain assumptions. The plasma radius can be calculated assuming that all the current is uniformly distributed within the separatrix with a circular cross section having the same area as the area within the separatrix:

$$a = 17.4 \left| I_p/(I_p + I_r) \right|^{1/4} \text{ (in cm)} \qquad (3.2)$$

With these assumptions, the effective edge safety factor is:

$$q_a = 10^{-4} a^2 B_T / I_p \qquad (3.3)$$

where B_T is the toroidal field in gauss.

Using the same circuit model of figure 3.4, and experimental values of plasma and ring inductance, the loop voltage (calculated at the magnetic axis), is given by:

$$V_l = 0.5(1 + t/75)V_{pg} + 0.0045(1 - t/37)I_r - \frac{2.3}{\sqrt{a}}\frac{dI_p}{dt} \qquad (3.4)$$

where t is the time in msec after the start of the discharge.

Once the loop voltage is known, the ohmic input power is given by $P_{oh} = I_p V_l$, and the electron conductivity temperature (in eV) is calculated using Spitzer resistivity and $Z_{eff} = 1$:

$$T_e = 376 \left(I_p / V_l a^2\right)^{2/3}. \qquad (3.5)$$

The average electron density can be measured with a Langmuir probe located between the upper outer ring and the wall, or by a 70 GHz interferometer. Since the interferometer system was not always functional the ion saturation current signal (J_{sat}) from the probe is numerically adjusted to match the interferometer given values:

$$\langle n_e \rangle = 0.05 J_{sat} / [T_e^{1/2} (1-\exp(-45/T_e))](10^{12}/\mathrm{cm}^3) \qquad (3.6)$$

where the $(1-\exp(-45/T_e))$ factor corrects for the probe bias voltage of only 45 volts.

After all these quantities are known it is possible to estimate the global energy confinement time given by:

$$\tau_E = 0.144 \langle n_e T_e \rangle / P_{oh} \qquad (3.7)$$

where $P_{oh} = I_p V_l$.

Many approximations are made in the derivation of all these quantities, so they give only a gross (but useful) representation of the plasma behavior.

A vertical array of 7 surface barrier detectors along the outside wall at one toroidal location monitor soft X-ray radiation with energies of 60 to 300 eV. Since the radiation is proportional to electron temperature, the detectors give a good indication of the central temperatures, as well as sawteeth related phenomena.

Impurities are detected with optical diagnostics consisting of four filtered photomultipliers which monitor lines of Carbon III and Oxygen III (from hydrocarbon impurities), Copper I (from interaction of the plasma with the rings) and Nitrogen III (from air leaks or boron nitride probe sheaths).

General diagnostics like plasma current, toroidal field, poloidal gap voltage etc., are digitized at 100 kHz using a DSP Technologies

TRAQ system model 4012 digitizer. Soft X-ray and impurity signals are digitized at 1 MHz using a DSP Technologies TRAQ system model 4012A and Le Croy model 8210 respectively. Equilibrium and fluctuating electrostatic signals with frequencies of up to 300 kHz are recorded at 1 MHz using two Le Croy model 8210 digitizers. For high frequency signals (in the MHz range) four DSP model 2001 digitizers are used at 10 MHz sampling rate. The CAMAC system is managed with the Model Data System (MDS) software, and data analysis is done with the Interactive Data Language (IDL) using a MicroVax II.

3.2 Spectral Analysis

3.2.1 Basic Concepts

Fluctuations in plasma parameters like density and potential are present in most experiments and are directly connected with particle and energy losses.[8] The basic concepts of digital linear spectral analysis techniques relevant to the analysis of fluctuation characteristics and fluctuation induced transport are summarized below.[9-11]

If $f_1(t)$ and $f_2(t)$ are two fluctuating signals (density and potential for example), then the cross-power spectrum $P_{12}(\omega)$ is defined as:

$$P_{12}(\omega) = F_1(\omega)\, F_2^*(\omega) \tag{3.8}$$

where $F(\omega)$ is the Fourier transform of $f(t)$, and the asterisk denotes a complex conjugate. The real and imaginary parts of $P_{12}(\omega)$ give the relative phase between the two signals:

$$\theta(\omega) = \tan^{-1} [\mathrm{Im}\,(P_{12}(\omega)) / \mathrm{Re}\,(P_{12}(\omega))] \qquad (3.9)$$

The auto-power spectrum of $f_1(t)$ is the square of the amplitude spectrum and is given by:

$$P_{11}(\omega) = F_1(\omega)\, F_1^*(\omega) = |F_1(\omega)|^2 \qquad (3.10)$$

The coherency spectrum is defined in terms of the auto and cross-power spectra:

$$\gamma_{12}(\omega) = \frac{|P_{12}(\omega)|}{[P_{11}(\omega)\, P_{22}(\omega)]^{1/2}} \qquad (3.11)$$

and measures the degree of similarity between the two signals as a function of frequency. Two perfectly coherent signals will have a coherency of one, while two completely unrelated signals will have zero coherency. If the two signals are spatially separated by a distance d, then assuming an exponential decay of the coherency we can define the coherency length as $L(\omega) = d / (-\ln\gamma)$. The coherency is a statistical quantity and an ensemble average over many terms is usually needed for a meaningful estimate. Note that the coherency between two signals calculated using one single realization is always one.

The cross-correlation is defined as:

$$R_{12}(\tau) = \frac{\left\langle \int_{-\infty}^{\infty} f_1(t)\, f_2(t+\tau)dt \right\rangle}{\left[\left\langle \int_{-\infty}^{\infty} f_1^2(t)dt \right\rangle \left\langle \int_{-\infty}^{\infty} f_2^2(t)dt \right\rangle \right]^{1/2}}$$

where

$$\int_{-\infty}^{\infty} f_1(t)\, f_2(t+\tau)dt = \int_{-\infty}^{\infty} F_1(\omega)F_2^*(\omega)\, e^{i\omega\tau}\, d\omega \tag{3.12}$$

The symbol < > denotes an ensemble average.

Like the coherency, the cross-correlation measures the similarity between the two signals (integrated in frequency), and we can similarly define the correlation length as $L = d\, /\, (-\ln R)$.

Error estimates of the statistical quantities defined above are complicated and the reader is referred to reference 12 for the derivations. For our purposes it is sufficient to know the expressions of the errors in the estimation of the coherency and the phase. For the coherence (γ^2) the random error is given by:

$$\varepsilon\left[\gamma_{12}^2\right] = \frac{\sqrt{2}\left(1 - \gamma_{12}^2\right)}{|\gamma_{12}|\sqrt{N}} \tag{3.13}$$

Note that the error in the coherence is smaller if the coherence itself is large, since it is easier to determine a causal relation for two signals that are very similar. The error is inversely proportional to the number of terms in the ensemble (N) as expected. The random error in the determination of the relative phase is similar to the coherence error:

$$\varepsilon[\theta_{12}] = \frac{\left(1 - \gamma_{12}^2\right)^{1/2}}{|\gamma_{12}|\sqrt{2N}} \qquad (3.14)$$

The two important applications of spectral analysis in this thesis are the calculation of wavenumber and wavenumber-frequency spectra, and the estimation of the fluctuation induced particle and energy fluxes.

3.2.2 The Wavenumber-Frequency Spectrum

If f(t) is a deterministic quantity, then a deterministic dispersion relation can be found relating wavenumber and frequency. If f(t) is turbulent, it may not have a deterministic dispersion relation: instead, the power at a given frequency band ω to $\omega+\Delta\omega$ may be distributed broadly in wavenumber space. In this case the best way to describe the dispersive properties of the medium is to define a statistical quantity $S(k,\omega)$ which represents the distribution of power as a function of frequency and one projection of the wavevector, in our case the poloidal wavenumber k_θ. Frequency spectra can easily be obtained from the signal of one probe, while wavenumber information would require simultaneous measurements of fluctuations in many points in space, which could be very expensive and disruptive to a plasma. Other methods make use of movable probes to change the spatial separation and use Fourier transforms to obtain the wavenumber spectrum , but sometimes it is not possible to cover a wide enough range of probe separation.

An alternative technique was developed[13] using a fixed probe pair to calculate a local wavenumber-frequency spectrum. In this technique, it is assumed that the fluctuations consist of a superposition of oscillations which are approximately sinusoidal in time and space, and with slowly varying amplitudes and wavenumbers. It is also assumed that the power in a single realization at a frequency ω is concentrated near a single wavenumber k, although statistically the averaged power could be distributed broadly in wavenumber space. Using two probes separated by a distance d, M records of length T and N digitized points are sampled. Care must be taken to prevent aliasing in frequency and space. From one of the two signals in one record, the auto power spectrum is calculated (to obtain information on frequency). Then the local wavenumber at a given frequency ω_l is calculated from the cross-power spectrum between the two signals:

$$k_l(\omega_l) = \theta(\omega_l)/d \qquad \text{where} \tag{3.15}$$

$$\theta(\omega_l) = \tan^{-1}[\,\mathrm{Im}P_{12}(\omega_l) / \mathrm{Re}P_{12}(\omega_l)\,]$$

At the coordinate point (k_l,ω_l) the power $P(\omega_l)$ is recorded. Since the turbulence is stochastic, examination of the next record will give a different value of power and wavenumber for this same frequency, so this new power value is entered at a different coordinate point. The process is repeated for all frequencies and data records, and the average power is calculated at each coordinate point (k,ω). This method is similar to the estimation of probability density functions by means of a histogram.

It is important to point out that this method of calculating S(k,ω) is only valid if the amplitudes and wavenumbers are slowly varying over a wavelength. This should be true for the lowest wavenumbers and frequencies which are dominant in Tokapole-II as is shown in chapter 4. If the turbulence is also uniform then our local estimation is a good measure of the general S(k,ω). In any event, caution must still be taken when interpreting the local S(k,ω), because the method will be incomplete if there are simultaneous counter propagating waves, which would be averaged out.

Once S(k,ω) is found, the statistical dispersion relation $\bar{k}(\omega)$ and its spectral width $\sigma_k(\omega)$ can be calculated as:

$$\bar{k}(w) = \sum_k k\, s(k \mid \omega) \tag{3.16}$$

where

$$s(k \mid \omega) = \frac{s(k,\omega)}{\sum_k s(k,\omega)} \quad , \quad s(k,\omega) = \frac{S(k,\omega)}{\sum_{k,\omega} S(k,\omega)}$$

and

$$\sigma_k(\omega) = \left\{ \sum_k \left[[k - \bar{k}(\omega)]^2\, s(k \mid \omega) \right] \right\}^{1/2} \tag{3.17}$$

Here $s(k \mid \omega)\Delta k$ is the fraction of power at a frequency ω with wavenumbers between k and k+Δk. The dispersion relation $\bar{k}(\omega)$ can also be calculated from the average phase between the two signals and their probe separation : $\bar{k}(\omega) = \bar{\theta}(\omega) / d$. The k-spectral width gives the spread in k of the turbulence, which can also be estimated from the coherency length $L(\omega)$ by: $\Delta k = \Delta m/r$ where m is the poloidal wavenumber and r is the radius of the flux surface (in cylindrical geometry), and $\Delta m = \pi r/L(\omega)$

3.2.3 Fluctuation Induced Transport

Fluctuation induced radial particle flux results when density and radial velocity fluctuations oscillate in a correlated way, that is $\Gamma = <\tilde{n}\tilde{v}>$. The radial velocity fluctuations are due to $\tilde{E} \times B_T$ drifts where $\tilde{E}$ is a poloidal electric field fluctuation caused by fluctuating plasma potentials. For electrostatic fluctuations and considering that potential fluctuations can be decomposed into sinusoidal Fourier components with wavenumber k, the electric field fluctuation can be written as $\tilde{E} = ik\tilde{\Phi}$. If the particle flux is decomposed into its frequency components, we may then write: [14]

$$\Gamma = \sum_f T(f)\, df$$

where $$T(f) = \frac{2}{B_T} \mathrm{Re}<N(f)E^*(f)> = \frac{2}{B_T} \mathrm{Im}<k(f)N(f)\Phi^*(f)> \qquad (3.18)$$

Here k(f) is the wavenumber calculated as in eq. (3.15) , N(f) and Φ(f) are the Fourier transforms of n(t) and Φ(t) respectively. Since k(f) is not deterministic it has to remain inside the ensemble averaging operator <>. However, for purposes of interpretation let us write:[11]

$$T(f) = (2/BT)\, k(f)\, \mathrm{Im}\langle N(f)\Phi^*(f)\rangle$$

which can be rewritten as:

$$T(f) = (2/BT)\, k(f)\, A_n(f)A_\Phi(f)\, \sin[\alpha_{n\Phi}(f)]\gamma_{n\Phi}(f) \tag{3.19}$$

where $A_n(f)$ and $A_\Phi(f)$ are the amplitude spectra of $n(t)$ and $\Phi(t)$, and $\alpha_{n\Phi}(f)$ and $\gamma_{n\Phi}(f)$ are the angle and the coherency between them. We can see now, that the transport depends not only on the strength of the electric field and density fluctuations (from the $k(f)$, $A_n(f)$ and $A_\Phi(f)$ terms), but also on the way they are correlated: the degree of coherency and the angle between them indicates how much they are correlated. The direction of the flux (radially inward or outward) is determined from the sign of the wavenumber k and the angle $\alpha_{n\Phi}(f)$. Note that for maximum transport density and electric field (and thus velocity) fluctuations should be in phase or, conversely $\alpha_{n\Phi}(f)$ should be 90 degrees. For a sinusoidal oscillation the degree of coherency is always one, but for turbulent fluctuations, it is between zero and one, so the transport is reduced.

Error estimates of the particle flux spectrum were made using equation 3.19 and the error expressions of the coherence and phase. Large relative uncertainties occur if the average angles $\alpha_{n\Phi}(f)$ are very small.

The energy transport induced by electrostatic fluctuations is given by:

$$Q_E = 3/2 <\tilde{p}\tilde{v}> = 3/2B_T <\tilde{p}\tilde{E}> \quad \text{so}$$

$$Q_E = 3/2B_T [\, k_B T_e <\tilde{n}\tilde{E}> + k_B n <\tilde{T}_e \tilde{E}>]. \qquad (3.20)$$

The first term is the convected energy flux (directly associated with the particle flux), and the second term is the conducted energy flux. In Tokapole-II the electron temperature fluctuations were measured to be small, so the energy flux is due to convection only.

For the fluctuation analysis described above, the data records were chosen to have 128 points, with about 200 terms for each ensemble average. The mean value was subtracted from the fluctuations to ensure no dc components, and a Hanning window[9] was applied to prevent leakage. Programs were made using the Interactive Data Language (IDL) and its Fast Fourier Transform routine, and also using parts of the Integrated Signal Analysis, a plasma fluctuation diagnostic software system by Integral Signal Processing, Inc. Except for the calculations of $S(k,\omega)$ and $\sigma_k(\omega)$, which were done using the ISA package only, all other spectral properties were calculated using the package and programs written in IDL, with similar results.

3.3 Langmuir Probes

3.3.1 Relevant Probe Theory

Electrostatic probes (Langmuir probes) are one of the most widely used plasma diagnostics, due to their apparent simplicity. In its simplest form it is essentially a conductor immersed in a plasma. Its nonlinear behavior makes an exact theory extremely difficult, but reasonable approximations make simple interpretations possible and plasma parameters can then be obtained very easily.

When an electrically isolated conductor is in contact with a plasma, the conductor "floats" to a potential that is negative with respect to the plasma, because electrons being more mobile will flow to the conductor more quickly than the ions. The excess negative charge near the probe surface will build up electric fields to repel electrons, and quasineutrality is no longer valid in a layer around the probe (with a thickness of about a Debye length), called the sheath. In order to keep a charge distribution that will permit this potential drop, the velocity with which the ions enter the sheath must satisfy what is called the sheath (or Bohm) criterion. If (for simplicity) species 1 is cold, i.e., has $T_1 = 0$, then they must enter the sheath with a minimum velocity which is determined by the other species temperature: $v_1 = (k_B T_2/m_1)^{1/2}$. For ions (usually the colder species in a ohmic plasma) this velocity is the ion acoustic velocity:[15]

$$v_s = (k_B T_e/M_i)^{1/2} \qquad (3.21)$$

Since the ions are usually colder than electrons (the approximation $T_i=0$ will be used) there must be a region outside the sheath where quasineutrality holds but a weak electric field exists to accelerate the ions; this region is called the pre-sheath.

If a voltage is applied to this conductor, a current is collected as shown in figure 3.5. At large negative or positive voltages, only one species is collected while the majority of the other species is repelled, and saturation is achieved because of shielding. The saturation currents are given in terms of the velocity of the particles at the sheath edge. For electron saturation this velocity is given by the average electron velocity at the sheath edge which for a Maxwellian distribution will give:

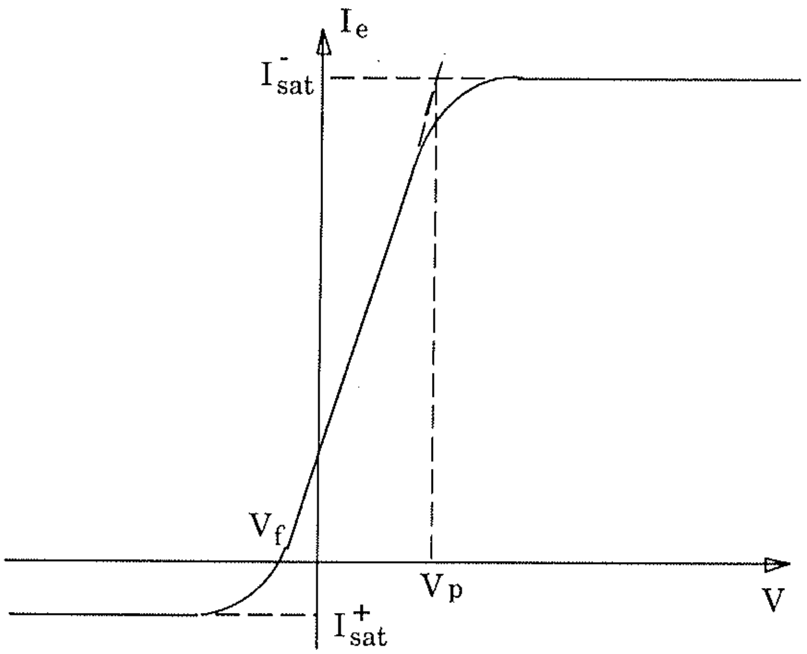

Fig. 3.5 Characteristic curve of a Langmuir probe: electron current collected versus voltage applied.

$$I^{-}_{sat} = (1/4)neA(8k_BT_e/\pi m_e)^{1/2} \quad \text{(in cgs-esu units)} \qquad (3.22)$$

where n is the plasma density and A is the sheath area. Since electrons are hotter than ions the sheath criterion is easily met by the electron average velocity. For ion saturation however, the sheath criterion requires that the minimum velocity be the sound velocity which is larger than the ion average velocity, so in this case the saturation current is given with a good approximation by:[16]

$$I^{+}_{sat} = (1/4)neA(8k_BT_e/\pi M_i)^{1/2} \qquad (3.23)$$

The region between the ion and the electron saturation, is called the transition region, where both ion and electron currents are drawn. As the applied voltage becomes more positive more electrons and less ions are collected. The net electron current drawn can be expressed as:

$$I = -I^{+}_{sat} + I^{-}_{sat} \exp\,[e(V - V_p)/k_BT_e] \qquad (3.24)$$

where Vp is the plasma potential. When V (the bias voltage) is equal to the floating potential V_f, no net current is drawn, i.e, the ion current I^{+}_{sat} equals the electron current $I^{-}_{sat} \exp\,[e(V_f - V_p)/K_BT_e]$. This will give the very useful relation:

$$V_p = V_f + (k_BT_e/2e)\ln(M_i/m_e)^{1/2} \sim V_f + 3.7(k_BT_e/e) \qquad (3.25)$$

i.e., the plasma potential can be obtained from the floating potential measured once the electron temperature is known.

The current collected shown in figure 3.5 is for a single conductor, (single probe) with voltages applied with respect to a reference point (for example the vessel wall). Another arrangement is often used, in which two conductors are biased with respect to one another, but are insulated from ground, keeping the system floating with the plasma: the negative current collected by one probe is compensated by a positive current collected by the other so the system follows the changes in plasma potential. This arrangement is called a double probe. If both probes are unbiased then no current is drawn. If probe 1 is biased negatively with respect to probe 2, a net positive current will flow from 1 to 2. It is easily shown that this current is given by:[15]

$$I = I^{+}_{sat} \tanh(eV/2k_BT_e) \tag{3.26}$$

where V is the applied voltage between the two probes. Ion saturation is reached for sufficiently high voltages. One of the advantages of the double probe is that the net current drawn is limited by the ion saturation current, unlike the single probe which can collect much larger and more perturbative electron currents.

In another arrangement called the triple probe[17-18] (used in this thesis), a third conductor is added and is kept floating with respect to the plasma. If the double probe is biased to saturation with tip 1 negative with respect to tip 2 and tip 3 is kept floating, the currents collected by each tip are given by:

$$I_1 = -I^+{sat}$$
$$I_2 = -I^+{sat} + I^-{sat} \exp [e(V_2 - V_p)/k_BT_e]$$
$$I_3 = -I^+{sat} + I^-{sat} \exp[e(Vf - Vp)/k_BT_e] = 0 \qquad (3.27)$$

Since $I_1 = -I_2$ (no net current flows from the plasma to the double probe and assuming that all probes have the same area) we have:

$$2I^+{sat} = I^-{sat} \exp [e(V_2 - V_p)/k_BT_e]$$
$$I^+{sat} = I^-{sat} \exp[e(Vf - Vp)/k_BT_e] \qquad (3.28)$$

These equations will then give:

$$(k_BT_e) / e = (V_2 - V_f) / \ln 2 \qquad (3.29)$$

This is the triple probe method of measuring the electron temperature, from the voltages measured at the positively biased tip of the double probe (V_2) and the floating potential. Once the temperature is known the plasma density is obtained from the ion saturation current that flows in the double probe given by eq. (3.23).

The simple theory presented above enabled us to measure electron temperature, density and plasma potential in a relatively easy way. Several assumptions had to be made which may not always be met by the experimental conditions. First, the expressions for the acoustic and average speeds assume a Maxwellian distribution,[19] and in ion saturation measurements only those few electrons in the tail that are energetic enough to overcome the sheath potential are collected. So ion saturation currents can be affected if there is a significant amount of fast electrons for example. Second, it is assumed that the ions are cold, which is not true experimentally and it would have to be taken into account in the calculation of the ion sound speed (the accelerating force is the plasma pressure which would have a contribution from finite ion temperature). Third, magnetic fields were neglected in this theory. In the presence of a magnetic field the cross-field flow to the probes is reduced while parallel flow is unaffected. If the gyroradius is much larger than the dimensions of the probe like it usually is for ions, then this effect is not seen, but for electrons, there is almost no cross-field flow, so the collection area is reduced, affecting the sheath potential drop, and consequently the interpretation of the floating potential signal.[20] All of these factors could contribute with a factor of two or so in the interpretation of the data, but for simplicity the ideal simple probe theory presented will be used. It should not affect significantly the conclusions on fluctuation measurements which are the objective of this thesis.

Other factors also need to be considered when using electrostatic probes. The theory presented is valid for a planar probe and it should be a good approximation for cylindrical and spherical probes if the probes' dimensions are large compared with the sheath's thickness (thin sheath approximation). Sheath expansion occurs when the probe is biased:[20] the sheath dimensions expand about one Debye length per k_BT_e/e volts applied. Since the voltages applied for saturation are about 3 to 4 times k_BT_e/e and Debye lengths are much smaller (around $2\text{x}10^{-2}$ mm) than the probe dimensions (several mm) the sheath area is approximately the probe area itself.

Another effect that must be considered in multiple array probes is shadowing.[21] If two probes are aligned on the same field line, density is depleted for the probe situated in the downflow side of the collected particle. For ion flow, the gyroradius is often larger than the probe dimension so this effect is not so important but for electrons it is. Care must be taken to align the probes so that no shadowing occurs.

Secondary electron emission can be present if the conductor is overheated, and that would increase the positive current collected thus affecting the ion saturation and floating potential measurements.

Arcing is often observed in electrostatic probes. Usually current carriers are provided by impurities in the insulating surface when the voltage applied is very large. Careful cleaning during construction and conditioning with plasma discharges is usually sufficient to prevent arcing. Secondary electron emission also can provide current carriers. In Tokapole-II electrostatic probes could be inserted up to 8 cm (probably ~ 1 cm past the separatrix) before arcing occurred.

3.3.2 Probe Construction for Correlation and Transport Studies

The electrostatic probes used for correlation and transport studies (chapters 4,5 and 6) consisted of an array of four probes inserted at the outside midplane of the machine, in a toroidal location that would place them in the shadow of the removable outer limiter (approximately 10 cm away from it toroidally). They are arranged in a rectangular array so that two tips separated poloidally by 3 mm are used as a double probe (biased to collect ion saturation current) and the other two (also separated by 3 mm poloidally and 5 mm away in the toroidal direction from the first two) are left floating with the plasma to measure poloidal electric field fluctuations (through differences in plasma potential fluctuations). Details of this arrangement are shown in figure 3.6.

Each probe consists of a cylindrical platinum wire (platinum was chosen due to its lower secondary electron emission properties),[22] 3 mm in length and 0.4 mm in diameter. These dimensions meet the condition $\lambda_D << r_p$ for a thin sheath approximation (r_p is the probe dimension) but $r_p \lesssim r_i$ (where $r_i \sim 2$ mm is the ion gyroradius) so magnetic field effects should occur. The probes separation (3 mm) is small enough to avoid space aliasing since dominant wavenumbers are small in Tokapole-II (see results chapter 4 and 5). Boron nitride particle shields keep the tips about 1.3 cm away from the main stainless steel body, to ensure that the probes' sheath and pre-sheath regions do not contact the grounded body. Since boron nitride does not electrically shield the conductors from the plasma, the noise contribution from the unshielded part of the probes was measured experimentally (by plugging a dummy probe) and added to the background noise in the data

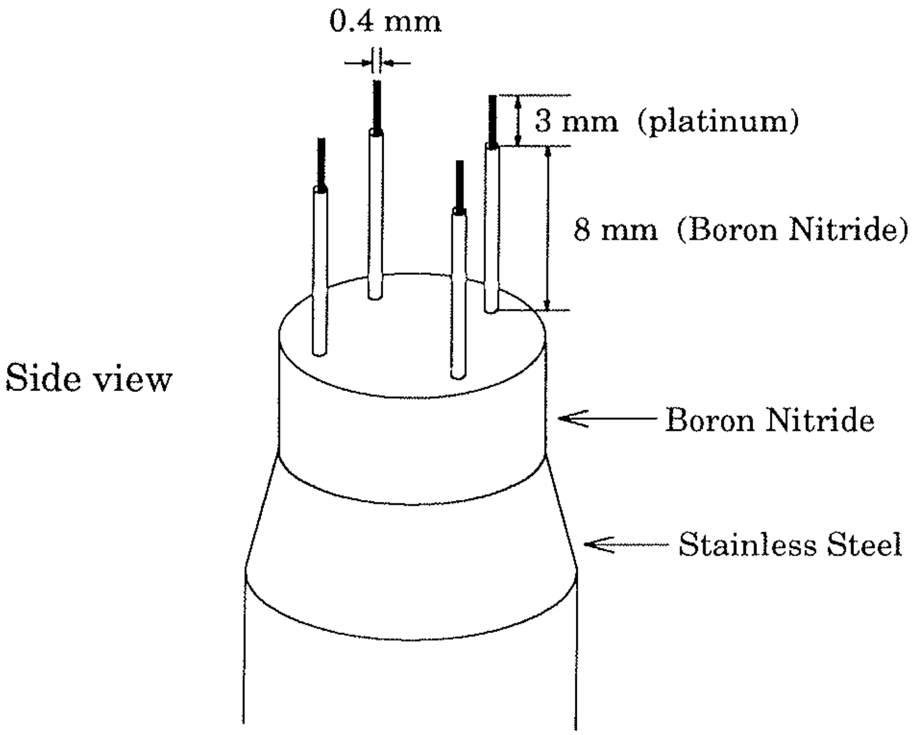

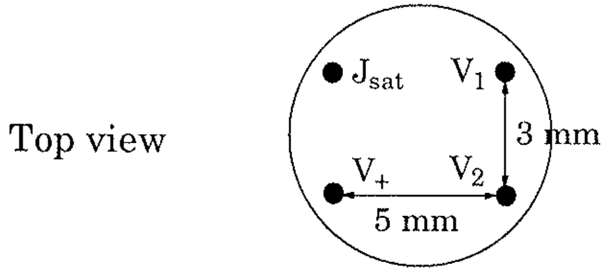

Fig. 3.6 Side and top views of Langmuir probes array. Two probes were used as a double probe and the other two measured floating potential signals.

analysis. This extra noise is very small compared with the signals of interest.

In inserting the probe, care was taken to align it properly. To avoid shadowing effects, two probes cannot be placed in the same field line, but on the other hand, temperature measurements require V_2 (floating potential at tip 2) and V_+ (positive tip of double probe) to be placed as close as possible, and for transport measurements J^+_{sat} and V_1 should ideally be measured in the same position or in the same field line. Since the magnetic field line makes an angle of about 5 to 8 degrees with the horizontal direction, aligning the pairs (V_2,V_+) and (J^+_{sat},V_1) horizontally was good enough to meet these two conditions.

The double probe is biased to 200 volts through a 1,000 μF capacitor and the ion saturation current is measured through a 10 Ω resistor. The voltage across the resistor is divided and fed into two differential amplifiers (Tektronics AM502), to separate equilibrium values from the fluctuating part. The two floating potential signals and the potential of the positively biased tip are first attenuated with a 1/11 voltage divider, and each signal (read from a 10 kΩ resistor) is divided and fed into two amplifiers to separate equilibrium from fluctuating parts. The four fluctuating signals are RC high-pass filtered at 10 kHz (in the amplifier) and low-pass filtered (using an n=5 Cauer-Elliptic filter) at 300 kHz to prevent aliasing. The eight signals (4 fluctuating and four equilibrium signals) are then digitized at 1 MHz and stored. Figure 3.7 shows a schematic diagram of the circuits.

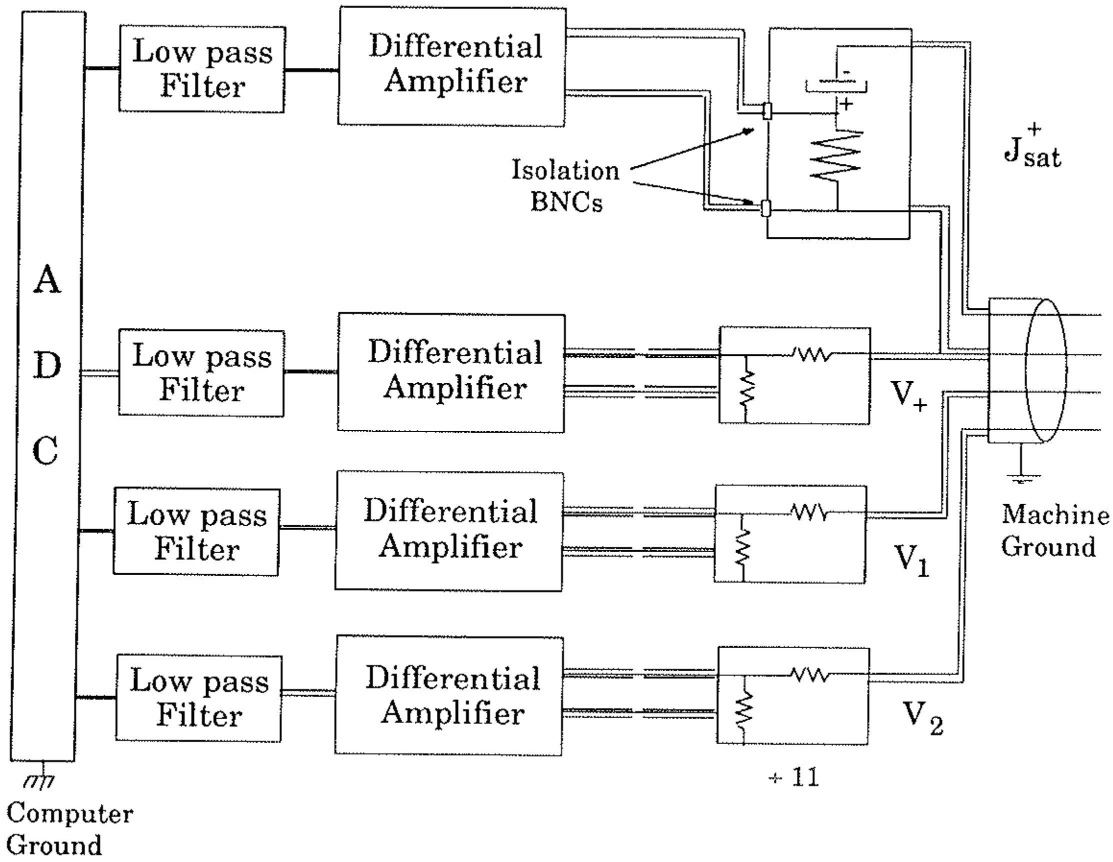

Fig. 3.7 Schematic diagram of Langmuir probes system. Only fluctuation signals hardware are shown. Each signal is also fed to amplifiers without filters for equilibrium measurements.

The system was calibrated to obtain a gain x frequency curve which account for losses in filters etc.. A phase calibration was also made as a function of frequency to account for the different hardware used in J^+_{sat} and floating potential measurements and possible differences in the filters response times.

For correlation and transport studies the equilibrium electron density and temperature measured by the triple probe agreed with simultaneous measurements made with an admittance probe in initial tests.[23] During the data taking run however, the admittance probe electronic circuits were not functional, so they are not reported for this case.

3.3.3 Fluctuation Measurements

The fluctuation quantities of interest in this experiment are the density, plasma potential, and electron temperature fluctuations. Both the ion saturation current and the floating potential signals measured are a mixture of the desired quantities (density and plasma potential respectively) with the electron temperature. In the triple probe method, it is assumed that the three quantities of interest are uniform in the volume enclosing the three tips. For fluctuation measurements this requirement means that the probes have to be in the same correlation volume, i.e., the correlation length of the desired quantities has to be greater than the probes separation and coherencies have to be high in the frequencies of interest.

Consider the ion saturation current density and the plasma potential fluctuations:

$$\tilde{J}^{+}_{sat} \alpha\, \tilde{n} \sqrt{T_e} + n\sqrt{\tilde{T}_e} \quad \text{so} \quad \frac{\tilde{n}}{n} \cong \frac{\tilde{J}^{+}_{sat}}{J^{+}_{sat}} - \frac{\tilde{T}_e}{2T_e}$$

$$\frac{\tilde{V}_p}{T_e} \alpha \frac{\tilde{V}_f}{T_e} + \frac{\tilde{T}_e}{T_e} \tag{3.30}$$

Squaring and ensemble averaging we have:

$$\frac{\tilde{n}}{n} = \left[\left\langle \left(\frac{\tilde{J}^+_{sat}}{J^+_{sat}} \right)^2 \right\rangle + \frac{1}{4} \left\langle \left(\frac{\tilde{T}_e}{T_e} \right)^2 \right\rangle + \left\langle \frac{\tilde{n}\tilde{T}_e}{nT_e} \right\rangle \right]^{1/2}$$

$$\tilde{V}_p = \left[\langle \tilde{V}_f^2 \rangle + 2.8 \langle \tilde{T}_e^2 \rangle + 5.6 \langle \tilde{V}_f \tilde{T}_e \rangle \right]^{1/2} \tag{3.31}$$

So depending on the $\tilde{T}_e$ and its correlation with $\tilde{n}$ and $\tilde{V}_f$, J^+_{sat} and $\tilde{V}_f$ can be a good or bad estimate of $\tilde{n}$ and $\tilde{V}_p$. For Tokapole-II $\tilde{T}_e$ was measured to be small and upper estimates (based on statistical uncertainties and assuming perfect correlation with density and floating potential fluctuations) give $\tilde{T}_e/T_e \sim 0.4\tilde{n}/n \sim 0.2\, \tilde{V}_p/T_e$.

Floating potential fluctuations could affect J^+_{sat} measurements if single probes are used, in which case, if $\tilde{V}_f$ were very large it could bring the probe out of saturation. Fortunately, this does not happen in double probes since it floats with the plasma accompanying its fluctuations.

3.3.4 Probe Construction for Small Spatial Scale Studies

For the small spatial scale studies presented in Chapter 7, two sets of probes were built (figures 3.8 and 3.9). In one set (probe set # 1), the spherical platinum tip was placed near two "large" cylindrical tips

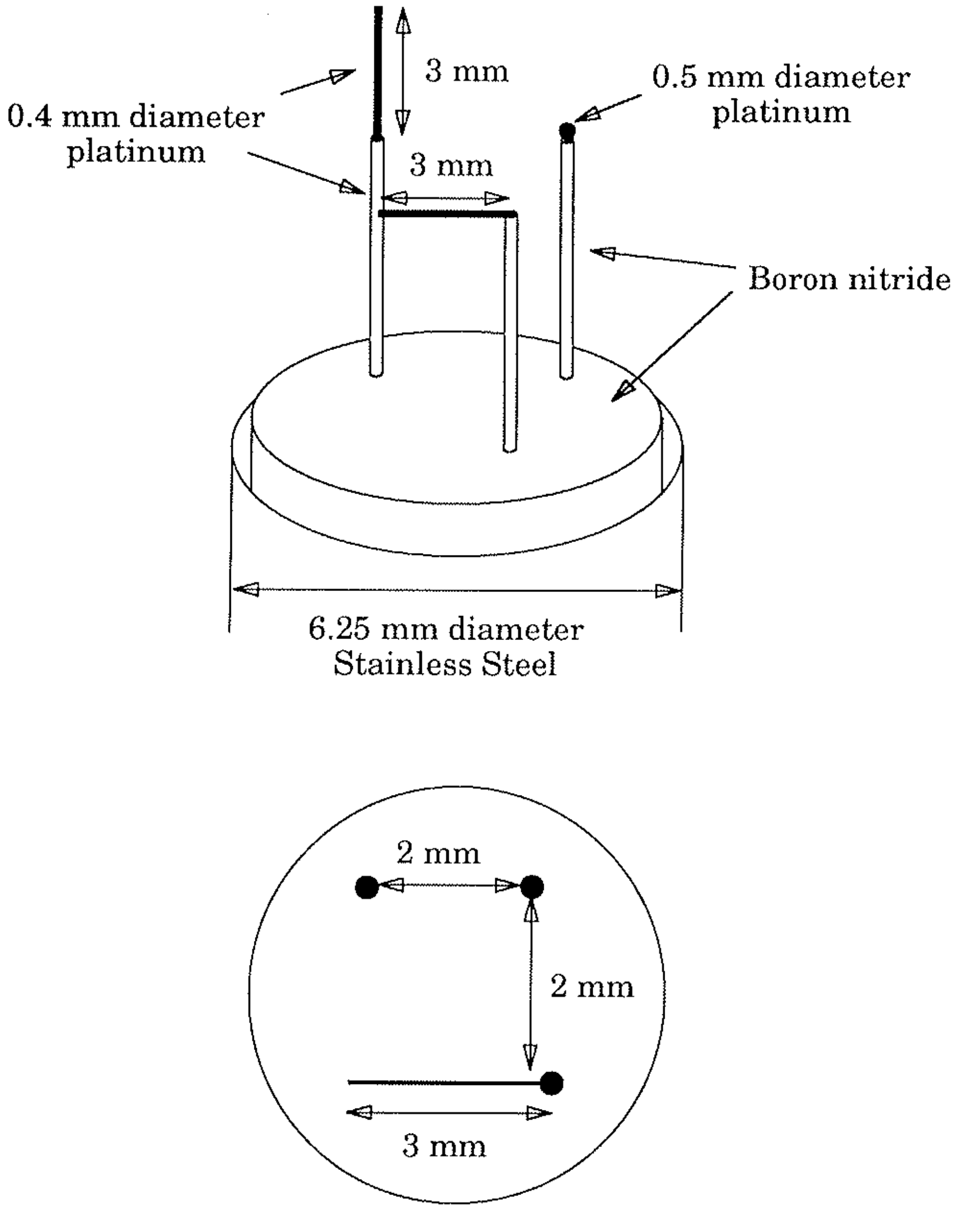

Fig. 3.8 Probe set # 1: Two 3 mm cylindrical tips (one oriented radially, one poloidally), and a 0.5 mm diameter spherical tip

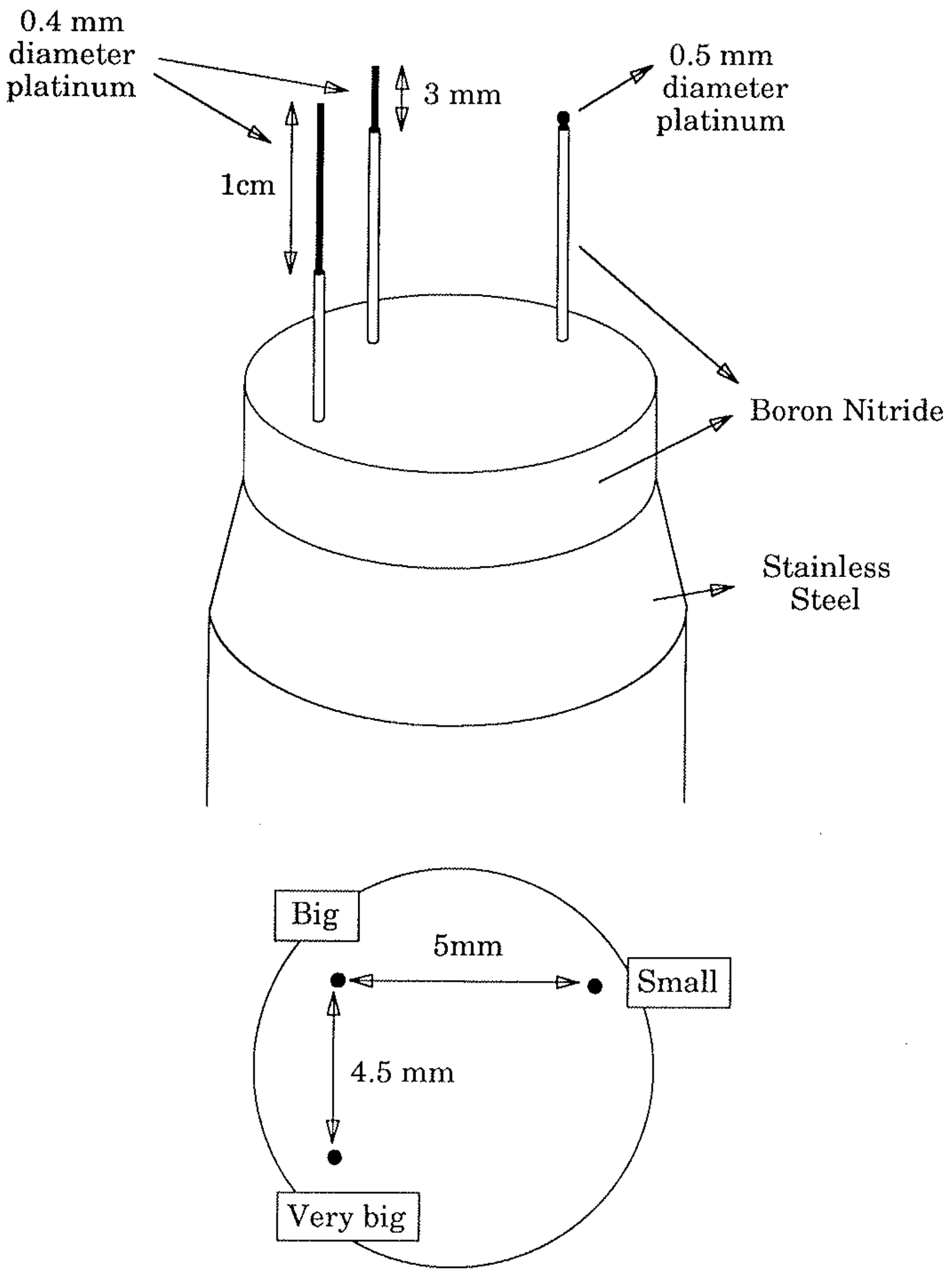

Fig. 3.9 Probe set # 2: Two cylindrical radial tips with lengths: 1cm and 3 mm, and a spherical 0.5 mm diameter tip.

3 mm in length and 0.4 mm in diameter oriented so that one tip has its length in the radial direction and the other in the poloidal direction.

The second set (probe set # 2) has the "small" spherical tip near a "large" cylindrical tip and an even larger cylindrical tip (1 cm in length, 0.4 mm in diameter) both oriented in the radial direction. All probes are biased to 200 V as single probes in ion saturation.

Figure 3.10 shows a diagram of the circuitry used. The output signal of the probes are divided and fed into 3 separate circuits: a high frequency amplifier and filter system (developed by D. Kortbawi and T. Lovell)[24] is used to measure fluctuations from 500 kHz to 1.5 MHz (which we will call "high" frequency), another amplifier and filter system (Tektronix AM502 which has passive RC high and low-pass filters) measures frequencies from 10 kHz to 500 kHz ("low" frequency), and a third amplifier (another AM502 used without filters) measures the equilibrium part of the ion saturation. Equilibrium and low frequency signals are recorded at 1 MHz using LeCroy model 8210 digitizers and high frequency signals are digitized at 10 MHz using DSP 2001 digitizers.

The band-pass filters used in the high frequency system can be exchanged, and a second set of filters from 300 kHz to 1.5 MHz was used with probe set # 2 (the filter modules used were n = 3 Cauer-Elliptic band-pass filters). The reason for changing the filter system was the fact that the low frequency circuit caused aliasing problems in the power spectra because the only low-pass filter available at the time was a

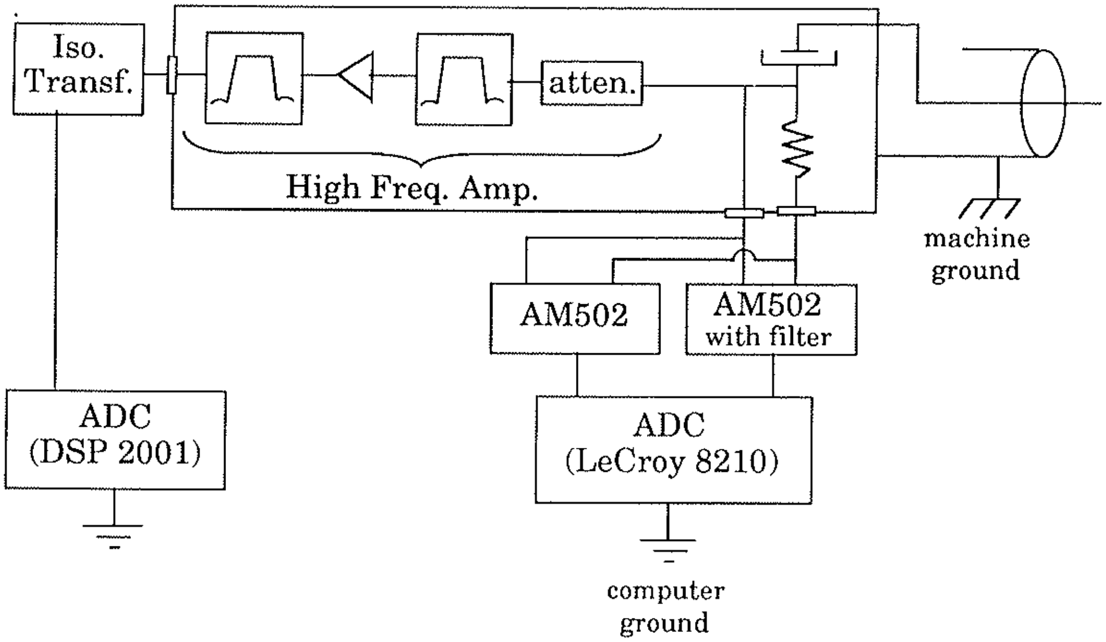

Fig. 3.10 Schematic diagram of Jsat probe setup for high and low frequencies.

1 MHz (3 dB point) RC filter in the Tektronix AM502 amplifier and the Nyquist frequency was 500 kHz. The low frequency data is therefore reliable only at the lowest frequencies (see section 7.3). The original band-pass filter at the high frequency amplifier system had a high frequency 3 dB point at 5 MHz. It had to be replaced due to the extreme sensitivity of the high frequency amplifiers to higher frequency noise from the machine's instrumentation (particularly the microwave interferometer system) in the single probe configuration which used the machine's walls for electric ground. The noise detected by the high frequency hardware was also enhanced when the low frequency circuit

was connected, so high and low frequency data had to be taken separately.

Data analysis consisted in the calculation and comparison of the amplitude spectra measured by the different probes. The IDL's Fast Fourier Transform routine was used for this calculation. For low frequency fluctuations time records of 256 points were chosen and for high frequencies 512 or 256 points per record were used. The mean value (DC component) is removed and a Hanning window is applied to prevent leakage. For high frequencies, the band-pass filter (with a high frequency corner of 1.5 MHz) ensured no aliasing problems (Nyquist frequency was at 5 MHz), but for low frequencies, a low-pass filter was not available at the time so some aliasing is expected.

3.3.5 The Admittance Probe

The electron temperature and density profiles were measured with a nearby admittance probe (30 degrees away in the toroidal direction). The admittance probe method consists in measuring the admittance across the sheath which is given by:[23]

$$\left.\frac{dI}{dV}\right|_{V_f} = - \frac{I^+_{sat}}{kT_e} = Y \qquad (3.32)$$

The electron temperature and density can therefore be determined by measuring the admittance Y (which has the dimensions of inverse resistance) of a floating probe and the ion saturation current measured by a nearby probe. The sheath admittance is determined by measuring the output of a capacitance bridge (which ensures that the probe is at floating potential) which is balanced in the absence of the plasma.

Figure 3.11 shows the schematic diagram of the admittance probe system hardware. A 2 MHz sinusoidal signal is fed into the capacitance bridge and a circuit that generates two sinusoidal signals (with the same frequency as the input signal) in quadrature with each other (sine and cosine). These reference signals are then fed into a phase and amplitude detector, which also receives the output signal of the bridge. What this detector does, is basically as follows: the input signal (the output of the bridge in the presence of plasma) is assumed to have the form $V(t) = A(t) \sin(\omega_0 t + \Phi(t))$, where A(t) is the amplitude modulation, ω_0 is the carrier oscillation frequency (2 MHz), and $\Phi(t)$ is a phase modulation. This input signal is then multiplied by one reference signal in the form $[1+ \sin(\omega_0 t)]$ and by the other reference signal in the form $[1 + \cos(\omega_0 t)]$. These two products can then be squared, added, and square root taken to yield the amplitude A(t), and the arc tangent of the ratio will give the phase $\Phi(t)$. When the system is calibrated, a known resistance and capacitance is connected to the probe, and the amplitude and phase are calculated by the detector, so that alterations to A(t) and $\Phi(t)$ due to attenuations, gains and delays caused by the hardware can be

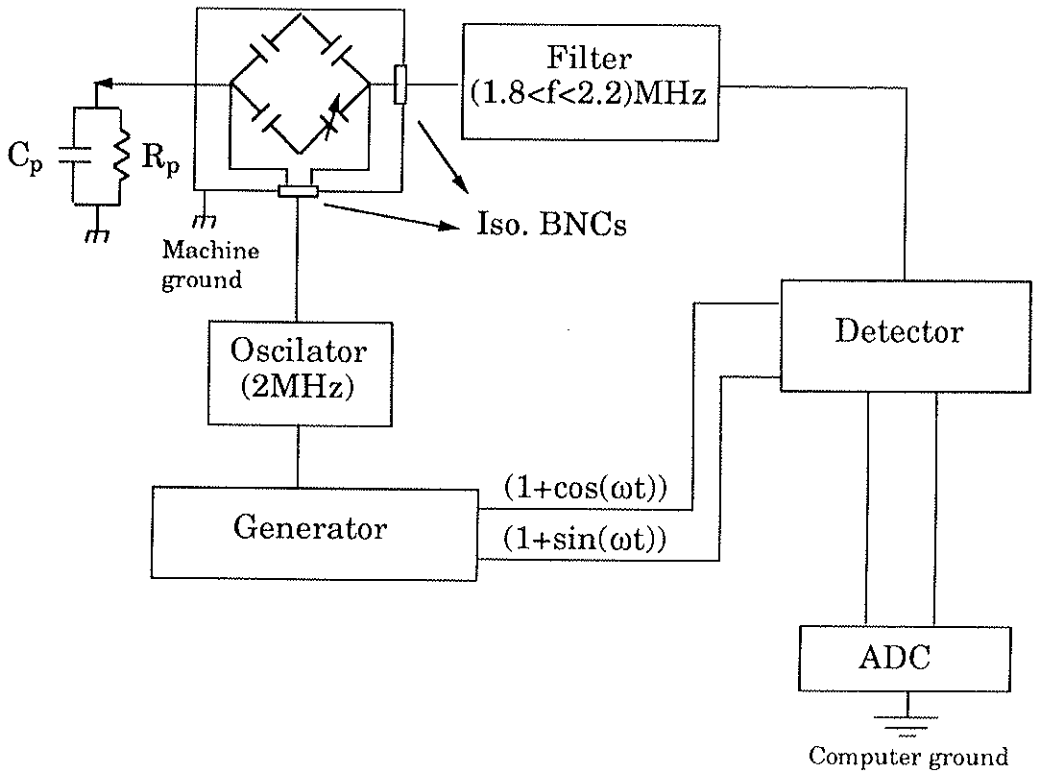

Fig. 3.11 Schematic diagram of admittance probe electronic circuits.

properly added or subtracted. In the presence of plasma, the sheath impedance Z_p is given by:

$$Z_p = \frac{K}{4}\left[\left(\frac{1}{V_d} - 1\right)\Big/\left(1 + \frac{K}{Z_d}\right) - 1\right] \qquad (3.33)$$

where $K = -i/(\omega_0 C_B)$, C_B is the bridge's capacitance, Z_D is the detector impedance and $V_D = A(t)\cos(\Phi(t)) + iA(t)\,\mathrm{sine}\,(\Phi(t))$. Usually the sheath impedance is mostly resistive, so $1/\mathrm{Re}(Z_p)$ will give the admittance value.

The admittance probe system consisted of two cylindrical platinum tips 3 mm in length and 0.4 mm in diameter, separated by

3 mm from each other. One of them is kept floating and connected to the bridge, and the other is biased into ion saturation (at - 200V).

The generator of signals in quadrature and the phase and amplitude detector system are parts of the electronics system built by David Kortbawi for the study of Alfven Wave heating in Tokapole.[24]

References

1. Biddle, A. P., Dexter, R. N., Groebner, R. J., Holly, D. J., Lipschultz, B., Phillips, M. W., Prager, S. C., Sprott, J. C., Nucl. Fusion **9** (1979), 1509.

2. Sprott, J. C., Lovell, T. W., University of Wisconsin-Madison Plasma Studies PLP 744 (1978).

3. Sprott, J. C., University of Wisconsin-Madison Plasma Studies PLP 889 (1983).

4. Sprott, J. C., University of Wisconsin-Madison Plasma Studies PLP 777 (1979).

5. Groebner, R. J., Ph.D. thesis University of Wisconsin-Madison (1979).

6. Moyer, R. A., Ph.D. thesis University of Wisconsin-Madison (1988).

7. Sprott, J. C., University of Wisconsin-Madison Plasma Studies PLP 962 (1985).

8. Ritz, Ch. P., Powers, E. J., Rhodes, T.L., Bengston, R. D., Gentle, K.W., Lin, H., Phillips, P.E., Wootton, A. J., Brower, D.L., Luhmann Jr., N. C., Peebles, W. A., Schock, P. M., Hickok, R. L., Rev. Sci. Instrum **59** (1988), 1739.

9. Smith, D. E., Powers, E. J., Caldwell, G. S., IEEE Transactions of Plasma Science Vol. PS-2, 261 (1974).

10. Brigham, E. O., "The Fast Fourier Transform", Prentice-Hall,

Englewood Cliffs, N.J., (1974).

11. Integrated Signal Analysis, Reference Guide, Integrated Signal Processing, Inc. (1989).

12. Bendat, J. S., Piersol, A. G., "Random Data Analysis and Measurement Procedures", 2nd Edition, Wiley-Interscience, John Wiley and Sons, New York, (1986).

13. Beall, J. M., Kim, Y. C., Powers, E. J., J. Appl. Physics **53** (1982), 3933.

14. Powers, E. J., Nucl. Fusion **14** (1974), 749.

15. Chen, F. F., "Plasma Diagnostic Techniques", chapter 4, edited by R. H. Huddlestone and S. Leonard, Academic Press, New York, 1965.

16. Sprott, J. C., University of Wisconsin-Madison Plasma Studies PLP 88 (1966).

17. Chen, S. L., Sekiguchi, T., Jou. Appl. Physics **36** (1965), 2363.

18. Sprott, J. C., University of Wisconsin-Madison Plasma Studies PLP 109 (1967).

19. Stangeby, P. C., Phys. Fluids **27** (1984), 682.

20. Rempel, T. D., University of Wisconsin-Madison Plasma Studies PLP 1083 (1991).

21. Vu, H. X., Gould, R. W., Phys. Fluids **B** (1989), 68.

22. Rempel, T. D., private communication.

23. Sprott, J. C., Rev. Sci. Instrum. **39** (1968), 1569.

24. Kortbawi, D., Ph. D. thesis, University of Wisconsin-Madison (1988)

CHAPTER 4

$<q_a>$ Scaling of Electrostatic Fluctuations in Tokapole-II

This chapter describes the experimental results obtained when $<q_a>$ was varied from 1 to 4 in the magnetic limiter configuration. Within this range of $<q_a>$, the energy confinement times varied by almost an order of magnitude from about 50 μsec to 350 μsec. Despite these large variations in global parameters, the electrostatic turbulence properties and their contribution to transport remained roughly unchanged. The contribution of electrostatic turbulence to transport is very small, being at least two orders of magnitude below the estimated total energy flux. When a material limiter is inserted (as described in Chapter 5) an enhancement of the turbulence is seen at high $<q_a>$ but it is attributed to a local density gradient increase rather than an effect of the magnetic configuration, which is not affected by the limiter. Therefore, although a complete $<q_a>$ scan was not performed with the limiter inserted, we believe that the independence of the turbulence on $<q_a>$ is valid for that case as well. The global equilibrium characteristics of the discharges are briefly presented first, followed by the fluctuation and transport properties of the four $<q_a>$ cases studied, which are described in detail.

4.1 Equilibrium Characteristics

The magnetic limiter configuration in Tokapole-II permits operation in a wide range of edge safety factor values. Detailed description of the discharge characteristics at the various $<q_a>$ values was described in previous works.[1] Only a summarized description will be given here, together with the radial profiles of the relevant quantities like electron temperature, density, pressure and plasma potential.

A typical "high $<q_a>$" ($<q_a> > 2$) discharge in Tokapole-II is shown in figure 4.1. Like most tokamaks with similar size and ohmic power, these discharges have loop voltages on the order of a few volts, plasma currents around ten kA, and energy confinement times about hundreds of microseconds. The soft X-ray signals show sawtooth activity in the center after the initial heating phase (after the peak of the SXR). For these discharges, it was possible to insert Langmuir probes up to $r = 8$ cm which was the position of the probe for the floating potential and ion saturation current signals shown. The toroidal field for this $<q_a> = 3$ discharge was 5.0 kG.

Figure 4.2 shows a typical "Low $<q_a>$" discharge ($<q_a> < 2$). By increasing the ohmic power and lowering the toroidal field, higher values of loop voltage and plasma current are obtained, compared to high $<q_a>$ discharges. Energy confinement times are estimated to be about tens of microseconds. Soft X-ray signals from the midplane of the machine do not always show significant sawtooth activity in the center of these discharges . Floating potential and ion saturation current

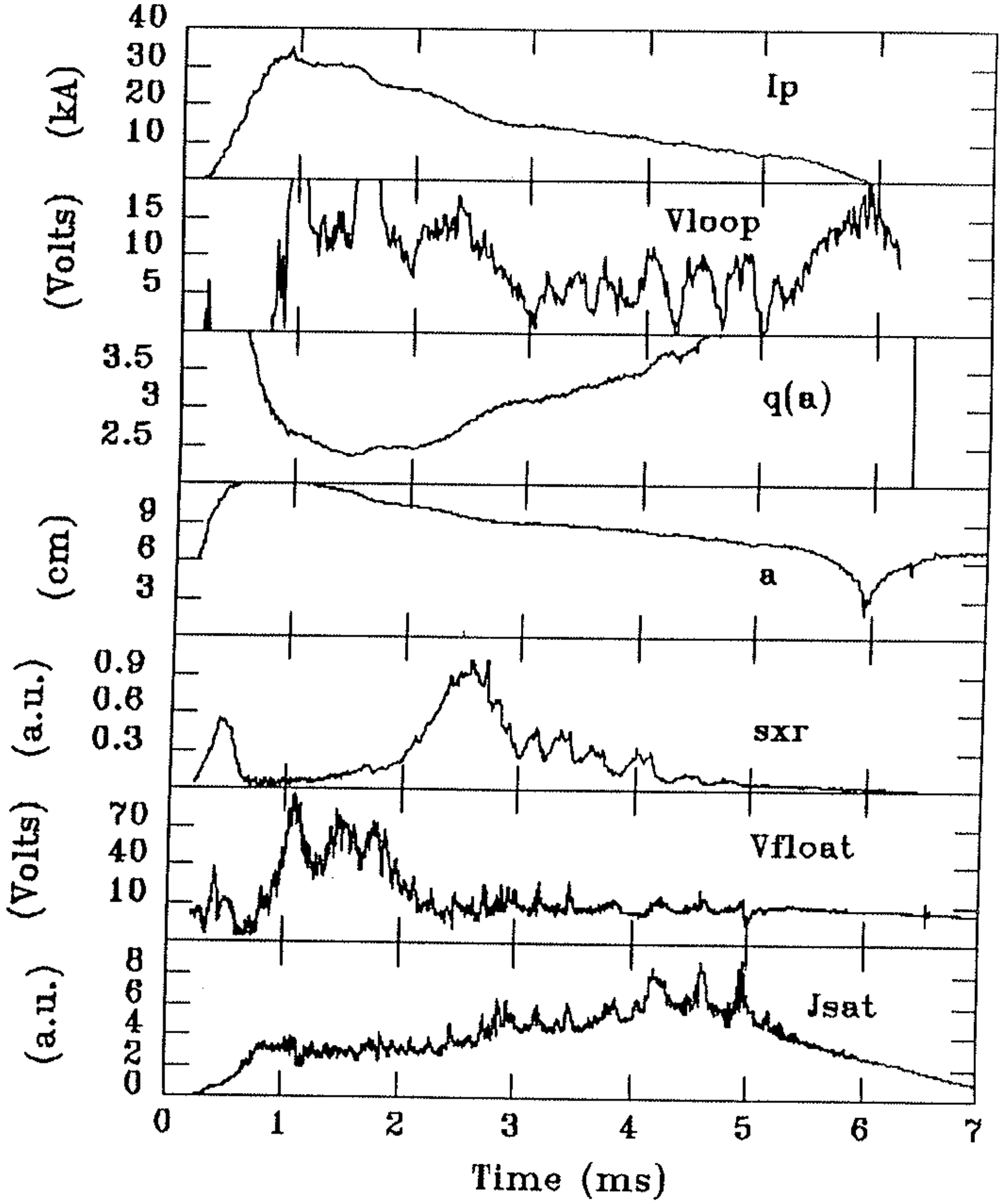

Fig. 4.1 *Global parameters of a <q(a)> = 3.0 discharge, limiters out. Shown are the plasma current, loop voltage, edge safety factor, plasma radius, central chord SXR signal, and floating potential and ion saturation current signals at r = 8 cm.*

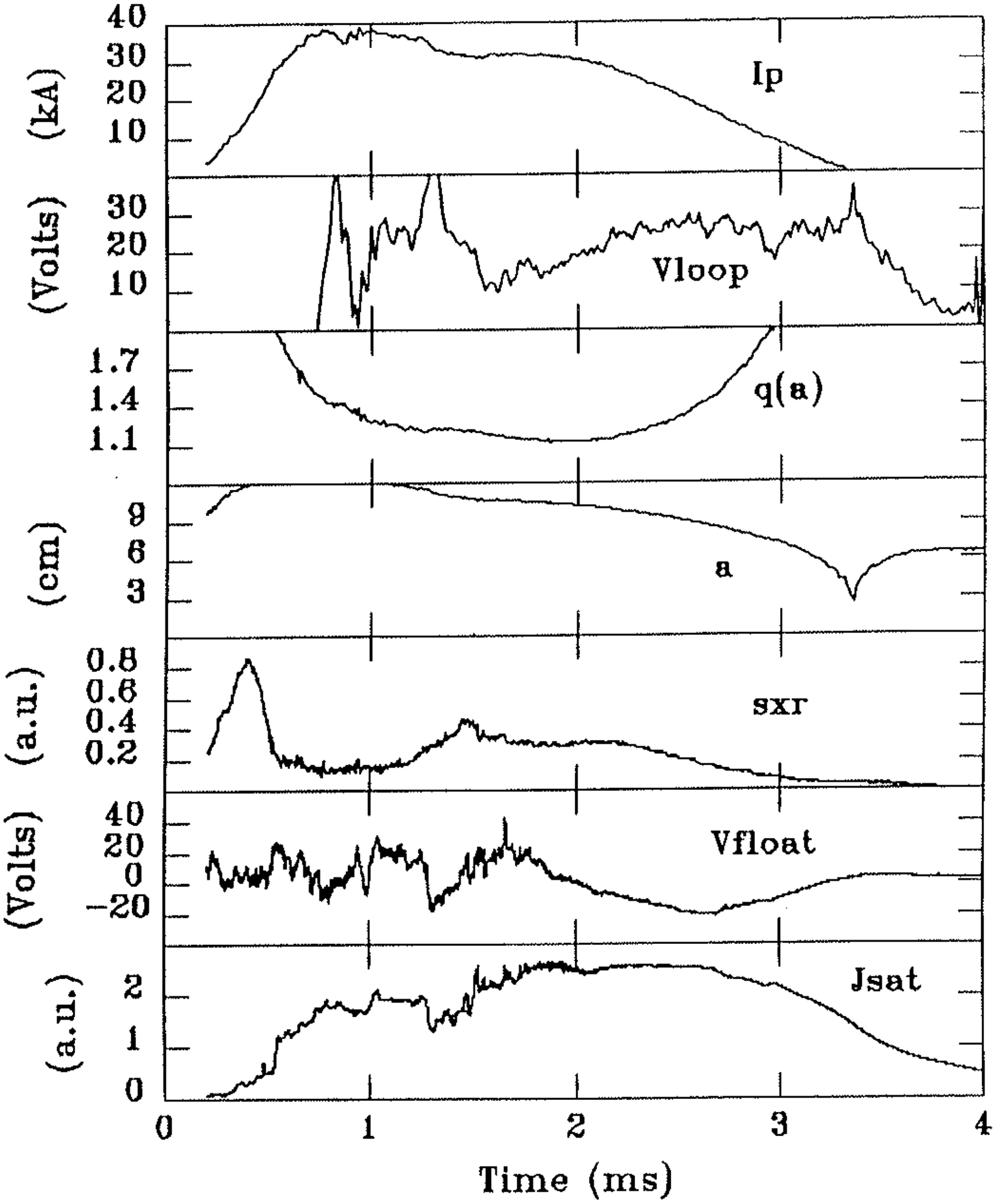

Fig. 4.2 Global parameters of a <q(a)> = 1.2 discharge, limiters out. Shown are: the plasma current, loop voltage, edge safety factor, plasma radius, central chord SXR signal, and floating potential and ion saturation current signals at r = 9 cm.

signals are shown for r = 9 cm, which is the innermost position the Langmuir probes could be inserted before having arcing problems. The toroidal field for this $\langle q_a \rangle = 1.2$ discharge was 3.2 kG.

Table 4.1 shows typical discharge parameters for the two extreme values of $\langle q_a \rangle$. Line averaged density and central electron temperatures are based on previous measurements and estimates.[1]

TABLE 4.1

Tokapole-II Parameters

	$\langle q_a \rangle \sim 1$	**$\langle q_a \rangle \sim 4$**
Toroidal field	~ 3kG	~ 5.5 kG
Plasma current	30-40 kA	~ 10 kA
Line avg. density	~ $10^{13}/\text{cm}^3$	~ $5\text{x}10^{12}/\text{cm}^3$
Central T_e	100 eV	120 eV
Pulse length	~ 4 msec	~ 8 msec
Loop Voltage	15 V	2 V
τ_E	0.05 msec	0.4 msec

It should be noted that the variation of $\langle q_a \rangle$ was made without fixing the plasma current or the toroidal field. Both parameters were varied in order to achieve an optimization of current duration and confinement times.

For fluctuation measurements, the time slices were taken after the peak of the SXR signals (after the initial heating phase) and before the beginning of current termination. During this time window, most quantities were approximately constant. In high $<q_a>$ discharges, sawtooth activity is present, so the bursts of fluctuation activity that sometimes accompany the sawtooth crashes are avoided in the choice of data segments.

Figure 4.3 shows the electron temperature and density profiles measured by the triple probe, for the four $<q_a>$ cases studied, during the time periods in which fluctuation data were taken. Energy confinement times were estimated using $\tau_E = W/IV$ where W is the stored energy $(3/2)\int(nk_BTe)dv$ integrated to the innermost position reached by the probes, and IV is the ohmic input power (plasma current I multiplied by loop voltage V). Central temperatures of (70-100) eV and central densities of $(1.5\text{-}3.0)\times10^{13}$ cm^{-3} are assumed, based on previous estimates[1] and "reasonable" plasma profile shapes. It was assumed that low $<q_a>$ discharges have flatter profiles due to their poor confinement. These confinement time estimates are reasonable to within factors of 2 or 3, and are accurate enough for our purposes of comparing the orders of magnitude of the energy flux with the fluctuation driven energy transport. The characteristic gradient scale length for the density is about $L_n \sim (3\text{-}5)$ cm in the edge region (the separatrix region shown in the figure). In the scrape-off region both temperature and density profiles are very flat.

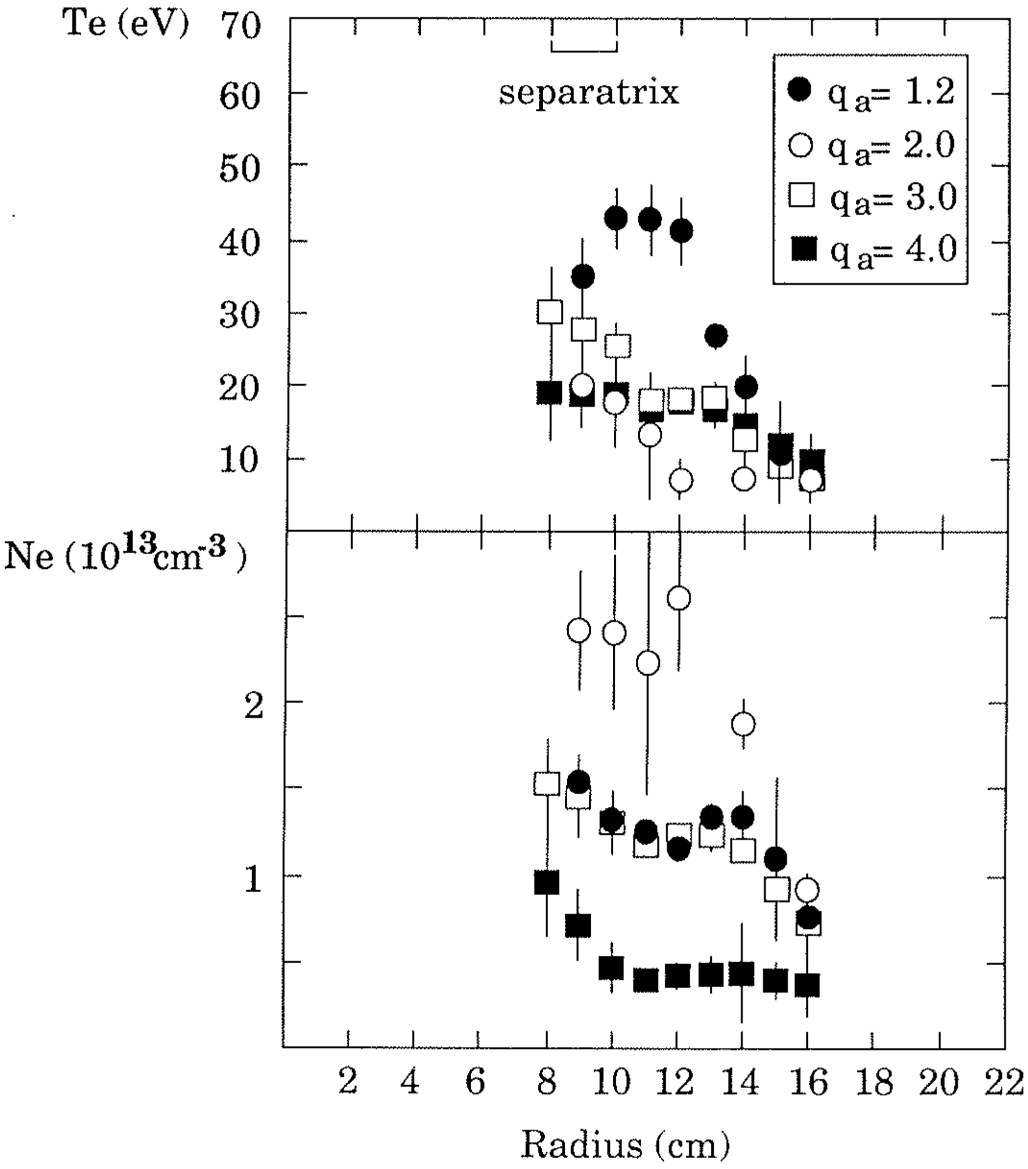

Fig. 4.3 Electron temperature and density profiles measured with a triple probe, for four <q(a)> cases, in magnetic limiter configuration.

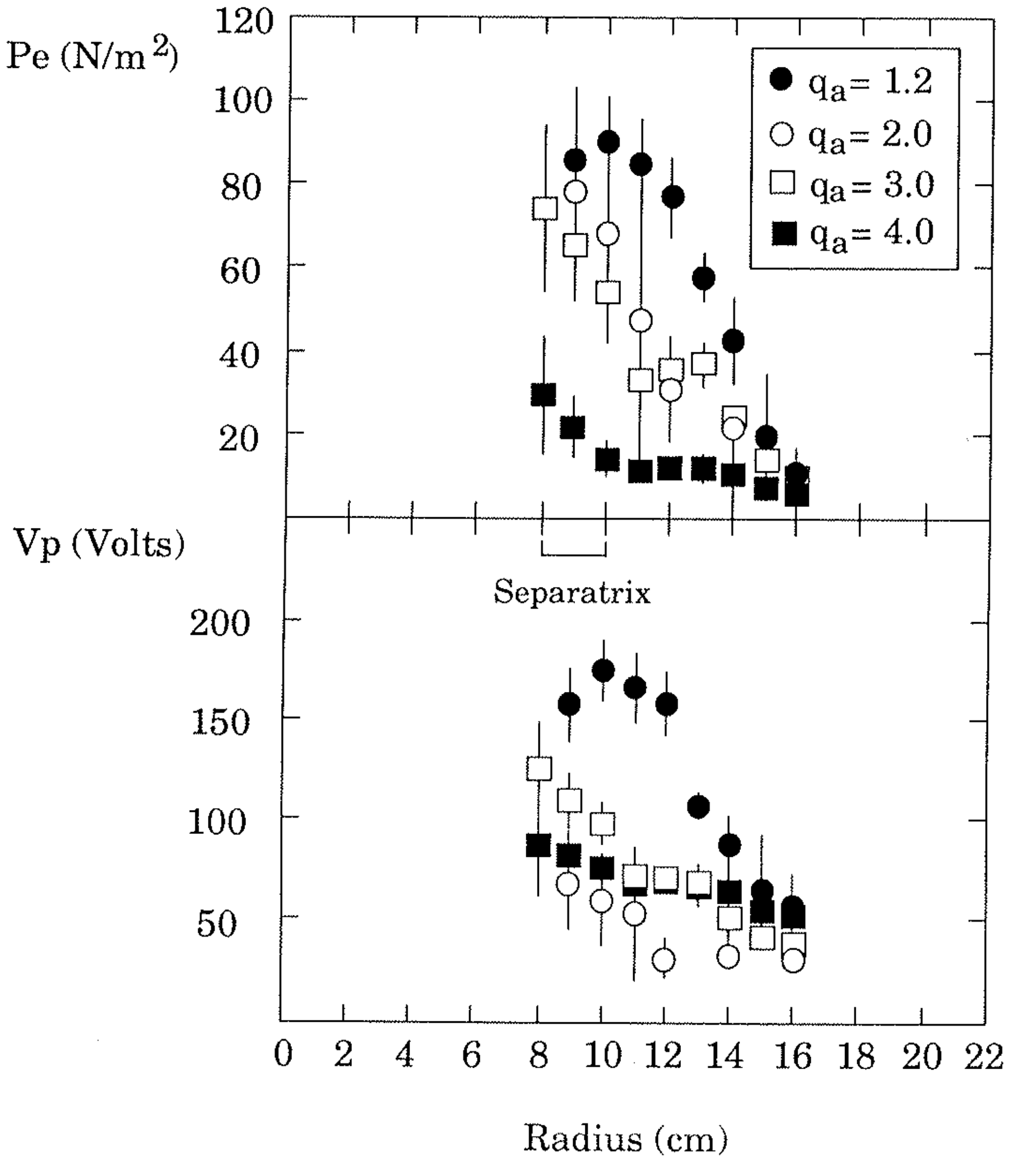

Fig. 4.4 Electron pressure and plasma potential profiles calculated from the profiles of fig. 4.3.

From these measurements, radial profiles of electron pressure and plasma potential were calculated, and are given in figure 4.4. The phase velocities of turbulent drift waves (diamagnetic drift velocities) measured in the laboratory frame are thought to be Doppler shifted by the E_r x B_T drift arising from the plasma potential gradients. It is therefore important to measure both drift velocities experimentally and compare with the measured phase velocities. Unfortunately, gradient quantities are difficult to measure, and due to the large error bars, it was not possible to calculate the electron diamagnetic drift and the E_r x B_T drift velocities (both around several km/sec) with sufficient accuracy to determine an average rotation velocity for the turbulent waves. Nevertheless, we can see that the plasma potential decreases monotonically with radius, and does not have a maximum (like is measured in other machines), so we should not expect to see a velocity shear layer, in contrast to other machine's results.

4.2 Electrostatic Turbulence Properties

4.2.1 Electron Temperature Fluctuations

As described in Chapter 3, the triple probe method for determining electron temperature fluctuations consists in measuring the difference between the positively biased tip of the double probe and the floating potential fluctuations, under the condition that they are in the same correlation volume.

In almost all cases, this condition was met in Tokapole-II, and the temperature fluctuations are measured to be very small. Figure 4.5 shows the high coherence level between $\tilde{V}_+$ and $\tilde{V}_f$, and their relative fluctuation levels, which practically overlap. An upper bound based on the error bars (due to statistical variations) would give $\tilde{T}_e/T_e \sim 0.4\ \tilde{n}/n \sim 0.2\ \tilde{V}_p/T_e$.

4.2.2 Fluctuation Amplitudes and Frequency Spectra

Radial profiles of electrostatic fluctuation levels for $<q_a> = 1.2, 2.0, 3.0$, and 4.0 are shown in figure 4.6. Density fluctuation levels are small (typically less than 10%) compared to the mixing length estimate $\tilde{n}/n = 1/(k_r L_n) \sim (20\text{-}60)\%$, assuming $k_r \sim k_\theta \sim (0.5\text{-}1.0)\ \mathrm{cm}^{-1}$ (see section 4.2.3), and $L_n \sim (3\text{-}5)$ cm. Potential fluctuation levels are generally smaller than 20%, and are comparable to density fluctuation levels, suggesting that the Boltzmann relation may hold for Tokapole-II. These rather small fluctuation amplitudes are in contrast to other machines results, which show much higher fluctuation levels. As we shall see in Chapter 5 this could be due to the absence of a material limiter in Tokapole-II. Many machines observe a non Boltzmann behavior of $\tilde{n}/n$ and $\tilde{V}_p/T_e$, although some exceptions have been reported,[2] and it is believed that potential fluctuations are affected by impurities . The fluctuation amplitudes are slightly higher in the scrape-off region due to the lower equilibrium values. No systematic dependence with the safety factor is observed.

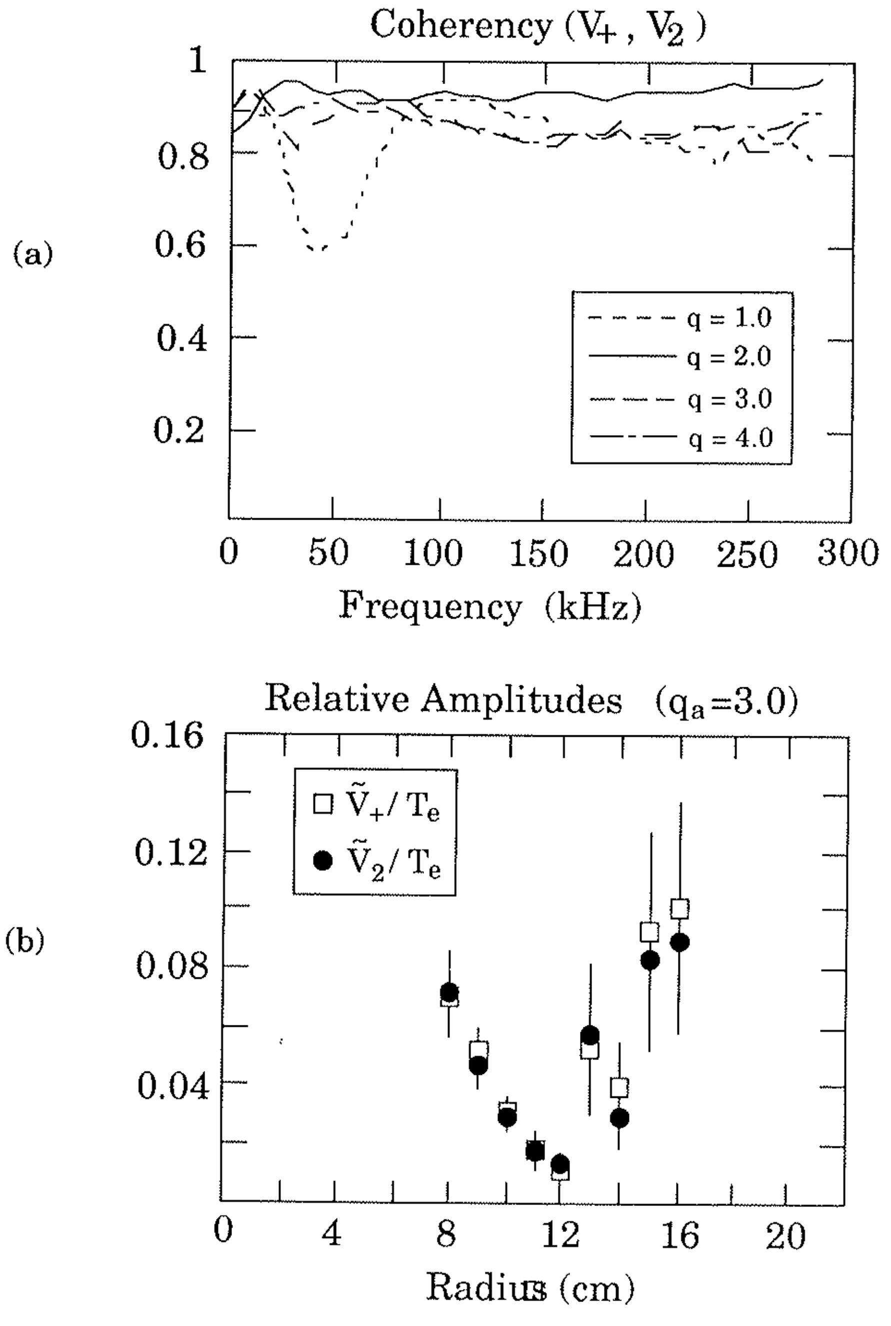

Fig. 4.5 *(a) Coherency between a floating potential and the positively biased tip of a double probe, for four <q(a)> cases, innermost positions, magnetic limiter configuration. (b) Fluctuation amplitude profiles of these two signals for a <q(a)> = 3 case.*

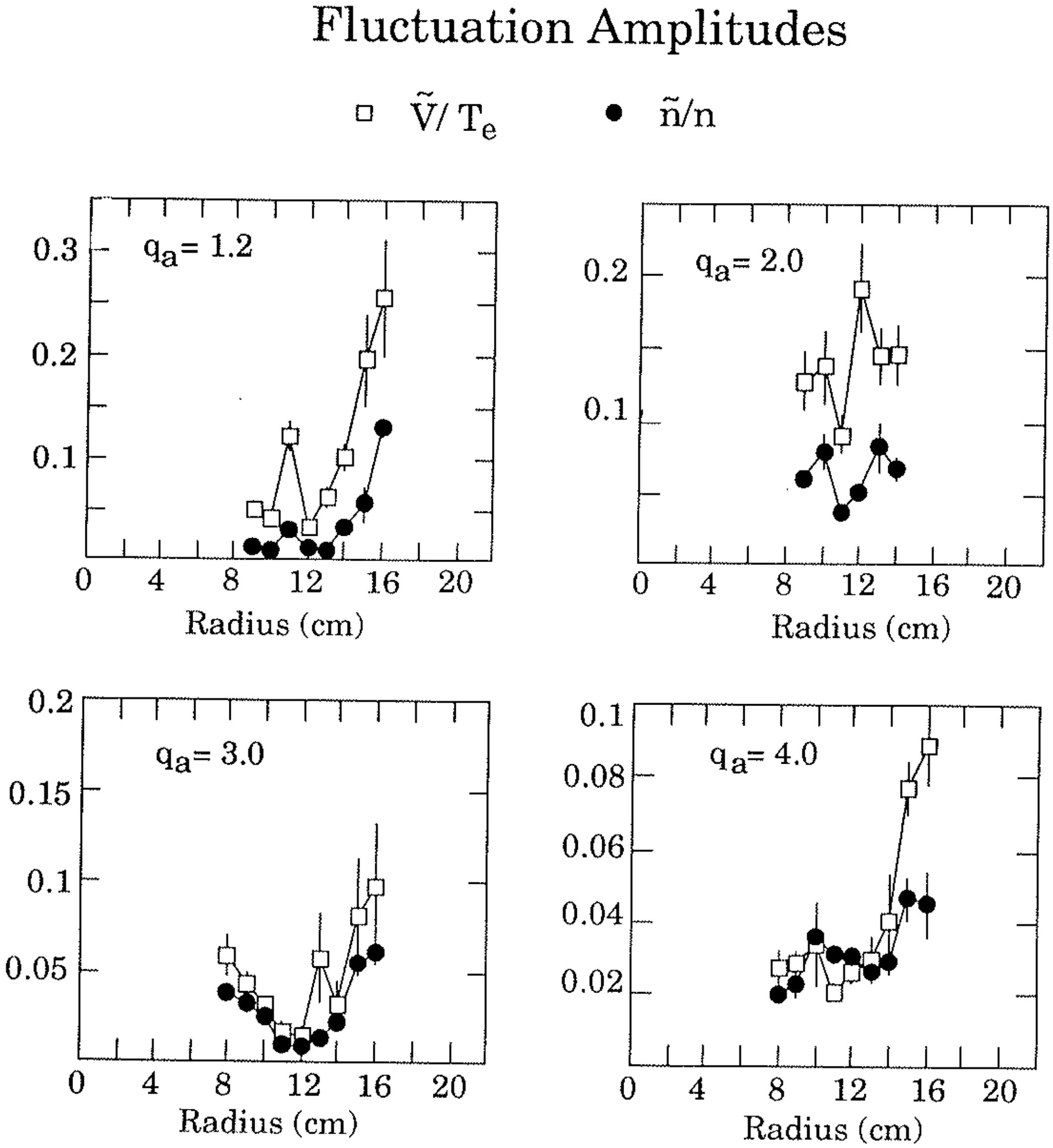

Fig. 4.6 Density and potential fluctuation level profiles for four <q(a)> cases, magnetic limiter configuration.

The frequency spectra (figure 4.7) show that both $\tilde{n}/n$ and $\tilde{V}_p/T_e$ decay monotonically with frequency : $\tilde{n}/n \;\alpha\; f^{-a}$, with a = (0.5 - 1.5) , and $\tilde{V}_p/T_e \;\alpha\; f^{-b}$ with b = (.5 - 2.0). These decay laws are independent of position and safety factor.

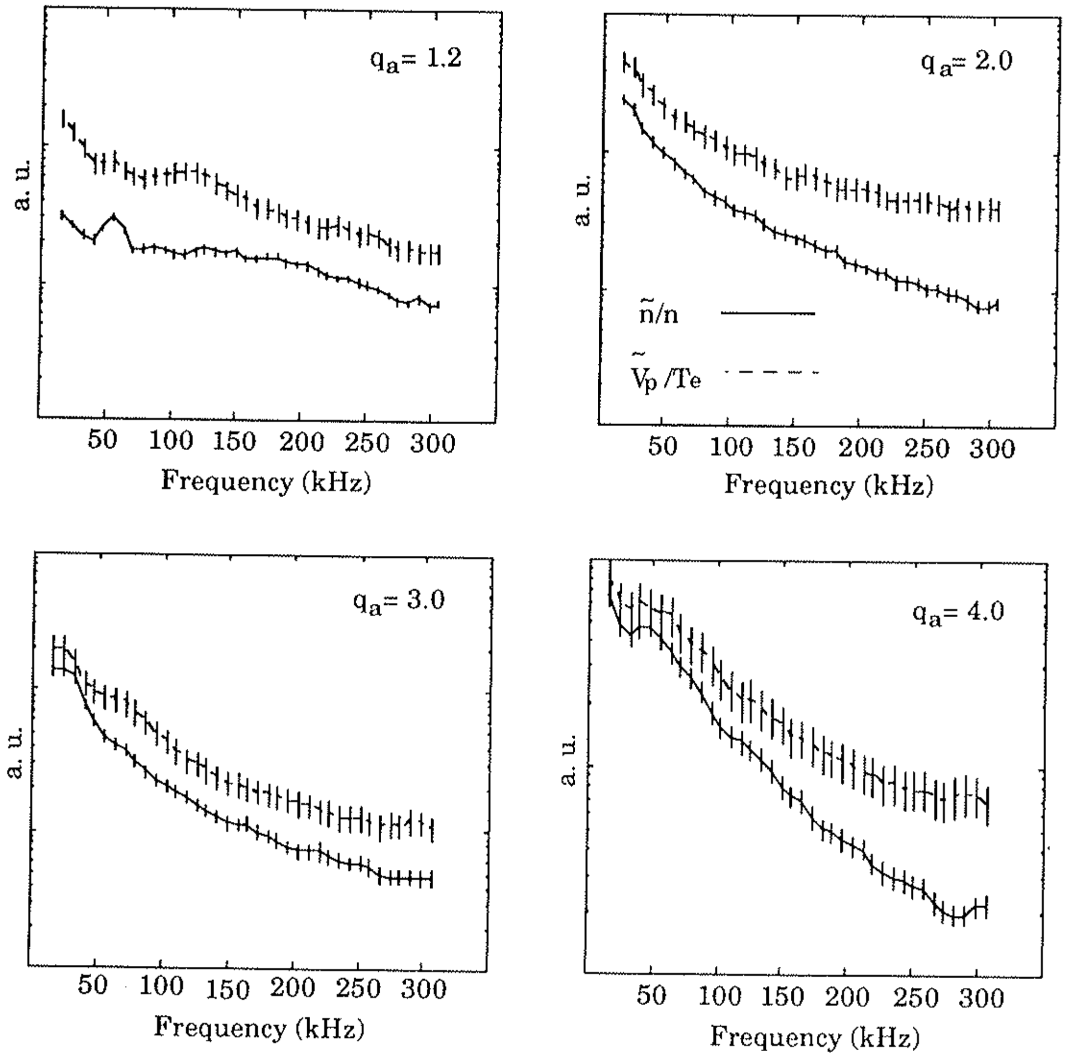

Fig.4.7 Frequency spectra of density and plasma potential fluctuations for the four <q(a)> values, innermost positions.

4.2.3 Structure of Potential Fluctuations

The spatial structure of the turbulence can be described by two point correlation measurements as described in Chapter 3. In spectral analysis, several hundred terms are usually necessary for a meaningful ensemble average measurement. Due to the relatively short discharge durations in Tokapole-II (especially in "low $<q_a>$" discharges) this meant taking 100 to 150 shots at a single position. Due to lack of time, it was not possible to make these measurements at all positions, so we decided that only the innermost position of each $<q_a>$ case ($r = 9$ cm for $q_a = 1.2$ and $q_a = 2.0$, and $r = 8$ cm for $q_a = 3.0$ and $q_a = 4.0$) would be studied in detail.

Figure 4.8 shows the coherencies between the two potential fluctuation signals (separated by 3 mm), for the four $<q_a>$ cases. The poloidal correlation lengths are $L_p \sim (0.6\text{-}2)$ cm, with no particular trend with respect to $<q_a>$. Correlation lengths can give an estimate of the spectral width from the relation $\Delta k_\theta = \pi/L_p$ .This gives $\Delta k_\theta \sim (1.5\text{-}5)$ which is comparable with the more accurate measurements of the spectral width described below.

A better description of the spatial structure of the turbulence can be given by the wavenumber-frequency spectrum $S(k,\omega)$, the wavenumber spectrum, the spectral width, and the dispersion relation shown in figures 4.9 and 4.10, for the two extreme $<q_a>$ values.

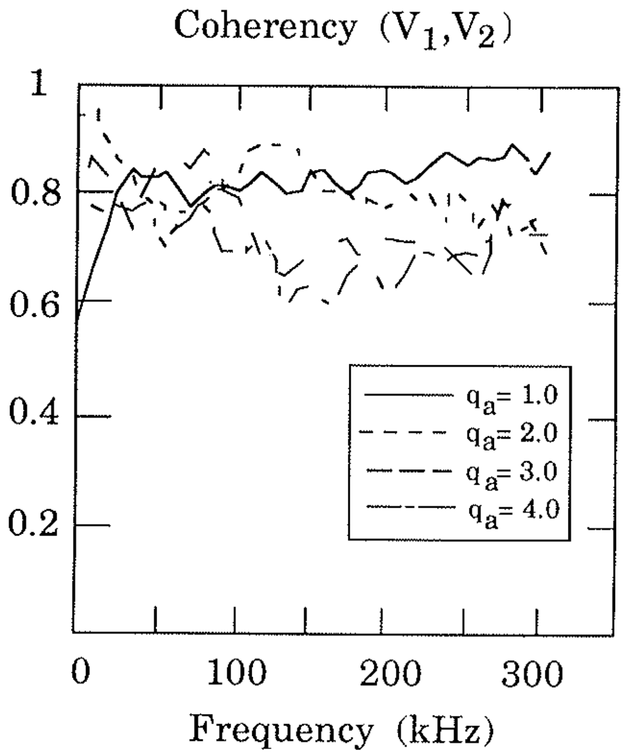

Fig. 4.8 Coherency between two potential fluctuation signals for four <q(a)> cases, innermost positions, magnetic limiter configuration.

The k_θ-spectra are broad ($\Delta k_\theta \sim 2 > k_\theta$), with most of the power concentrated at the lowest frequencies ($f < 100$ KHz) and lowest k_θ values ($k_\theta \sim (0\text{-}1)$ so that $k_\theta \rho_s \sim (0\text{-}0.2)$). Note that there is no predominant direction of propagation for $<q_a> = 1.2$ and only a slight shift towards the electron diamagnetic drift direction for the $<q_a> = 4.0$ case.

The k_θ spectra and spectral width of the potential fluctuations for other positions could not be determined with sufficient accuracy, since

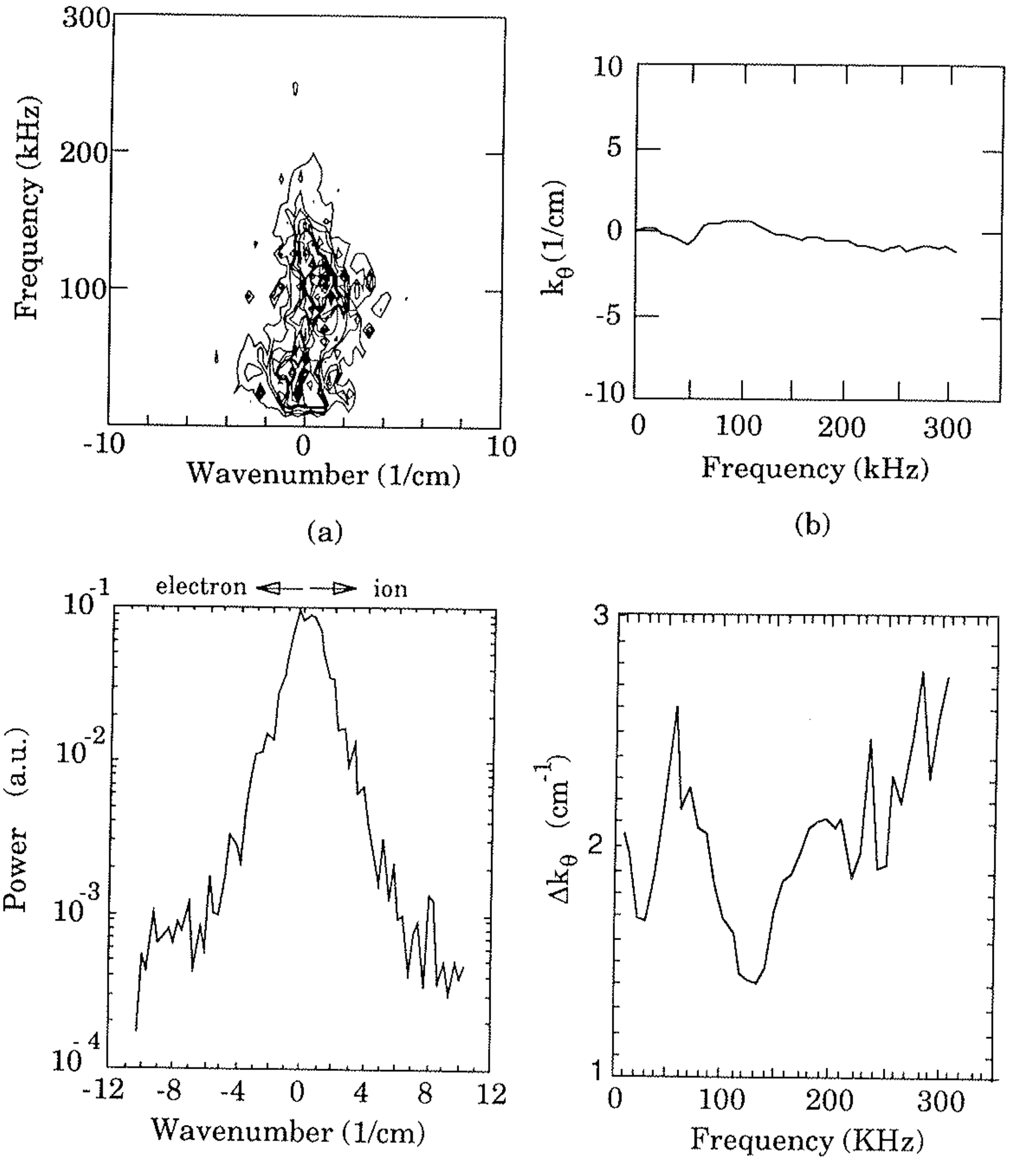

(a) (b)

(c) (d)

Fig.4.9 (a) Wavenumber-frequency spectrum S(k,ω), (b) Dispersion Relation, (c) k-spectrum and (d) k-spectral width for potential fluctuations, r = 9 cm, <q(a)> = 1.2, magnetic limiter configuration.

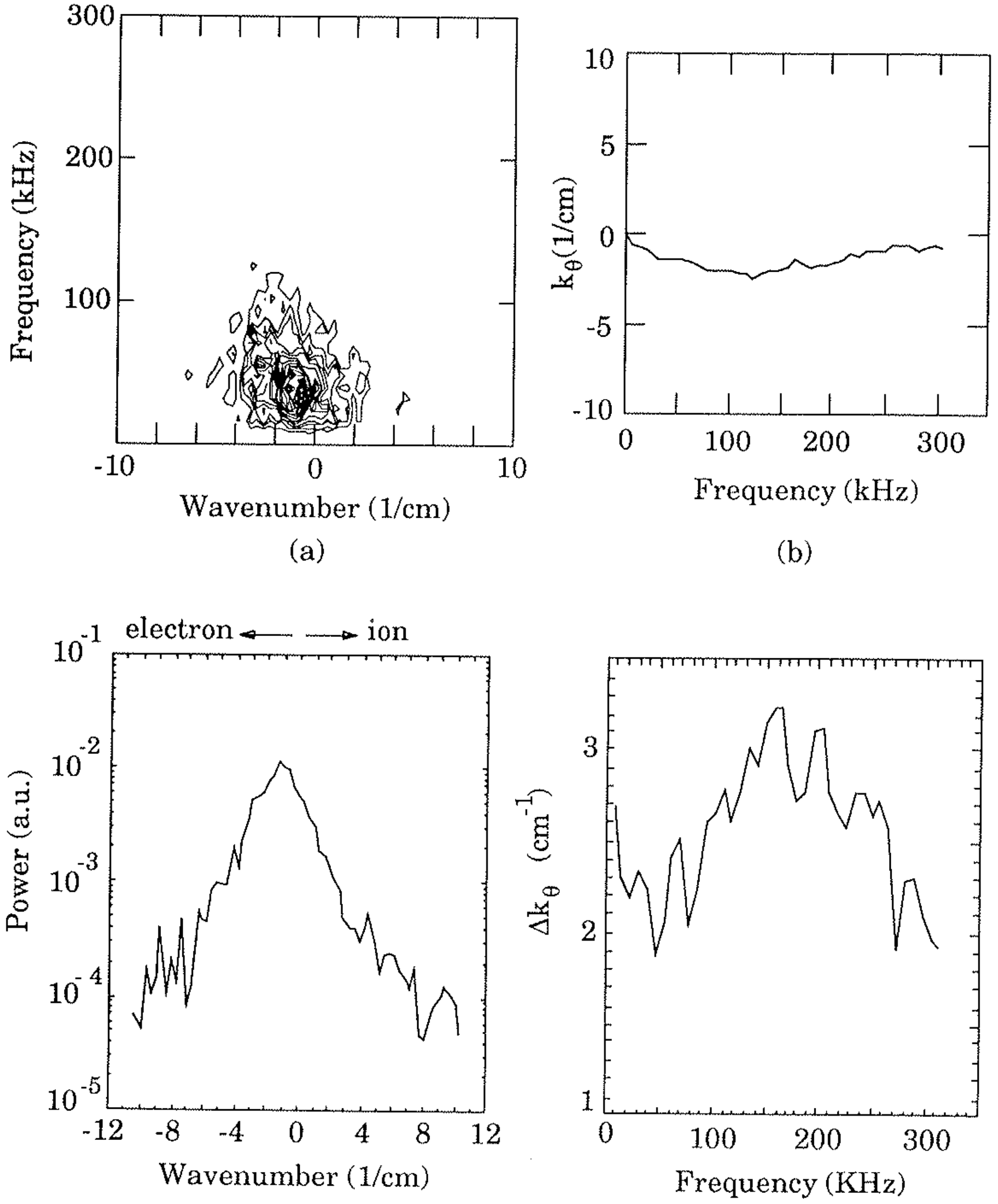

(a) (b)

(c) (d)

Fig. 4.10 *(a) Wavenumber-frequency spectrum $S(k,\omega)$, (b) Dispersion Relation, (c) k-spectrum and (d) k-spectral width for potential fluctuations, $r = 8$ cm, $<q(a)> = 4$, magnetic limiter configuration.*

only 20-60 terms were taken for each case. However, the data available (i.e., the sign of the phase between both floating potentials) indicate that in some cases in the scrape-off region, the direction of propagation is clearly in the electron diamagnetic drift direction. A clear propagation in the ion diamagnetic direction was never seen, so the available data does not show any evidence of a velocity shear layer, as it is seen in other machines.

4.3 Fluctuation Driven Transport

4.3.1 Energy Fluxes

Fluctuation driven energy and particle fluxes can be calculated from the density and the two potential fluctuation signals, using the proper spectral analysis described in Chapter 3.

The energy flux associated with electrostatic fluctuations is $Q=(3/2B)<\tilde{p}\tilde{E}>$. In our case, the pressure fluctuations are assumed to be due to the density fluctuations only, since the temperature fluctuations were measured to be small, so $Q=3/2k_BT_e\Gamma$, where Γ is the particle flux. The total energy loss rate is calculated assuming that the fluxes are poloidally symmetric and integrating over the area of a cylinder of length $2\pi R$ (R is the major radius). An up-down asymmetry was detected in the fluctuation amplitudes for high $<q_a>$ discharges (which are usually displaced 1 to 2 cm above the geometric center of the machine), but the amplitudes at the outer side are intermediate between the values at the top and bottom. Therefore, the transport measurements made at the outer side of the machine should give good average numbers for the integrated fluxes. At low $<q_a>$ discharges (which are usually centered vertically) no up-down asymmetries were detected in the amplitudes.

The plasma energy is estimated using the profiles measured with the probes. The results are shown in figure 4.10, which gives the energy fluxes calculated at the innermost positions (for outward and non negligible fluxes), the maximum energy fluxes (assuming optimum phase relations) calculated at other radii, and the total energy fluxes. It can be noticed that in all four cases the electrostatic fluctuation driven transport is at least two orders of magnitude too small to account for the energy confinement measured, even when optimum phase relations are invoked. It can also be noticed that there is no systematic dependence of the transport with the average safety factor.

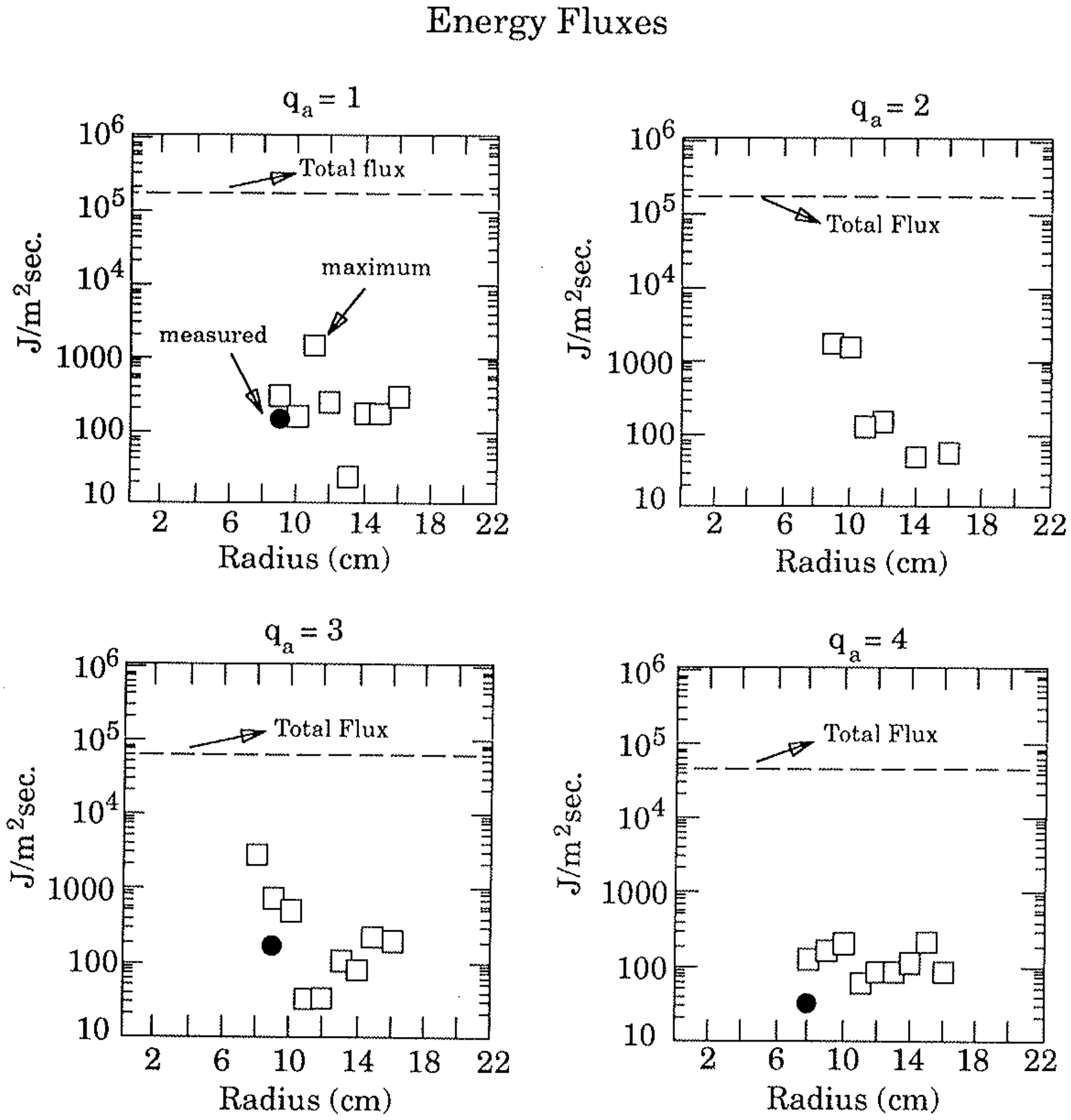
Energy Fluxes

Fig. 4.11 Energy fluxes due to electrostatic fluctuations: profiles for four <q(a)> cases, magnetic limiter configuration. Dark circles are measured fluxes (when not negligible) and white squares are maximum values (based on amplitudes only). Also shown are the total energy fluxes.

4.3.2 Particle Fluxes

The particle flux spectrum is given in spectral components by $\Gamma = \mathrm{Im}\langle n(f)^{*} k_{\theta}(f) V_{p}(f)\rangle / B_{T}$. This statistical quantity depends on the phase relations between the three measured signals. A coherency of 1 and a 90 degrees phase shift between $\tilde{n}$ and $\tilde{V_p}$ would give the maximum transport given by $\Gamma_{max} = \tilde{n}(f)\,\tilde{E}(f)/B_{T}$, where $\tilde{E}(f) = \langle (k_{\theta}(f) V_{p}(f))^{2}\rangle^{1/2}$ is the fluctuating electric field. Figure 4.11 shows the total particle flux (integrated from 15 kHz to 300 kHz and taken at the innermost positions) and their maximum values as a function of $\langle q_a \rangle$. The particle fluxes measured are small and outwards, in the range of 10^{19} part./m^{2}sec., about 2 orders of magnitude smaller than other machines.[3,4] Even when maximum phase relations are invoked the upper limits are in the range of 10^{20} part./m^{2}sec.

The fluxes are outwards and sometimes negligible (in a few cases a net inward flux is measured but with error bars larger than 100% due to the small phases involved). When the flux is outwards and in the edge region, the frequency spectrum decreases monotonically, peaking at the lowest frequencies (fig.4.12.a). In the scrape-off region, higher frequency components contribute to the transport (fig.4.12.b). The inward fluxes sometimes measured are actually due to low frequency peaks with large error bars (fig.4.12.c), or a net inward flux resulting from a spectrum fluctuating in frequency between negative and positive values, all with large error bars (fig.4.12.d).

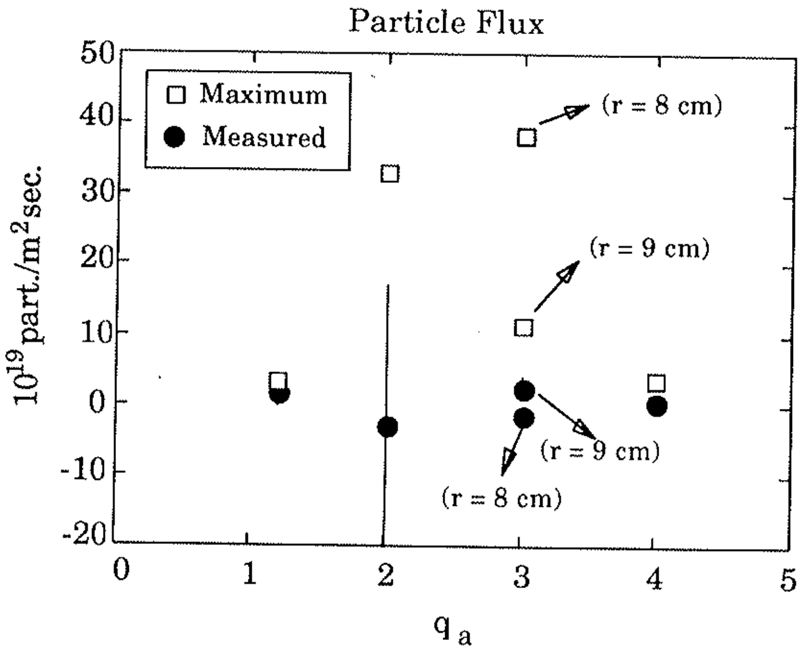

Fig. 4.12 Particle Fluxes for four <q(a)> cases, innermost positions (except for <q(a)> = 3), magnetic limiter configuration. Dark circles are measured values and white squares are maximum estimates, based on amplitudes only.

As described in Chapter 3 the particle flux depends on the phases between density and potential fluctuations, as well as their coherency levels. Figure 4.13 shows the coherency levels and the phases between the two fluctuating quantities, for the 4 $<q_a>$ cases. The fluctuations are not very coherent ($\gamma_{nv} < 0.6$) , and their phase shifts are about 30 degrees at higher frequencies, and close to zero for lower frequencies where most of the power is concentrated. These small phases introduce large uncertainties in the fluctuation induced flux calculations (but are not large if compared to the total energy flux).

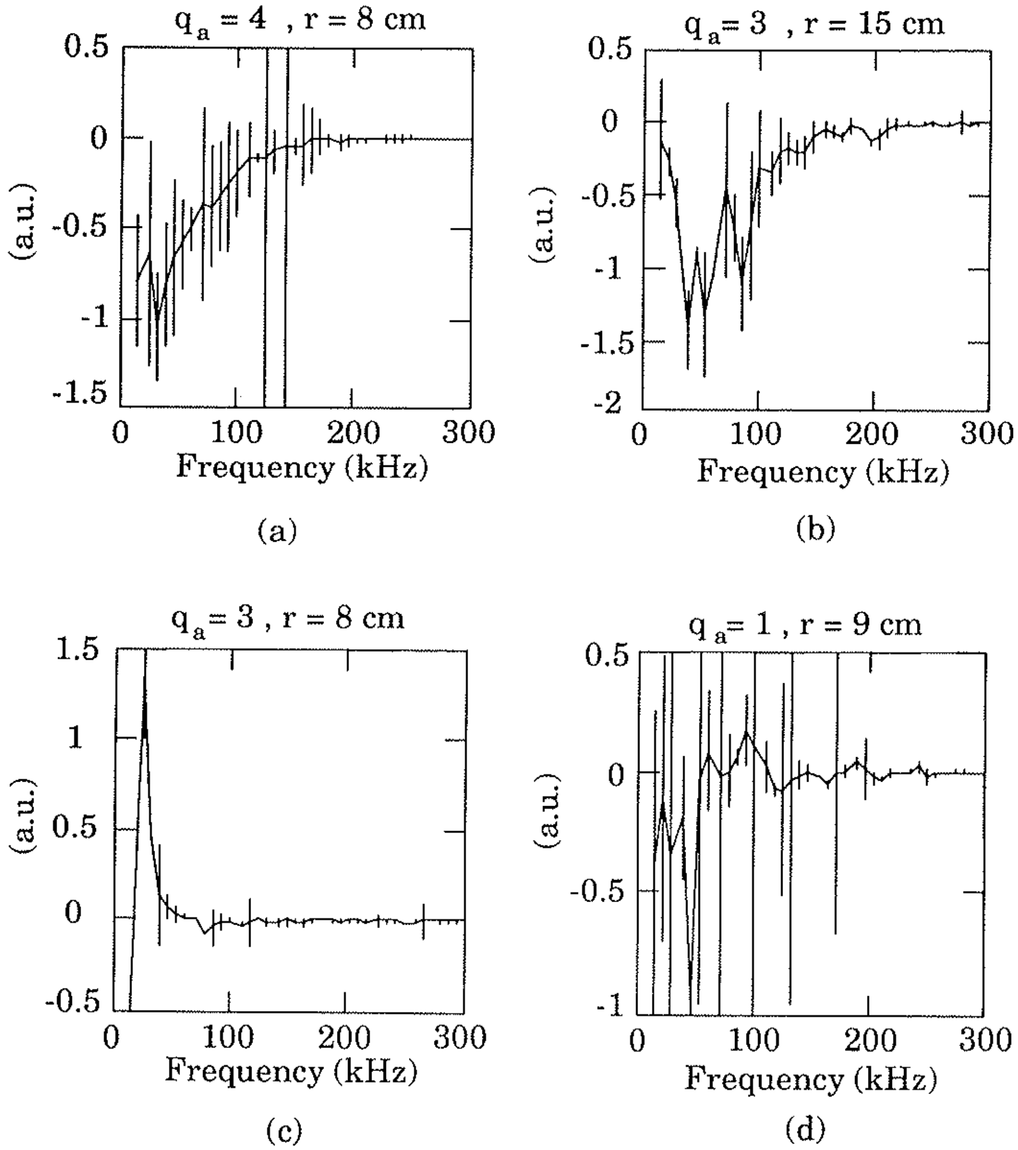

(a) (b)

(c) (d)

Fig. 4.13 Particle flux frequency spectra (outward flux is negative):
(a) outward flux, edge region
(b) outward flux scrape-off region
(c) "inward flux", with low frequency peaks
(d) "zero flux",

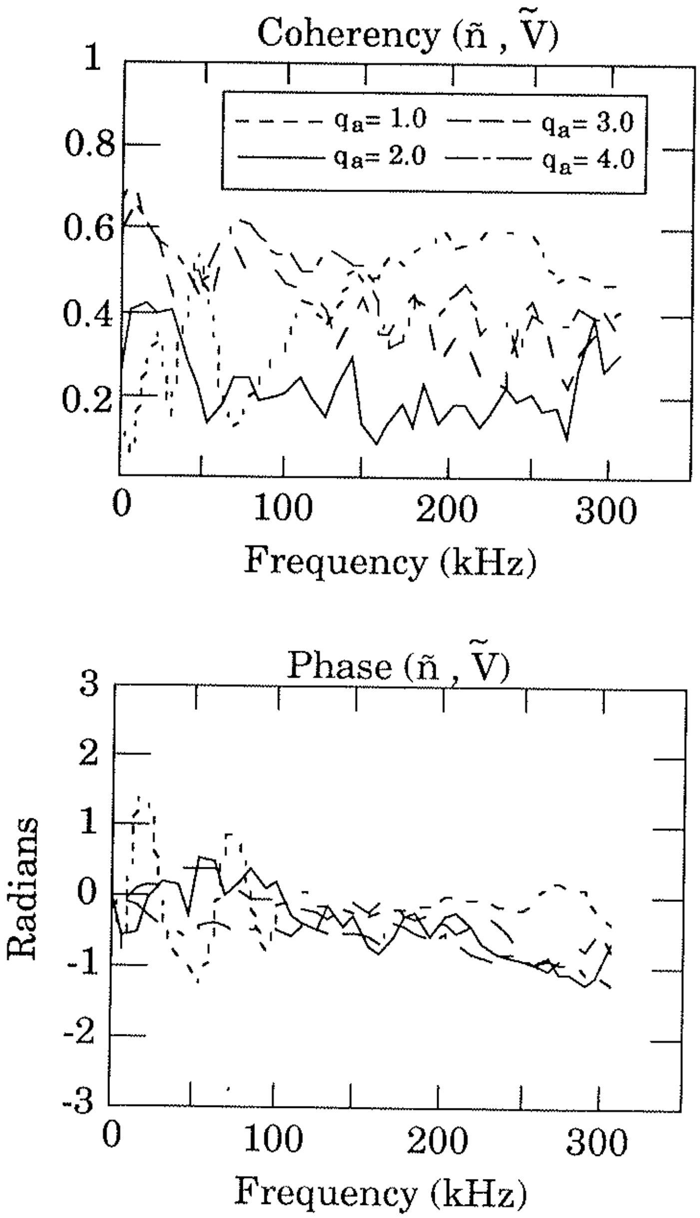

Fig. 4.14 Coherencies and phases between density and potential fluctuation signals, for four <q(a)> cases, innermost positions.

The diffusion coefficients associated with the measured particle fluxes are $D = -\Gamma/(dn/dr) \sim 3\times10^3$ cm^2/sec. To compare the measured particle flux with the actual particle confinement time it would be necessary to make a particle balance analysis based on the sources (usually measured from H_a light emission) and sinks (parallel flow to the limiter) present at the edge. Unfortunately Tokapole-II was not equipped with the necessary diagnostics, but in general particle and energy confinement times are comparable in magnitude. Therefore the role of electrostatic fluctuations on transport can be inferred from energy confinement time measurements, which showed that electrostatic turbulence is at least two orders of magnitude too small to explain the energy losses.

This was a rather puzzling result, considering that many tokamaks explain anomalous losses with electrostatic turbulence. An attempt to explain this behavior was made by inserting a material limiter in the outer edge of Tokapole, since most tokamaks operate with either a limiter or a divertor plate in the scrape-off region. The results of material limited discharges are presented in the next chapter.

References

1. Moyer, R. A., Ph.D. thesis, University of Wisconsin-Madison (1988).

2. Bengston, R. D., et al., 17th EPS Conf. on Controlled Fusion and Plasma Heating, Amsterdam **14B** (1990), p. 1460.

3. Ritz, Ch. P., et al., Nuc. Fusion **27** (1987), 1125

4. Levinson, S. J., Beall,J. M., Powers, E. J., Bengston, R. D., Nuc. Fus. **24** (1984), 527

CHAPTER 5

Limiter and Edge Gradient Effects on Electrostatic Fluctuations

The effects of the insertion of a material limiter in the outer edge on the electrostatic fluctuations is described in this chapter. In high $<q_a>$ discharges the density gradient was increased with the insertion of the limiter and that presumably caused an observed increase in the fluctuations. The two cases studied will be presented: first in discharges with $<q_a> = 3.5$, where a significant enhancement of the fluctuations is seen, together with a large increase in the density gradient, then in discharges with $<q_a> = 1.4$, where these effects were not observed.

5.1 "High $< q_a >$" Discharges with Material Limiters

Figure 5.1 shows the temporal evolution of global parameters for a discharge with $<q_a> = 3.5$ with a material limiter inserted in the outer edge up to r = 10 cm. These discharges are similar to the magnetically limited "high $<q_a>$" discharges, but have shorter duration. The Jsat signal shown is at r = 9 cm. It is readily noticed that the fluctuation amplitudes were greatly enhanced in this position, compared to the case without limiters.

The insertion of the material limiter had a marked effect in the

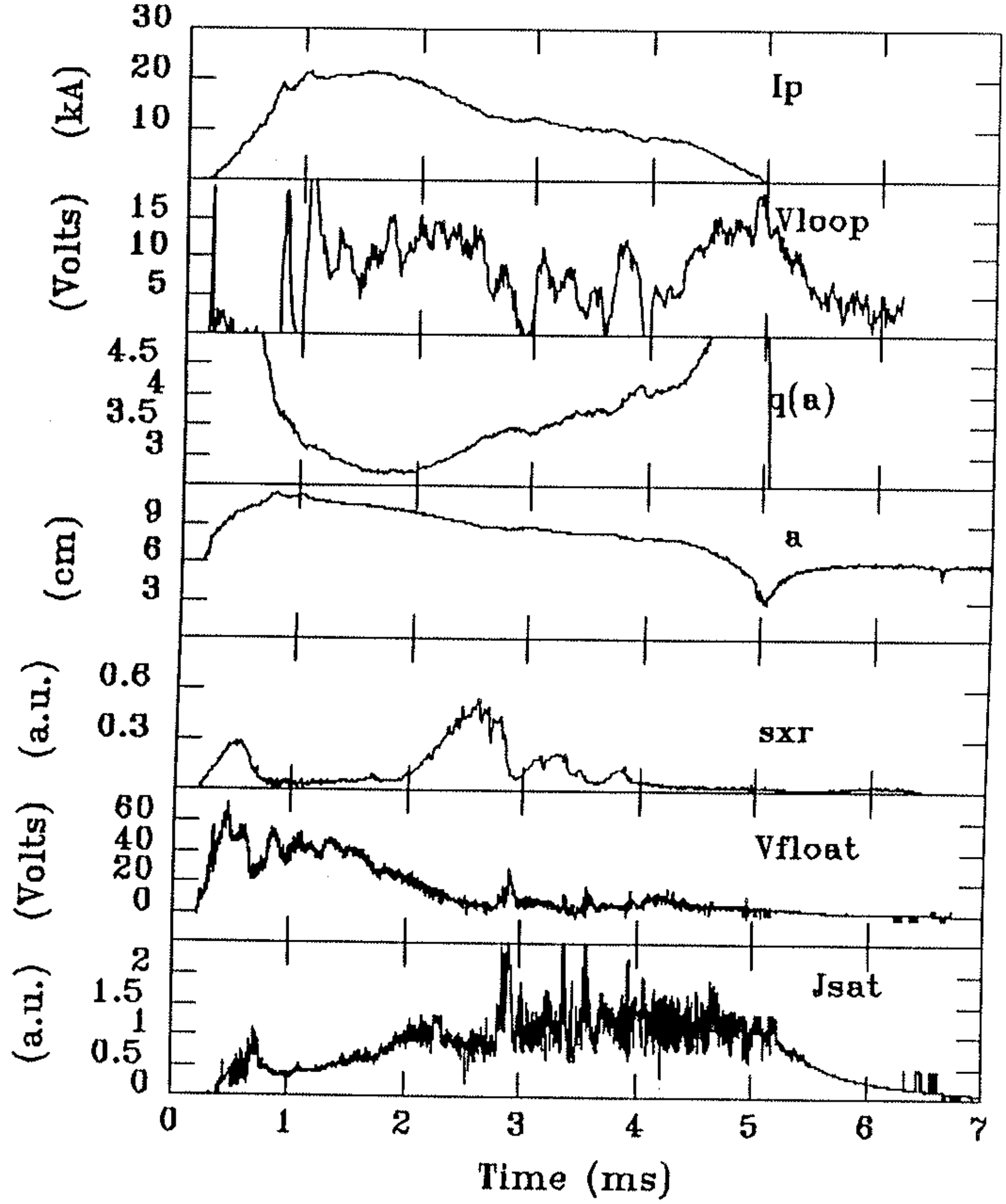

Fig. 5.1 Global parameters of a <q(a)> = 3.5 discharge, outer limiter in at r = 10 cm. Shown are: the plasma current, loop voltage, edge safety factor, plasma radius, central chord SXR signal and floating potential and ion saturation current signals at r = 9 cm.

density gradients as can be seen in the radial profiles of temperature and density shown in figure 5.2. The limiter caused a very sharp steepening in the density profile. The density gradient scale length at $r = 9$ cm is $L_n \sim 1.7$ cm compared with $L_n \sim 3\text{-}5$ cm in the magnetic limiter cases. No noticeable change occurred in the temperature profile. The steepening of the density profile was reflected in the pressure profile shown in figure 5.2. A slight increase in the gradient of the plasma potential is also seen at $r = 9$ cm, and we can see that no peak in the plasma potential profile is seen (no shear layer).

The radial profiles of the fluctuation amplitudes is shown in figure 5.3. It is somewhat remarkable that a large enhancement in the fluctuation amplitudes occurred exactly where the density gradient was steepest ($r = 9$ cm), and it occurred at that location only. This enhanced fluctuation level is now comparable to the mixing length estimate $\tilde{n}/n = 1/(k_r L_n) \sim 16\%$, where $k_r \sim k_\theta \sim 3$ cm^{-1}. At other positions no changes were observed .

Another important change that occurred at $r = 9$ cm was in the spatial structure of the fluctuations. The turbulent waves now propagate clearly in the electron diamagnetic drift direction, with the k_θ-spectrum peaking at $k_\theta = 3$ cm^{-1}. This is shown in the wavenumber-frequency spectrum and k_θ-spectrum shown in figure 5.4. This shift in the direction of propagation could be due to the steepening of the density gradient, which would increase the electron diamagnetic drift velocity.

The particle and energy flux (integrated over 15-300 kHz) profiles is shown in figure 5.5, together with the total energy flux calculated

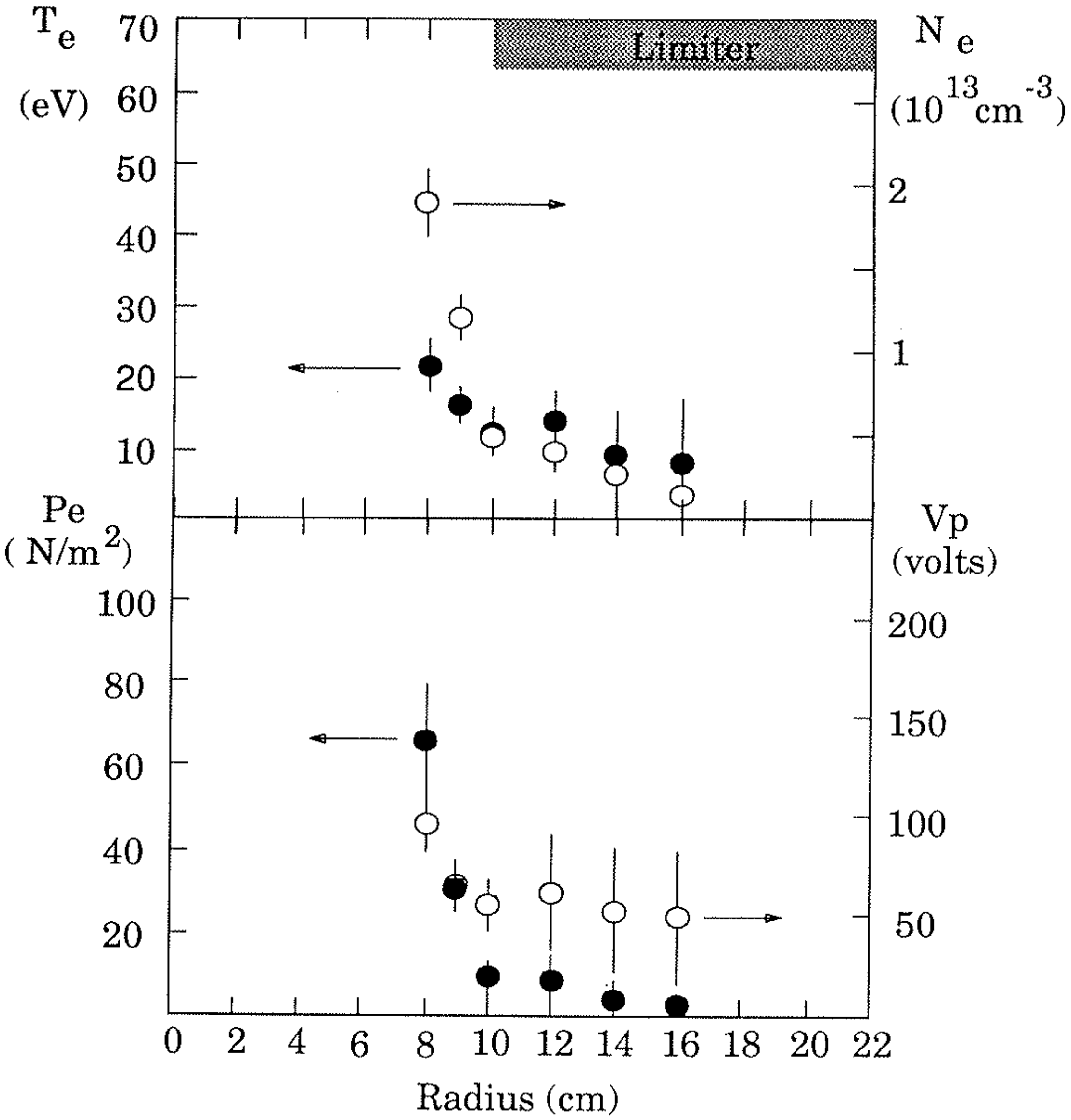

Fig. 5.2 Electron temperature, density, pressure and plasma potential profiles measured by a triple probe, for <q(a)> = 3.5, outer limiter in.

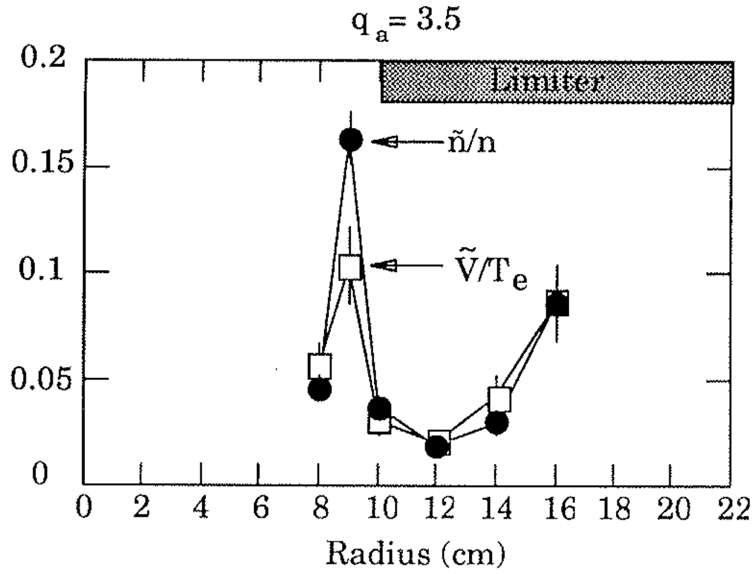

Fig. 5.3 Radial profiles of density and potential fluctuation levels, <q(a)> = 3.5, outer limiter in.

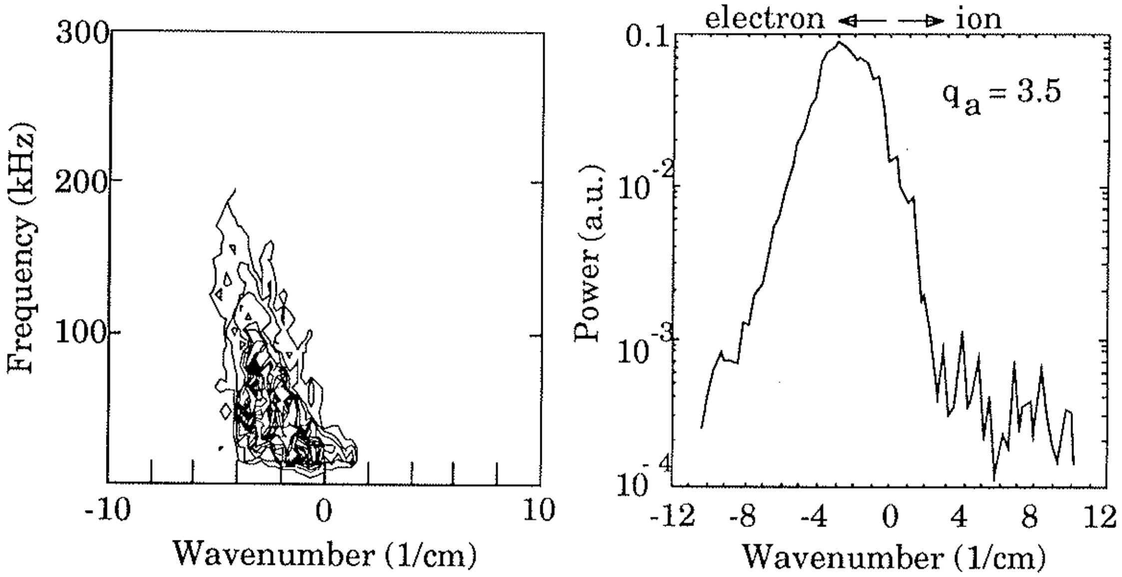

Fig. 5.4 Wavenumber-frequency spectrum S(k, ω) and k-spectrum of potential fluctuations, <q(a)> = 3.5, r = 9 cm, outer limiter in.

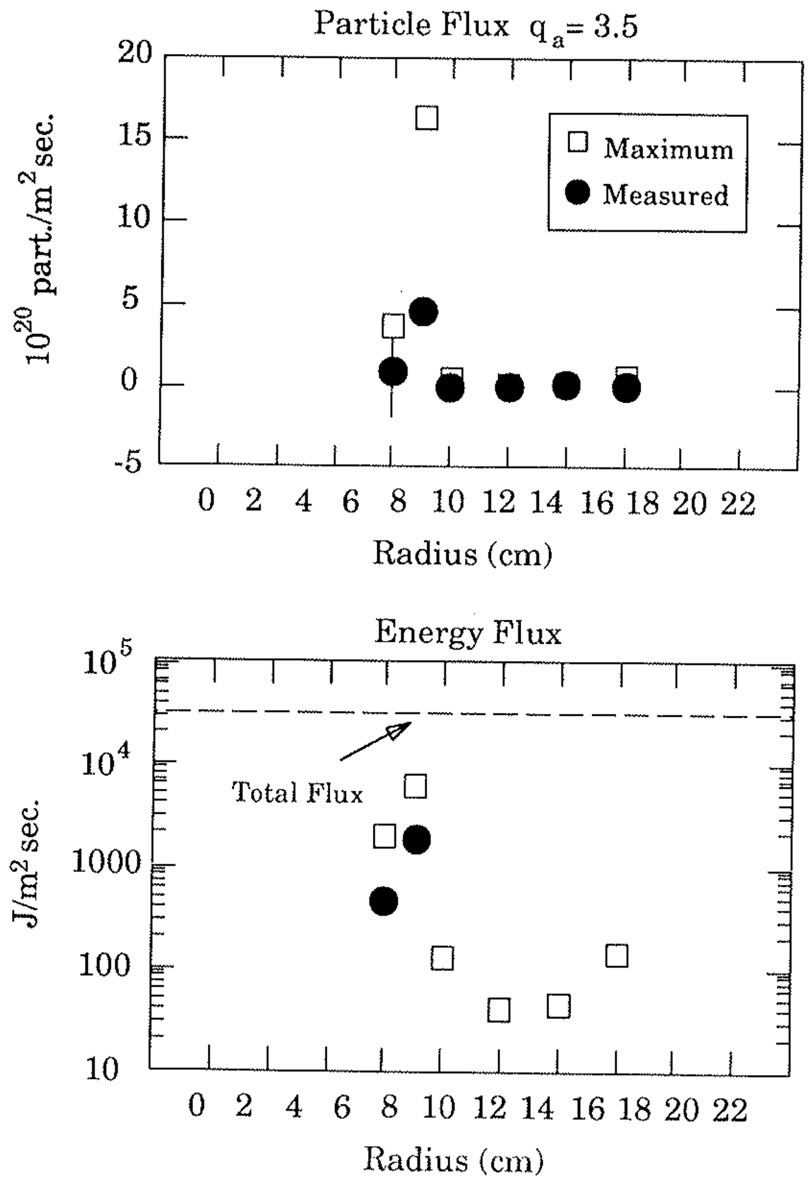

Fig. 5.5 Particle and energy flux profiles for <q(a)> = 3.5, outer limiter in. Also shown is the total energy flux.

from the measured energy confinement times. Despite the increase in the particle transport due to the increase in the fluctuation amplitudes at $r = 9$ cm, the corresponding energy flux is still a factor of 10 too small compared with the total flux. An upper limit in the energy flux (assuming perfect correlation and no phase shift between $\tilde{n}$ and $\tilde{E}$) would still be about 3 times too small. At other positions the results are similar to the magnetic limiter case.

This limited high $<q_a>$ result is not inconsistent with other machines observations. It has been reported in TEXT[1] that in their low density discharges ($\bar{n} < 2 \times 10^{13} cm^{-3}$) the convected energy loss could only account for 15% of their energy losses.

5.2 "Low $< q_a >$" Discharges with Material Limiters

Figure 5.6 shows a $<q_a>=1.4$ discharge with the outer limiter inserted up to $r = (10.5 - 11.0)$ cm. The global parameters do not differ much from magnetically limited "low $<q_a>$" discharges.

In this case a steepening of the density profile was not seen as in the "high $<q_a>$ " case, but the temperature gradient was somewhat increased, and as a result the pressure gradient at the edge was actually comparable to the limited $<q_a> = 3.5$ case. The plasma potential profile does not have a maximum, so no shear layer is observed. The electron temperature, density, pressure and plasma potential profiles are shown in figure 5.7.

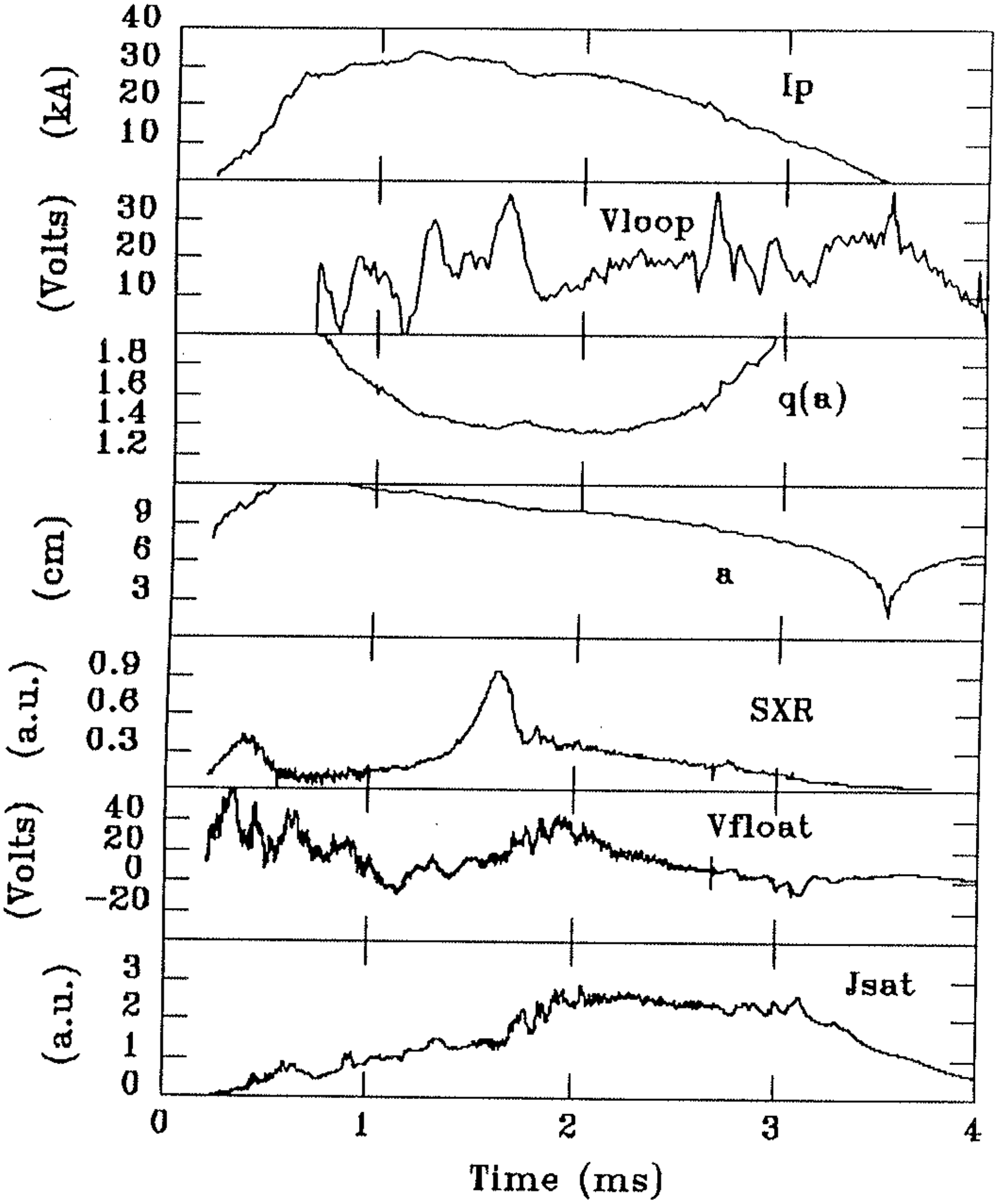

Fig. 5.6 *Global parameters of a <q(a)> = 1.4 discharge, outer limiter in at r = 10 cm. Shown are: the plasma current, loop voltage, edge safety factor, plasma radius, central chord SXR signal and floating potential and ion saturation current signals at r = 9 cm.*

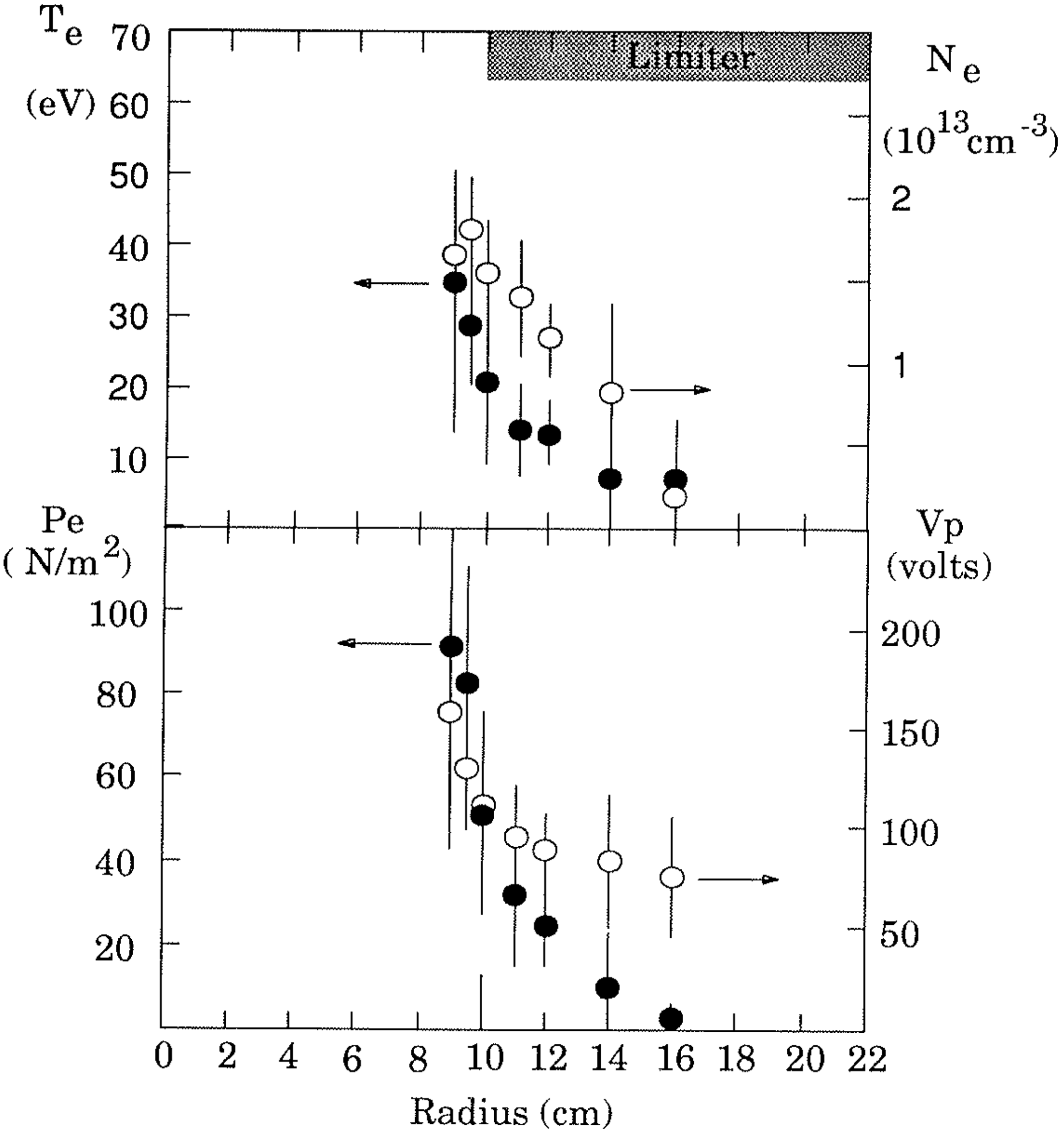

Fig. 5.7 Electron temperature, density, pressure and plasma potential profiles measured by a triple probe for <q(a)> = 1.4, outer limiter in.

The radial profiles of the fluctuation amplitudes are shown in figure 5.8. No enhancement is seen in any position. The large relative amplitudes in the scrape-off region was due to the very low equilibrium densities there. The wavenumber-frequency spectrum (figure 5.9) again shows a broad spectrum with the power concentrated at low frequencies ($f < 100$ kHz) and low k_θ ($k_\theta \sim .5\ \mathrm{cm}^{-1}$). The particle and energy flux profiles are shown in figure 5.10. Like the magnetically limited cases the fluctuation driven transport is 2 orders of magnitude too small, even with optimum phase and correlation relations.

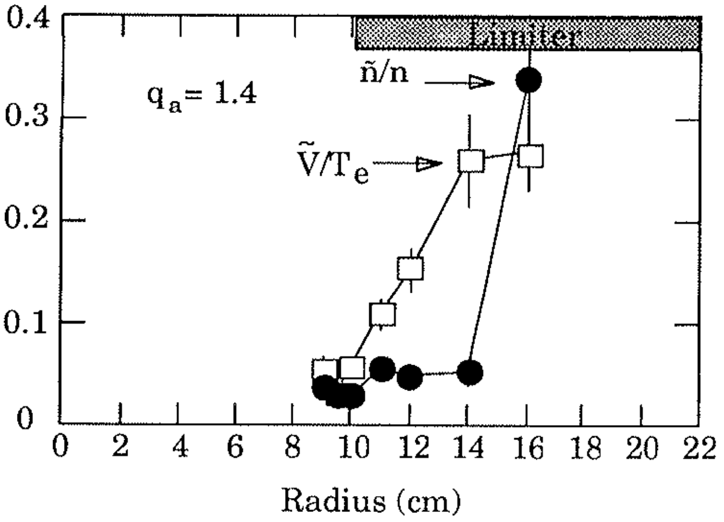

Fig. 5.8 Radial profiles of density and potential fluctuation levels for <q(a)> = 1.4, outer limiter in.

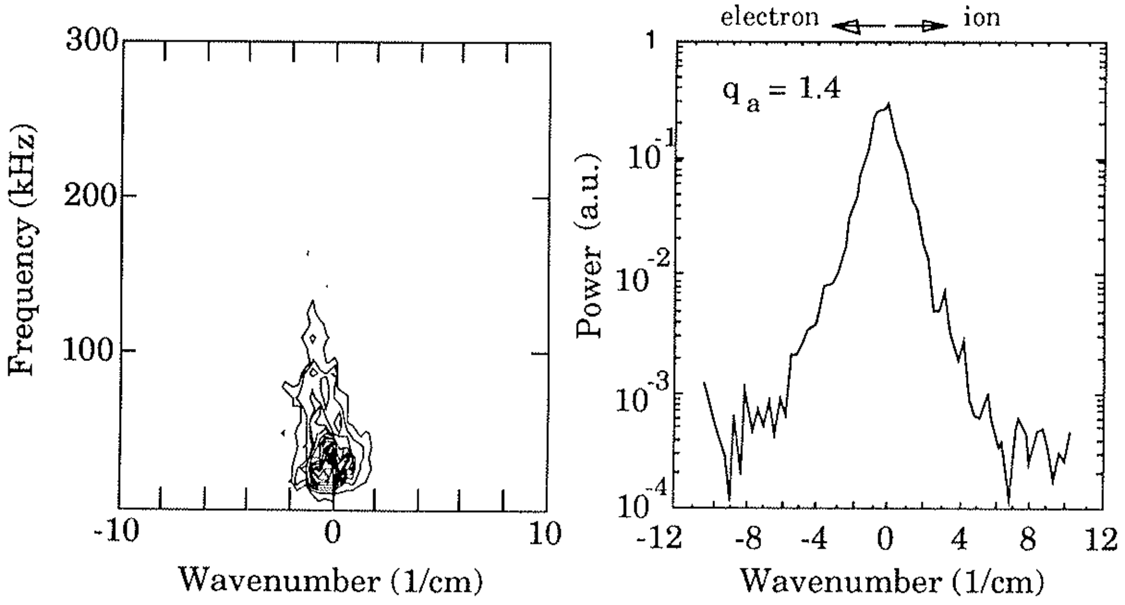

Fig. 5.9 Wavenumber-frequency spectrum S(k,ω) and k-spectrum of potential fluctuations, <q(a)> = 1.4, r = 9 cm, outer limiter in.

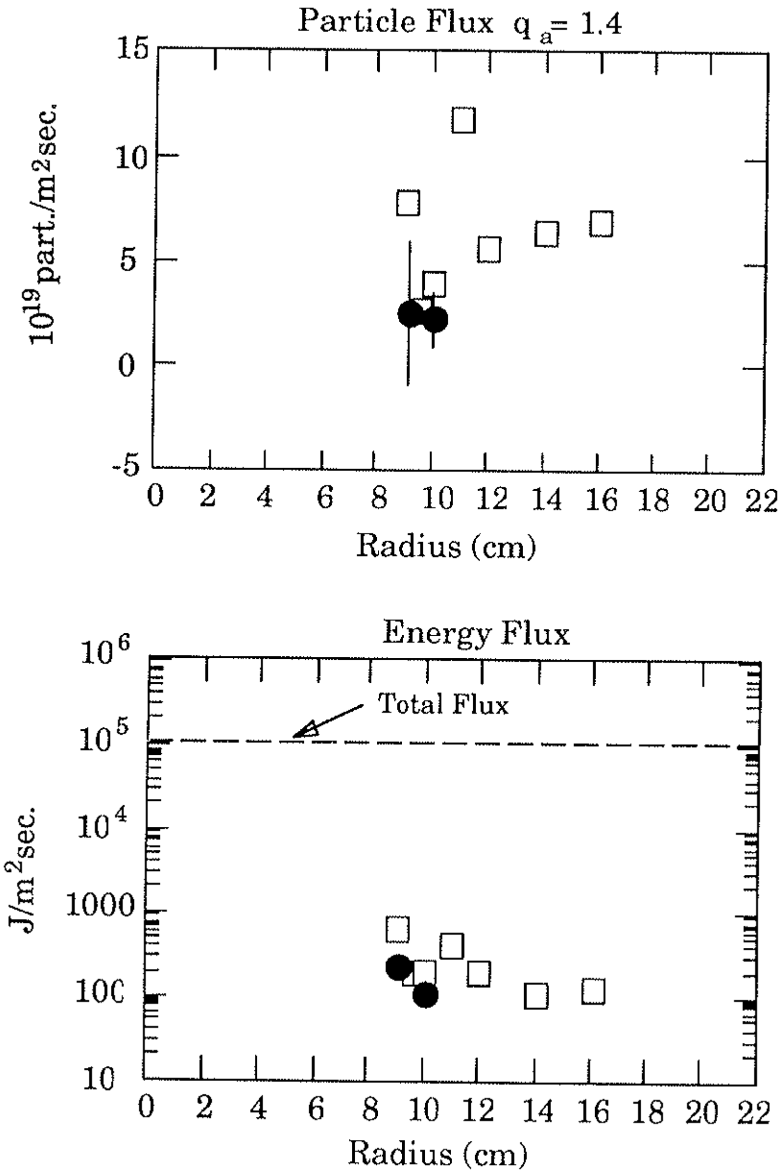

Fig. 5.10 Particle and energy flux profiles for <q(a)> = 1.4, outer limiter in. Also shown is the total energy flux.

References

1. Ritz, Ch. P., et al., J. Nuc. Mater. **145-147** (1987), 241

CHAPTER 6

Conclusions for $<q_a>$ Scaling and Limiter Effects on Electrostatic Turbulence in Tokapole-II

This chapter gives the summary and conclusions of the results described in Chapters 4 and 5. First a brief discussion will be made on the comparison of electrostatic and magnetic turbulence. The final conclusions are discussed next.

6.1 Comparison with Magnetic Fluctuation Measurements

A $<q_a>$ scan of magnetic turbulence was done on Tokapole-II for magnetically limited discharges by Dale Graessle.[1] It was demonstrated then, that for $<q_a> \leq 1$ the magnetic turbulence was large enough to account for the global energy confinement if a collisionless stochastic magnetic transport model was adopted. The magnetic turbulence decreased by a factor of 50 as $<q_a>$ was raised to 5.0. The energy confinement time due to magnetic turbulence is calculated from the measured magnetic fluctuations (fig. 7 of reference 1) and the corresponding energy fluxes was calculated and is compared with our electrostatic results in figure 6.1.

It can be seen that whereas for magnetic turbulence there is a strong dependence with $<q_a>$, there is no clear trend for the turbulence

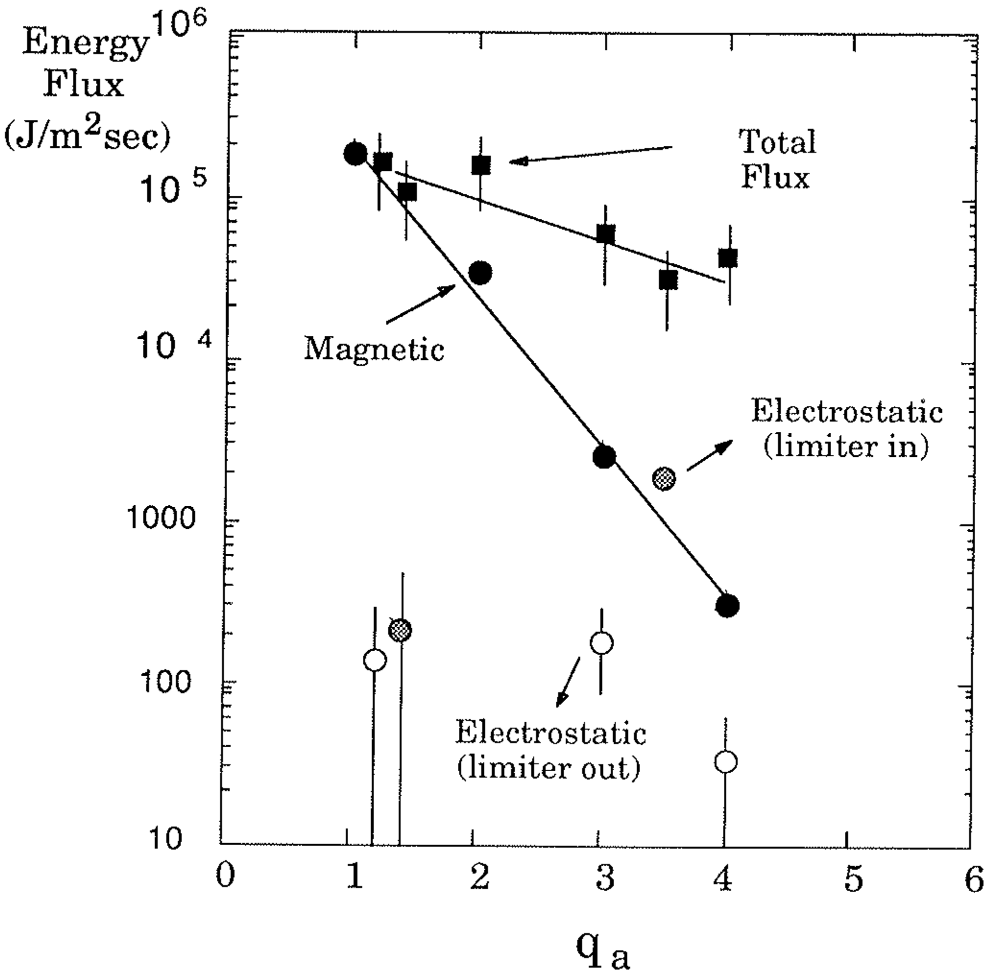

Fig. 6.1 Energy fluxes due to magnetic fluctuations (dark circles), electrostatic fluctuations with and without limiters (white and dashed circles), and the total energy fluxes (dark squares) calculated from the energy confinement times, as a function of <q(a)>.

in the electrostatic case. For the case with material limiter at high <qa>, the fluctuation induced flux does approach the actual value. The result for the "low <qa>" case with limiter in would suggest that the electrostatic turbulence would have the inverse behavior of the magnetic case, but the enhancement seen at high $<q_a>$ is actually due to a density gradient effect, rather than an effect of the magnetic configuration, which does not change with the limiter insertion. Therefore, we believe that the $<q_a>$ scaling results are valid for material limiters as well.

6.2 Summary and Conclusions

Electrostatic turbulence and its contribution to transport has been studied in Tokapole-II. In magnetically limited discharges the contribution of electrostatic turbulent transport in the edge and scrape-off regions is very small and certainly not responsible for the energy losses measured. The increase in turbulence and transport levels in material-limited discharges could suggest a dependence of transport on the presence of material limiters. However, low $<q_a>$ discharges do not show the same sensitivity to the limiter as high $<q_a>$ ones. The enhancement in the turbulence seems related to the gradient in the equilibrium densities which is affected by the limiter only in high $<q_a>$ discharges. The relative absence of electrostatically driven transport in magnetically limited discharges is thus probably due to the large scrape-off region in Tokapole-II which allows a gradual radial decrease of equilibrium quantities. In contrast, the plasmas in most machines are in close contact to a material limiter or a divertor plate, making the gradients very steep at the edge.

In many aspects the turbulence properties observed in Tokapole-II are similar to the observations made in the plasma interior of many tokamaks.[2] The low amplitudes observed in the plasma interior (~ 1%), low values of $k_\theta \rho_s$ (~ 0.05-1) with propagation in the electron diamagnetic direction, are also observed in Tokapole-II. Furthermore, the Boltzmann relation seems to hold in the plasma interior, and no clear correlation exists between $\tilde{n}/n$ and τ_E, although recent measurements in TEXT[3] indicate some agreement between fluxes calculated using a dissipative trapped electron model and equilibrium fluxes.

What causes transport in Tokapole-II remains an unanswered question. Since the frequencies measured were restricted to $f > 15$ kHz, global, MHD type modes are not being taken into account in this work. They are known to cause internal and external disruptions in Tokapole-II[4] (not always leading to current termination in the magnetic limiter case) and could contribute to transport. Fast electrons, which are more likely to be present in low $<q_a>$ discharges when the loop voltage is higher, could contribute to energy losses, via stochastic magnetic fields. Previous studies in impurity radiation losses in Tokapole, showed that it could only contribute with up to 30% of energy losses.[5]

In summary, two main conclusions emerge from this work. First, electrostatic turbulence is independent on the safety factor. Although the $<q_a>$ scaling was done only in magnetic limited discharges, it is likely that this is also true in material limiter cases, since the limiter does not affect the magnetic configuration. Second, the density gradient is responsible for electrostatic turbulence at the edge.

The presence of a material limiter in itself does not trigger electrostatic turbulence if the density gradient at the edge is allowed to slowly decay radially, as in a magnetic limiter configuration. This would explain the unique behavior of Tokapole-II compared to other machines, in which large density gradients cannot be removed.

References

1. Graessle, D. E., Prager, S. C., Dexter, R. N., Phys. Fluids B **3** (1991), 2626 . See also
   Graessle, D. E., Prager, S. C., Dexter, R. N., Phys. Rev. Lett. **62** (1989), 535

2. Wootton, A. J., et al., Phys. Fluids B **2** (1990), 2879

3. Bravenec, R. V., Abstracts of the 33rd Annual Meeting of the American Physical Society, Division of Plasma Physics, November, 1991 , Bulletin of the American Physical Society, vol 36, No. 9, p. 2348 October (1991).

4. Moyer, R. A., Ph.D. thesis University of Wisconsin-Madison (1988).

5. Groebner, R. J., Ph.D. thesis University of Wisconsin-Madison (1979).

CHAPTER 7

Small Spatial Scale Electrostatic Fluctuations in Tokapole-II

This chapter describes electrostatic fluctuations measured with a small spherical Langmuir probe, in order to investigate the possible existence of small spatial scale instabilities, which have been theoretically investigated and could contribute to anomalous transport. In order to differentiate the small-spatial-scale fluctuations, the power measured by the "small" probe is compared with the power of a nearby larger probe. It was found that for some cases they are indeed present in Tokapole-II although their contribution to transport is minimal. A brief review of the existent theoretical work on small scale instabilities, in particular η_e modes will be made, followed by the experimental results and conclusions of this chapter.

7.1 Motivation and Background

Small spatial scale instabilities (wavelengths on the order of the electron gyroradius) have been invoked by some authors to cause a significant amount of anomalous transport.[1-4] A good review of the available theories on these instabilities (called η_e instabilities) was made by Edward. J. Haines,[5] to whose thesis the reader is referred for a more complete description.

The electron confinement time in many tokamaks is known to scale linearly with density in the so-called Alcator scaling. In an attempt to explain this empirical scaling, Ohkawa[3] first proposed, based on simple arguments, that electromagnetic fluctuations with characteristic scale length $\delta = c/\omega_{pe}$ (the plasma collisionless skin depth, where c is the velocity of light and ω_{pe} is the plasma frequency) can lead to an electron thermal diffusivity $\chi_e \sim (c/\omega_{pe})^2 v_{the}/qR$ (here, v_{the} is the electron thermal velocity, q the safety factor and R is the major radius).

Nonlinear studies performed by Horton et all.,[6] showed that the source of this c/ω_{pe} turbulence may be a small spatial scale instability called the η_e mode.

Lee, Dong, Guzdar and Liu developed a linear theory for this instability which has wavelengths on the order of the electron gyroradius and are primarily electrostatic.[4] In a collisionless, sheared-slab model with finite beta, they treat the full electromagnetic character of the mode and find that the instability depends on the critical parameter:

$$\eta_e = \frac{d \ln T_e / dr}{d \ln n_e / dr} = \frac{L_n}{L_T}$$

where L_n and L_T are the density and temperature gradient scale lengths respectively. The modes are unstable at a threshold value of $\eta_e \sim 1$, becoming more unstable at larger values of η_e. Instability occurs at wavelengths between ρ_e and ρ_i (the electron and ion gyroradius respectively), in a wide range of frequencies below $0.3\omega^*_{ne}$ ($\omega^*_{ne} = k_y v_{the}^2/L_n\omega_{ce}$ is the electron diamagnetic drift frequency, where k_y is the poloidal wavenumber, v_{the} is the electron thermal speed, and ω_{ce} is the electron cyclotron frequency). The mode is localized in a narrow layer with a width of about an electron gyroradius (somewhat larger for magnetic perturbations). The magnetic character of the mode becomes important at finite beta, i.e. for $\beta_e >> m_e/m_i$.

Horton et al. studied the toroidal version of the linear mode,^{5} by adding ∇B and curvature drifts. The ions are assumed to be adiabatic ($\lambda_\perp << \rho_i$). The results show similar real frequencies and growth rates as the sheared-slab theory, with maximum growth at $\lambda \sim \rho_e$, but with a threshold value of $\eta_e = 2/3$.

The only nonlinear work performed to date on η_e mode turbulence was done by Horton and co-workers,$^{6\text{-}7}$ in a numerical solution of a set of hydrodynamic equations (using the electron continuity equation, parallel force balance and energy conservation), assuming adiabatic ions and toroidal effects (∇B and curvature drifts). Dominant nonlinear terms come from $\tilde{B}.\nabla$ due to field line perturbations and the ExB convective derivative ($\partial/\partial t$ + v.∇ with v = v_{ExB}) acting on fluctuating quantities. The perturbed scalar potentials $\tilde{\Phi}$ and $\tilde{A}$, and the temperature fluctuations $\tilde{T}_e$ as well as the their corresponding energies are solved, and their evolution from the linear growth phase to saturation is followed. During the linear growth phase, dominant modes have $k_z = 0$ (z is the direction parallel to the magnetic field) and $k_y\rho_{ei} \sim 0.8$ (ρ_{ei} is the electron gyroradius with the ion temperature), and are primarily electrostatic. In the steady state, the small random magnetic fluctuations evolved into larger structures. The turbulence is isotropic and dominated by $k_y\rho_{ei} \sim 0.05$ to 0.1 (for $\beta = 1\%$), with the peak of the k-spectra at $k_{min} \sim \omega_{pe}/c$ which is the largest scale permitted by the simulation grid. Figure 7.1 shows the contours of electrostatic potential, magnetic flux function and electron temperature fluctuations at the linear phase (a) and steady state (b-d).[6] Note that at steady state, the electric potential perturbations are slightly smaller in size than the c/ω_{pe} dimension of the magnetic perturbations.

The numerical code used by Horton to solve the eigenfunctions $\tilde{\Phi}$ and $\tilde{A}$, was modified by E. Haines to accommodate Tokapole-II parameters. Figure 7.2 shows the results for the maximum growth rates and their corresponding real frequencies. The maximum growth rate for a $k_z = 0$ case occurs at $k_x = 0$ and $k_y\rho_{ei} \sim 0.5$ which corresponds to $\lambda = 0.4$ mm. The range of frequencies corresponding to positive growth is very broad, and for the $k_y\rho_{ei} = 0$ and 0.25 cases it extends from 200 kHz to 22 MHz, with peak growths occurring between 4 MHz and 6 MHz.[2]

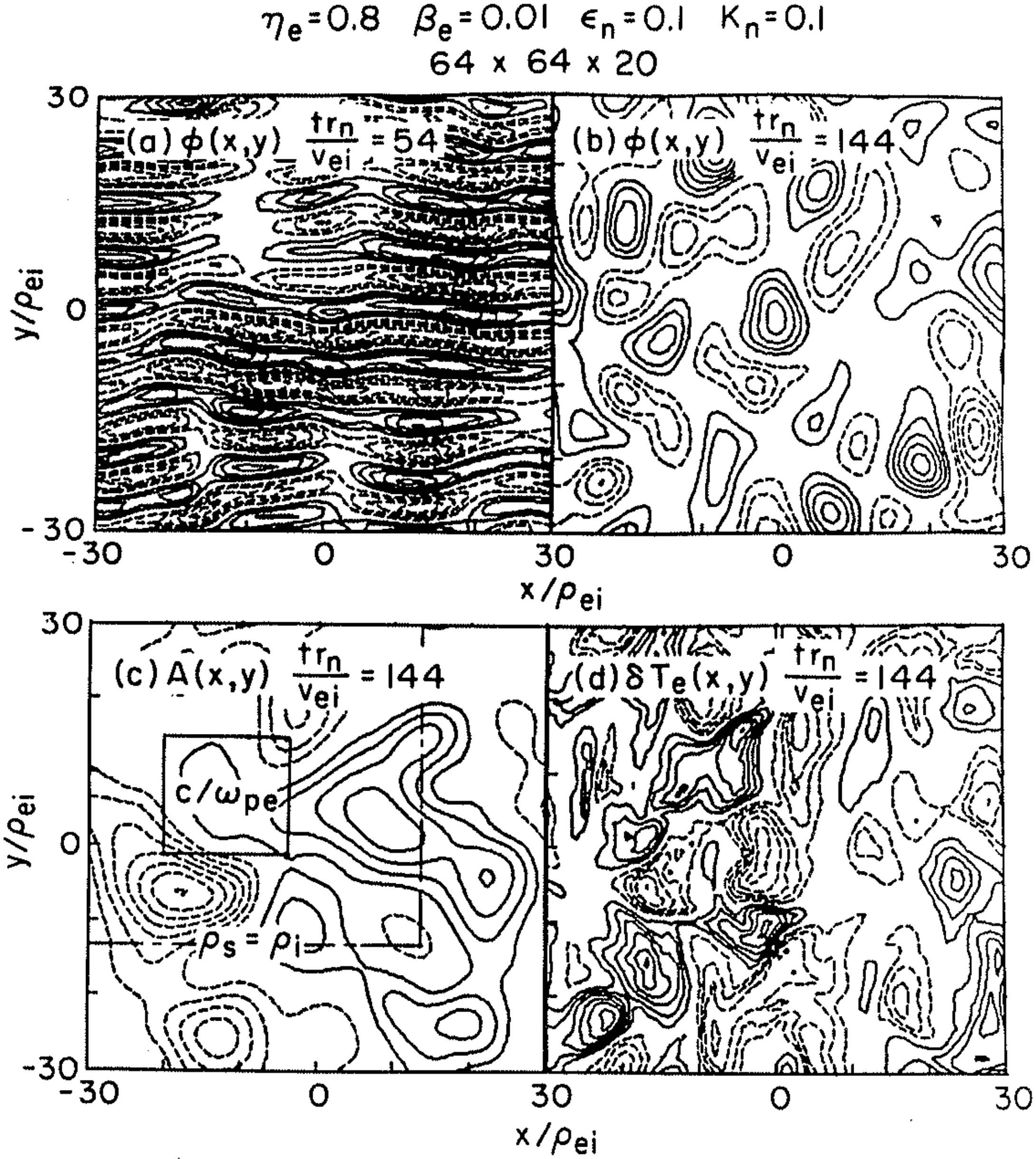

Fig. 7.1 Contours of electrostatic potential, magnetic flux function and electron temperature perturbations at the linear phase (a), and at steady state (b-d).

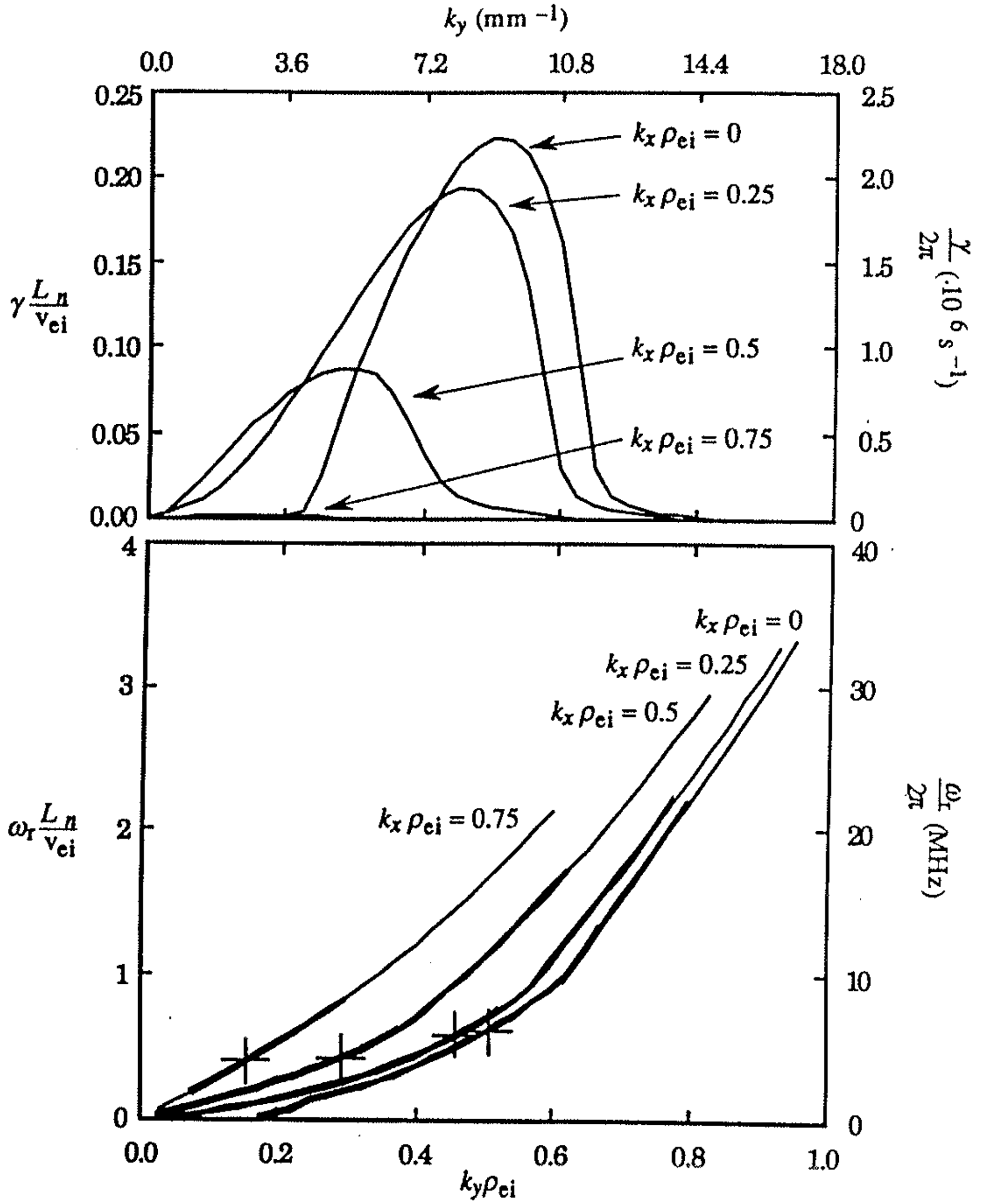

Fig. 7.2 Maximum linear growth rates (a) and real frequencies (b) computed for Tokapole-II parameters with $k_z = 0$. Crosses mark the frequencies corresponding to peaks of the maximum growth rate curves.

7.2 The "Small" Langmuir Probe

For Tokapole-II's edge parameters: T_e = (10-40) eV, B_T = (3-5) kGauss and n_e = (0.5-2.5)x10^{13} cm^{-3}. This will give: ρ_e = (2-7)x10^{-2} mm, ρ_i = (0.9-3) mm (assuming $T_i = T_e$ in the edge) and c/f_{pe} = (6-15) mm.

To resolve electrostatic fluctuations with small wavelengths, a spherical Langmuir probe 0.5 mm in diameter was constructed. Two sets of probes were built (described in Chapter 3). In one set (probe set # 1), the fluctuation power of the spherical tip was compared with those of two "large" cylindrical tips 3 mm in length and 0.4 mm in diameter oriented in the radial and poloidal directions. This arrangement allows us to distinguish fluctuations with small spatial scales (with wavelengths $\lambda \geq 1$ mm) from fluctuations with larger scales ($\lambda \geq 6$ mm) in the radial and poloidal directions.

In the second set (probe set # 2) the "small" spherical tip is compared with a "large" cylindrical tip 3 mm in length and an even larger cylindrical tip 1 cm in length both oriented in the radial direction. This probe set was built to extend the range of spatial scales that could be studied: the very large tip can only detect wavelengths larger than 2 cm.

7.3 Experimental Results

The results that will be presented were obtained in two run periods. On the first run, high $<q_a>$ discharges were studied, and probe set # 1 was used with high frequencies covering the range of 500 kHz to 1.5 MHz. Due to aliasing problems and the rapid power decay with frequency of the low frequency fluctuations, there was a gap between the high and low frequency ranges which was not resolved. A band-pass filter of 300 kHz to 1.5 MHz was therefore built and used with probe set # 2 to study low $<q_a>$ discharges.

7.3.1 Small Spatial Scales in High q_a Discharges

The high $<q_a>$ discharges that were investigated are very similar to the magnetic limiter high $<q_a>$ case described in Chapter 4 (a $<q_a> = 3.5$ discharge was used). A probe set with a small spherical tip (0.5 mm diameter) and two cylindrical tips (3 mm in length) oriented in the radial and poloidal directions (probe set # 1), was used to measure the power of ion saturation fluctuations at different radii.

The amplitude spectra measured by the three probes at different radii are shown in figures 7.3 and 7.4 for low (10 kHz to 500 kHz) and high (500 kHz to 1.5 MHz) frequencies respectively. No enhancement is seen at low frequencies in any position, while at high frequencies, the "small" probe measures significantly more power than the "large" ones in the scrape-off region, but not in the edge region. An enhancement of a factor of 4 in amplitude is seen at $r = 12$ cm. Note that in these cases there is no difference in the amplitudes measured by the large probes oriented in the radial and poloidal directions, indicating that the turbulence is perpendicularly isotropic. In some cases however, the

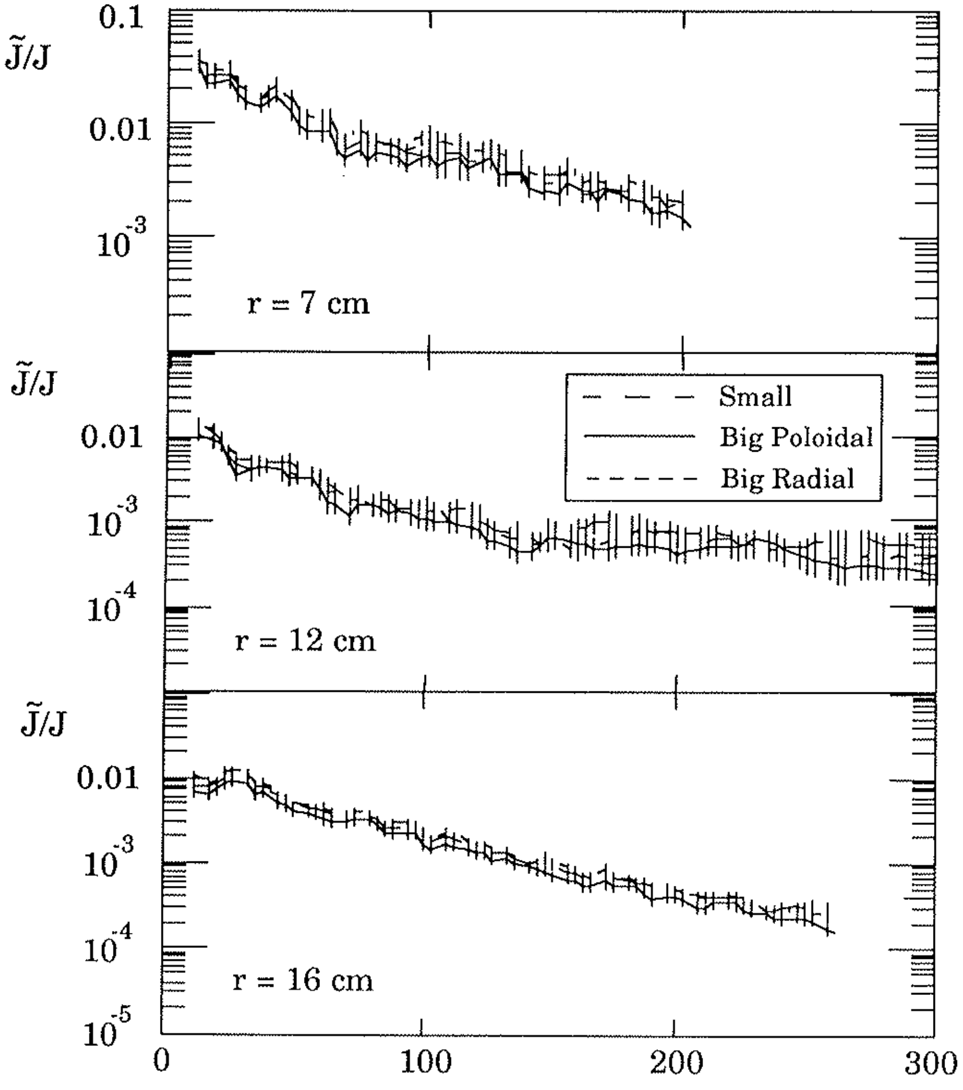

Fig. 7.3 Ion saturation current fluctuation amplitude spectra for the small (0.5 mm), big poloidal and big radial (3 mm) tips, at various positions at low frequencies, <q(a)> = 3.5.

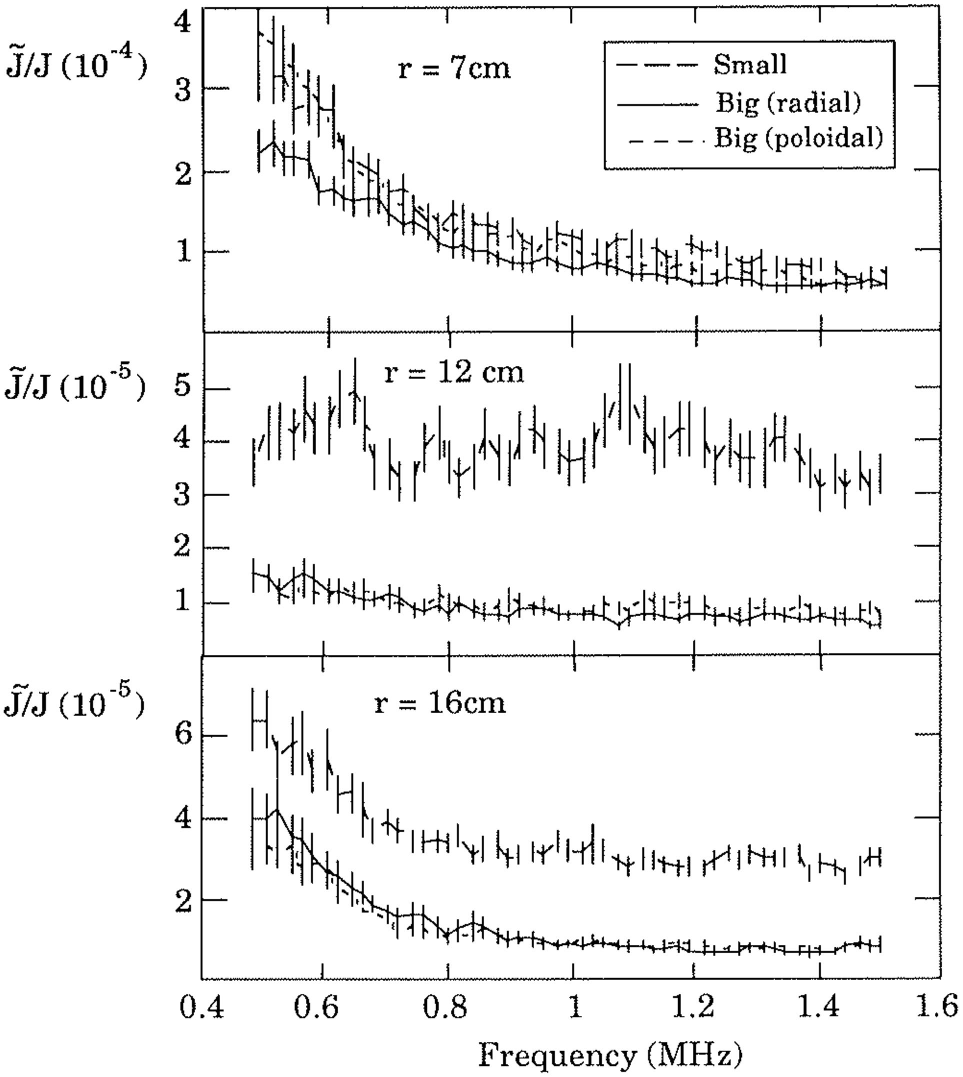

Fig. 7.4 Fluctuation level amplitude spectra for various positions <q(a)> = 3.5, high frequency range, for: small (0.5mm), big radial (3mm) and big poloidal (3mm) tips.

radial probe measures larger amplitudes than the poloidal probe by up to about a factor of two in amplitude.

Figures 7.5 and 7.6 show the frequency integrated fluctuation level profiles and the ratio between the integrated "small"/"large" amplitudes at the various radii, for low and high frequency ranges. Fluctuation levels are very small at high frequencies (in the 10^{-4} range), and should not contribute much to transport. Mixing level estimates would give $\tilde{p}/p = 1/(kL_p) \geq 3\%$ for the 3 mm probe (assuming $L_p \sim 3$ cm and $k \leq 2\pi/0.6\ \mathrm{cm}^{-1}$).

Figure 7.7 shows the distribution of fluctuation power in k space for the largest enhancement which occurred at r = 12 cm at high frequencies. The area of each bin in the histogram corresponds to the power in the corresponding k-band, with heights normalized to the height of the first bin. The area in the first bin corresponds to the power measured by the large probe (i.e., for wavelengths larger than 6 mm). The area of the second bin represents the extra power measured by the small probe, i.e., it is the difference between the power measured by the small and the large probes, corresponding to wavelengths between 1 mm and 6 mm. Wavelengths corresponding to ω_{pe}/c and $2\pi/\rho_i$ are indicated in the figure for the plasma parameters at r = 12 cm. It is seen that there is a peak in power at the larger k band, which includes ρ_i scale instabilities but not c/ω_{pe} scales (which lies in the first k band).

Figure 7.8 shows the raw data for high frequency fluctuations detected by the three probes and the SXR signal for r = 12 cm. It is seen that the fluctuations measured by the "large" probes have bursts of

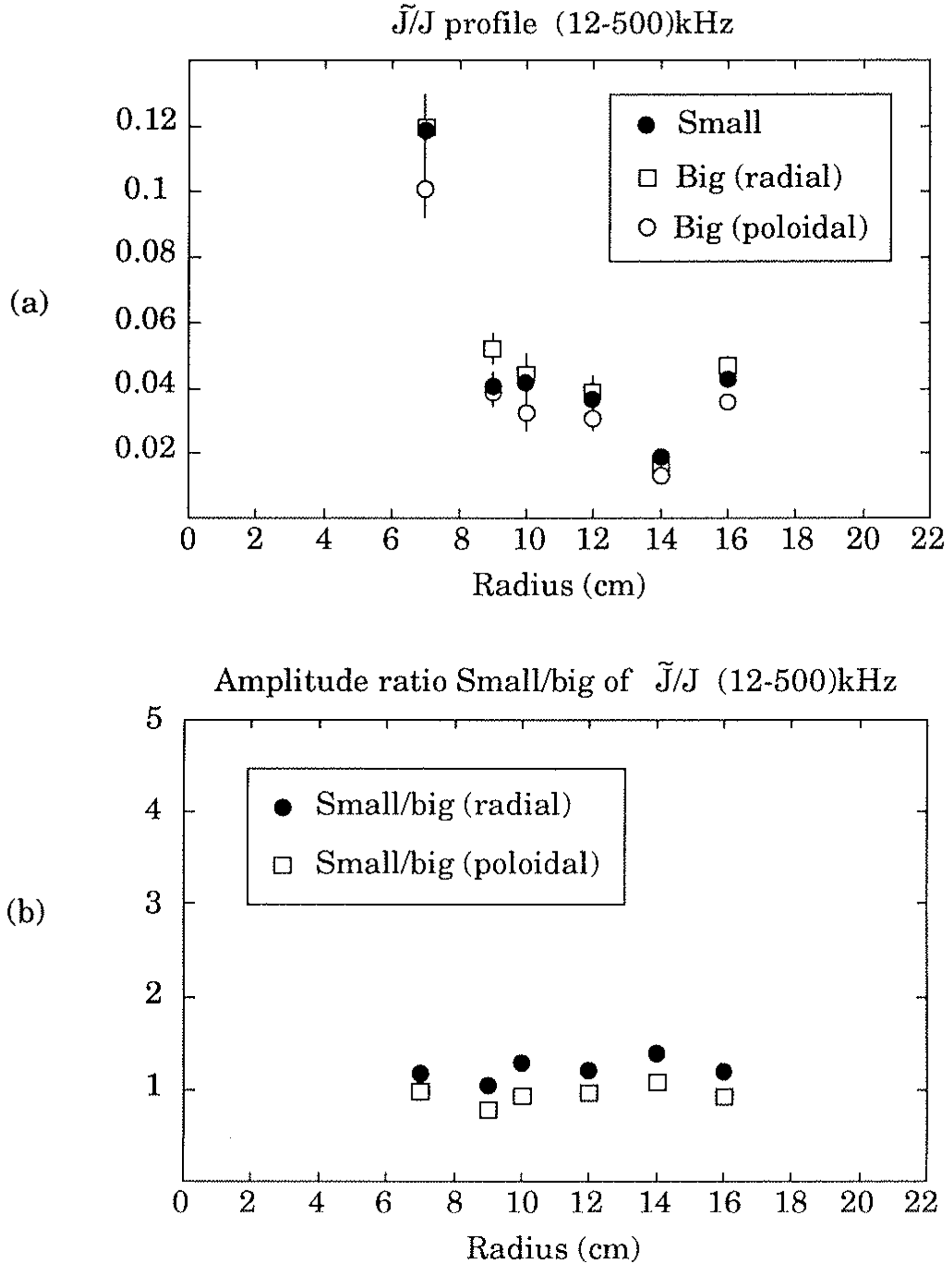

Fig. 7.5 (a) Fluctuation amplitude profile (12-500) kHz for the three tips for $<q(a)> = 3.5$. (b) Ratio of amplitudes between small (0.5 mm), big (3 mm) radial and big (3 mm) poloidal probes.

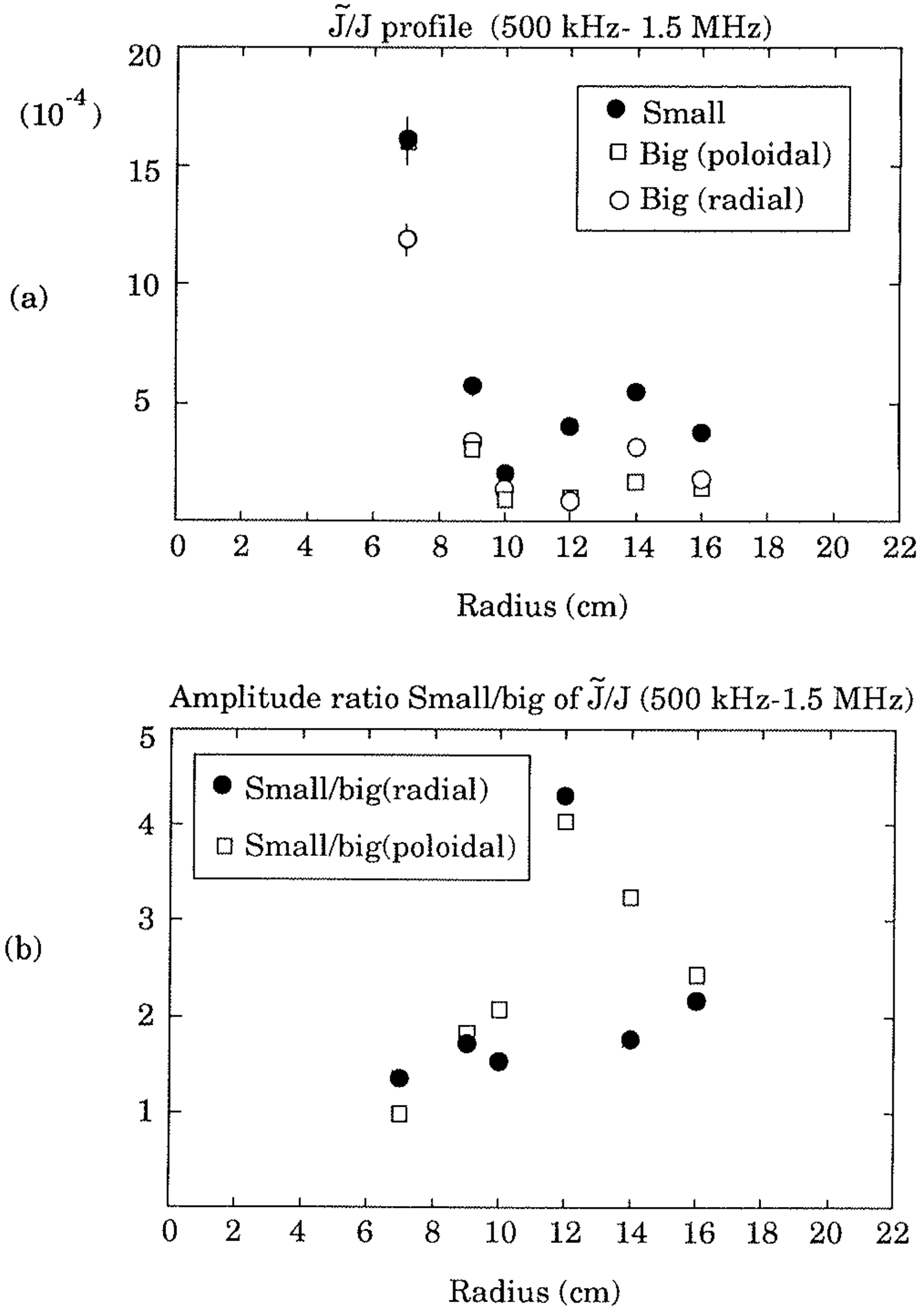

Fig. 7.6 (a) Fluctuation Amplitude profile (500 kHz to 1.5 MHz) for the three tips for <q(a)> = 3.5. (b) Ratio of amplitudes between small (0.5 mm), big (3 mm) radial and poloidal probes.

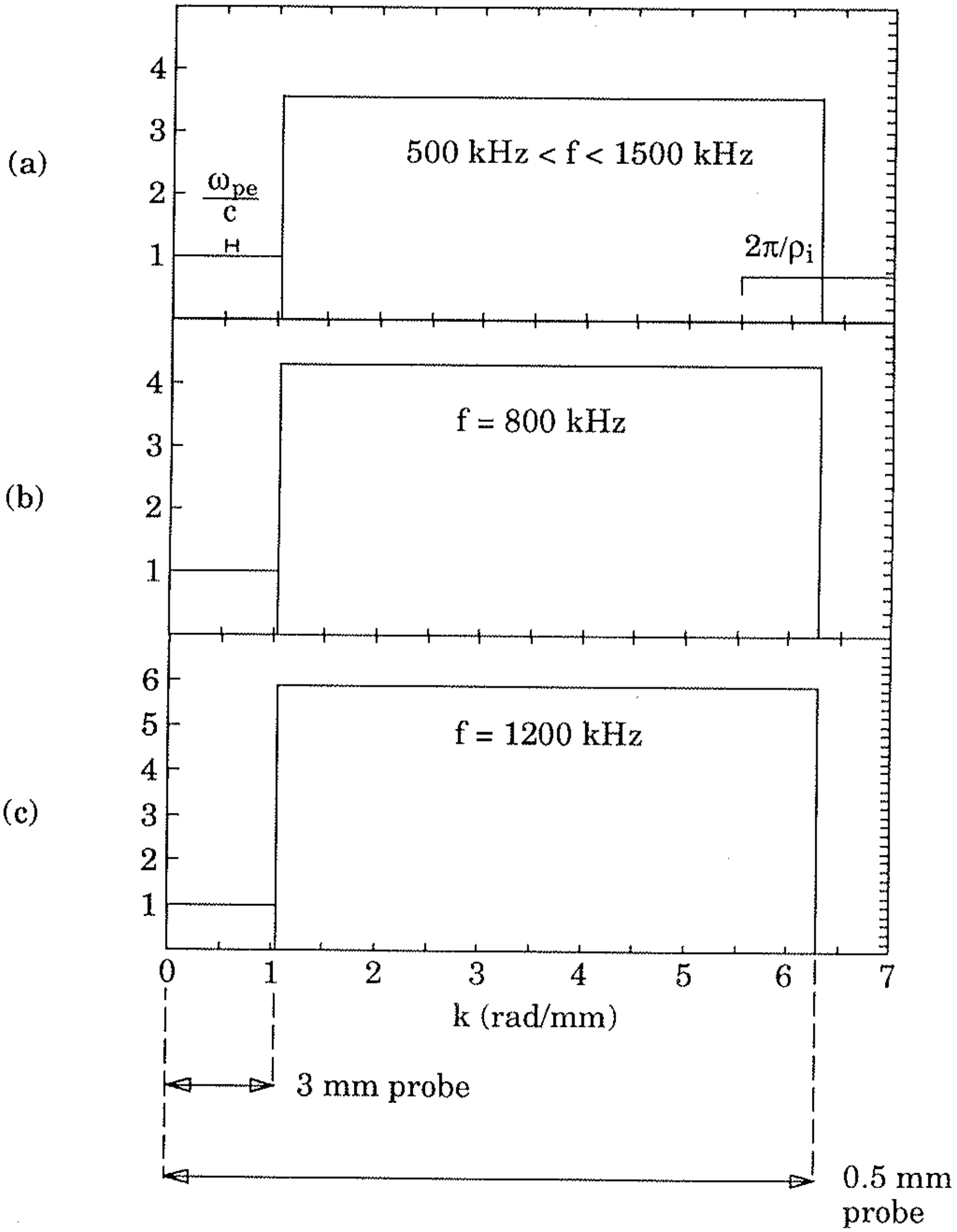

Fig. 7.7 Normalized fluctuation power as a function of radial wavenumber, for <q(a)> = 3.5, r = 12 cm, (a) for the integrated power from 500 kHz to 1.5 MHz, (b) for f = 800 kHz and (c) for f = 1.2 MHz.

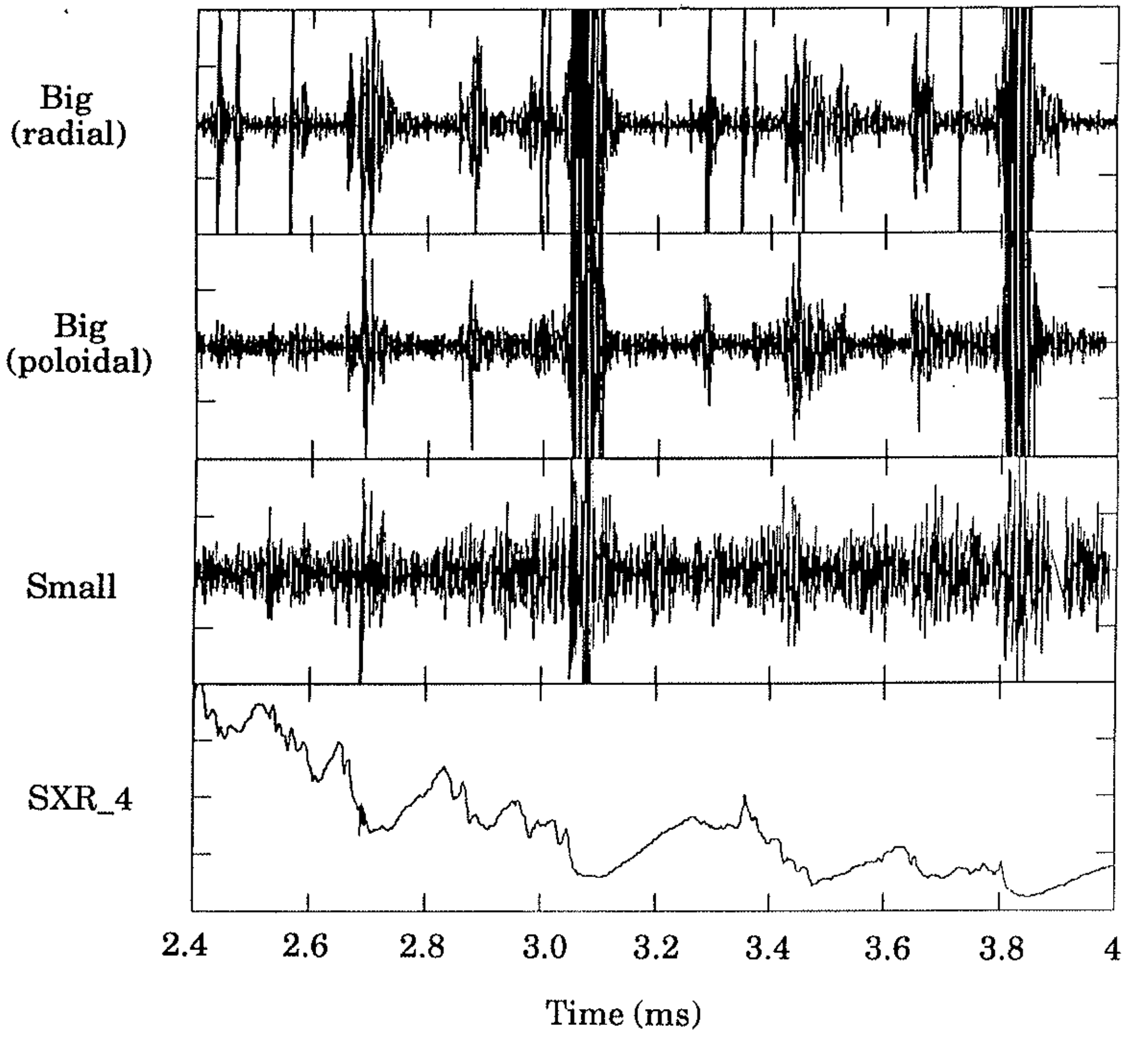

Fig. 7.8 Ion saturation current fluctuations for the three probes (a-c) and Soft X-ray signal (d). Bursts of activity during SXR crashes are not as accentuated in the small probe signal.

activity that correspond to small crashes in the SXR signals. Note that the small probe does not seem to be as sensitive to the same bursts, because during the "quiet" parts it is actually detecting more power than the large probes. The high frequency results just presented were taken during these "quiet" parts of the discharge. A comparison of the spectra

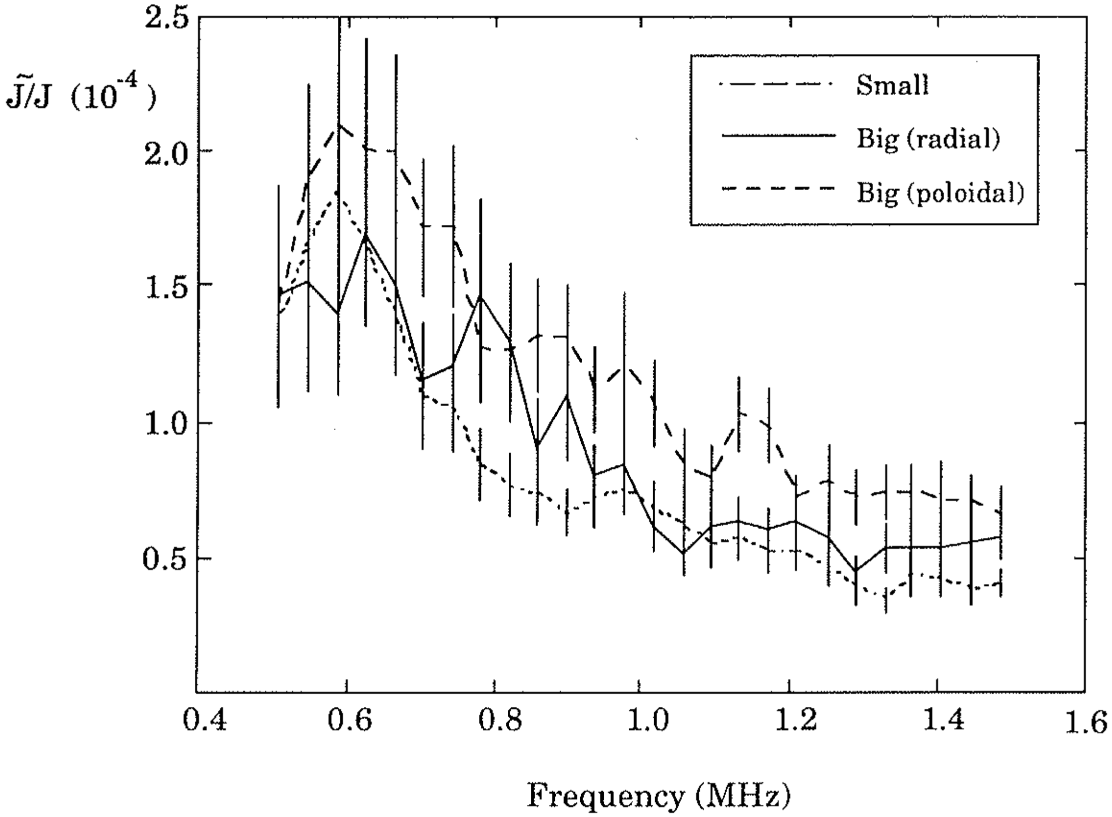

Fig. 7.9 Fluctuation amplitude spectra for the three tips at <q(a)>= 3.5, r = 12 cm, bursts only.

detected by the three probes during the bursts of activity (figure 7.9) shows no enhancement at all, as we could expect for sawteeth related phenomena which are dominated by large MHD type fluctuations.

Although electron temperature and density profiles were not measured during this run, similar discharges have profiles as shown in figure 7.10. A reliable calculation of η_e is difficult due to the large uncertainties involved in taking the ratio of two derivative quantities.

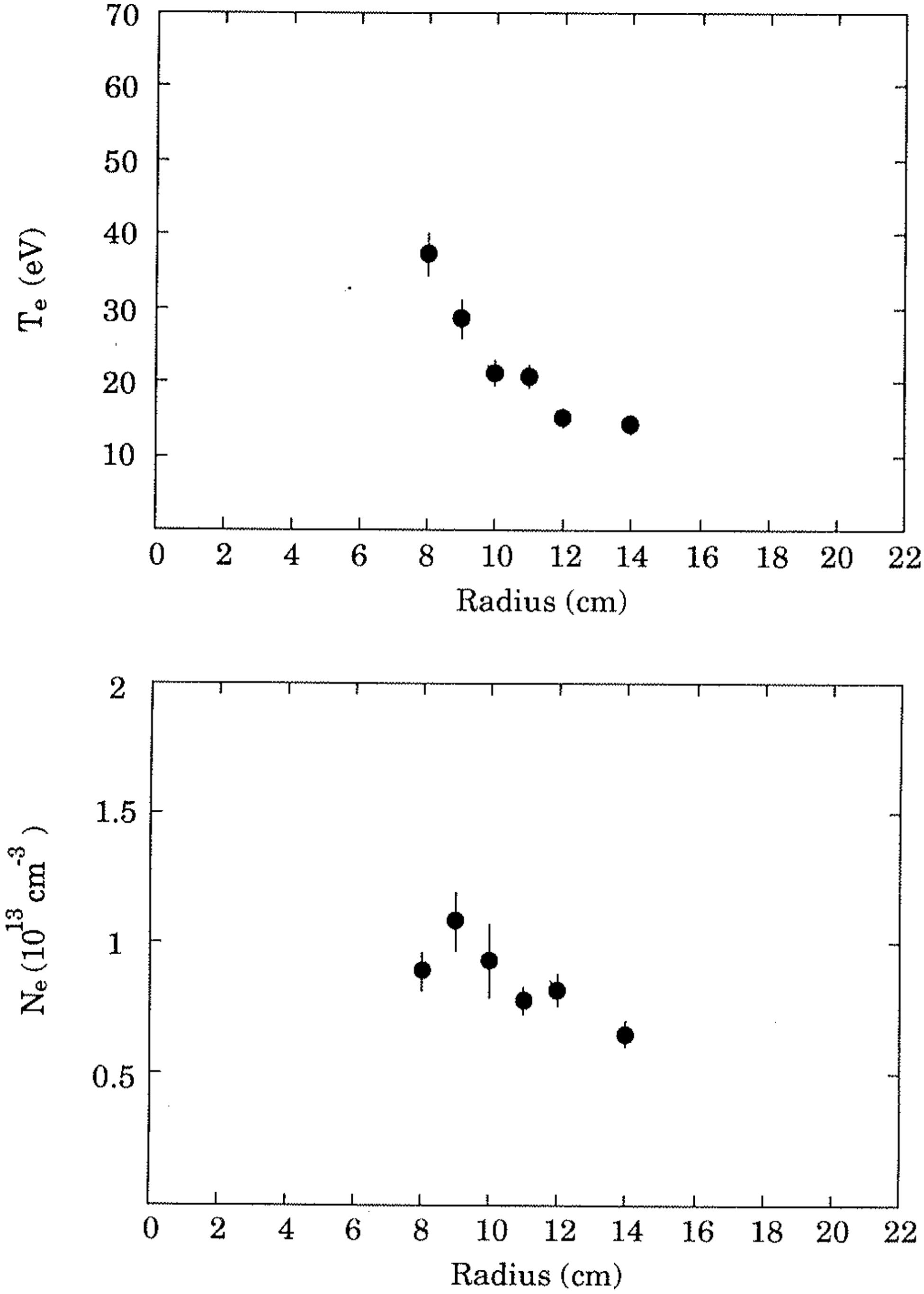

Fig. 7.10 Electron temperature and density profiles for $\langle q(a)\rangle = 3.5$. $\eta e \sim 2$

However we can roughly estimate that η_e is of order unity ($\eta_e \sim 2$) in this case ($L_n \sim 10$ cm and $L_T \sim 5$ cm).

7.3.2 Small Spatial Scales in Low q_a Discharges

The low $<q_a>$ discharges in which the data presented here were taken are also similar to the low $<q_a>$ magnetic limited discharges of chapter 4. The fluctuation data however were taken before the peak of the SXR, when $<q_a>$ was flat in time. For this run, a different set of probes was built, with two large probes oriented in the radial direction, one 3 mm long ("large") and the other 1 cm long ("very large"). The high frequency band-pass filters were also changed so that 300 kHz $< f <$ 1.5 MHz.

Figures 7.11 and 7.12 show the fluctuation amplitude spectra of the three probes at different radii for low and high frequency ranges. As in the high $<q_a>$ case no differences are seen in low frequencies between "small" and "large" probes. At high frequencies, the "small" probe measures a larger amplitude at $r = 12$ cm and $r = 16$ cm.

For $r = 12$ cm (highest enhancement), the distribution of fluctuation power with k is shown in figure 7.13. With three different probe sizes, the power can be distributed in 3 k-bands. At lower frequencies (400 kHz) there is no extra power at the largest k band (which contains $2\pi/\rho_i$ wavelengths), but some power exists in the second band, which includes c/ω_{pe} scales. The differences increase at higher frequencies, and at 800 kHz there is power in the largest k band and even

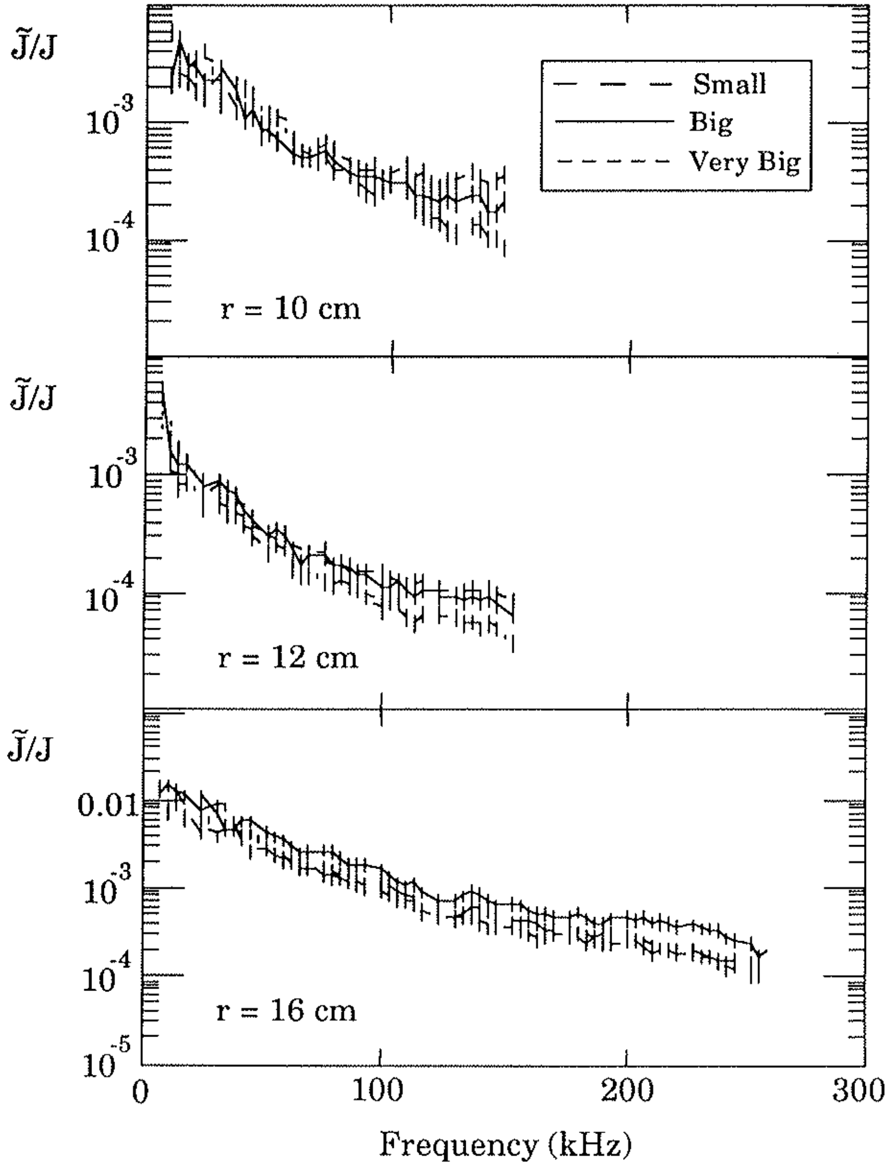

Fig. 7.11 Fluctuation amplitude spectra for small (0.5 mm), big (3 mm) and very big (1 cm) tips, at various positions at low frequencies, <q(a)> = 1.4.

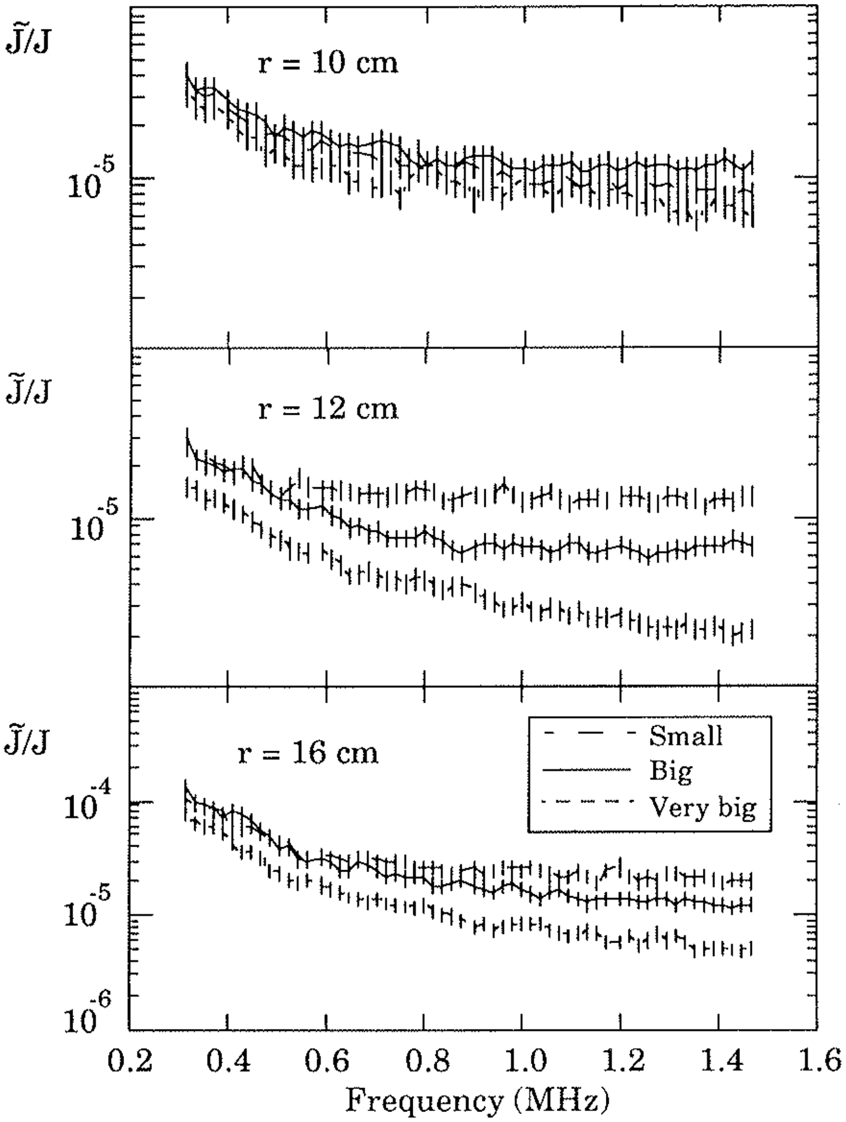

Fig. 7.12 Fluctuation amplitude spectra for small (0.5 mm), big (3 mm) and very big (1 cm) tips, at various positions, <q(a)> = 1.4, high frequency range.

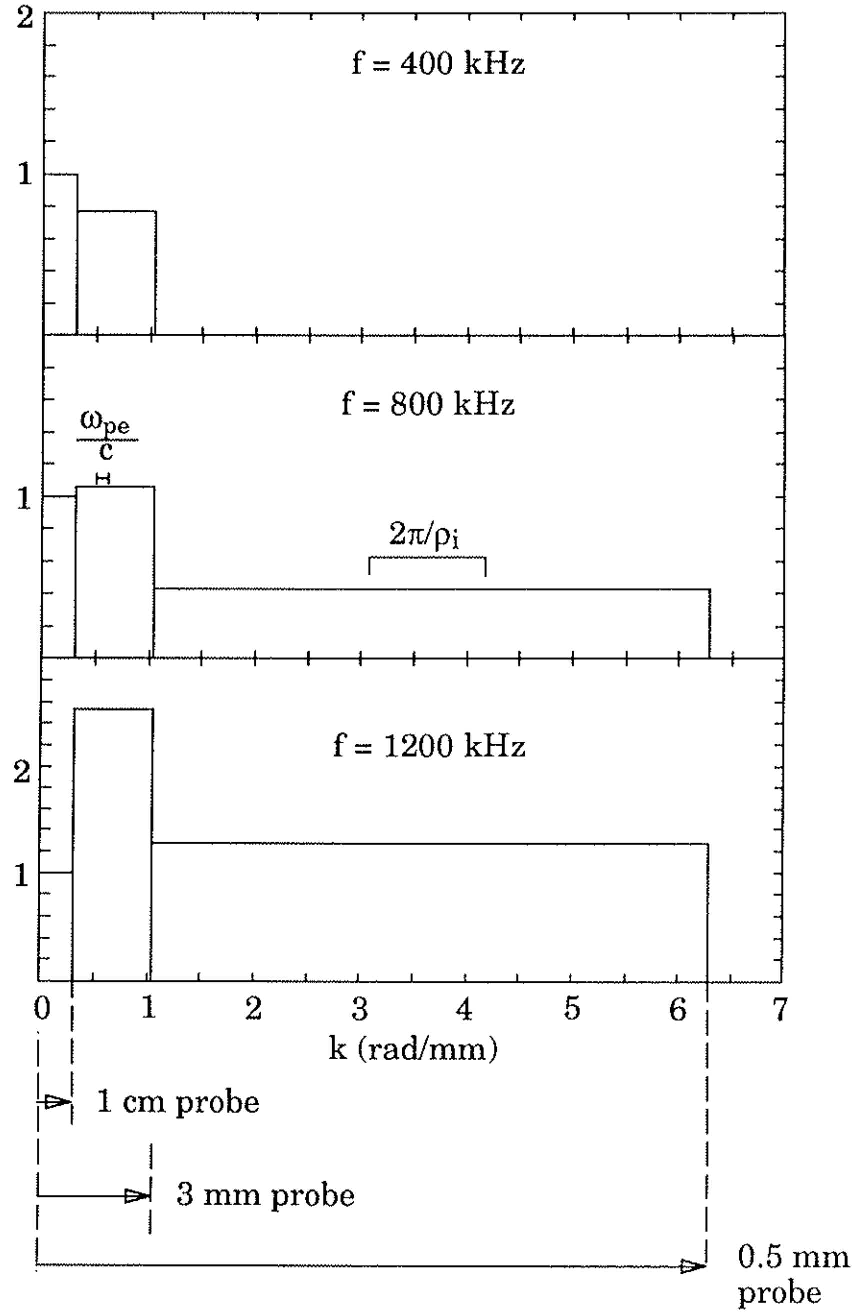

Fig. 7.13 Normalized fluctuation power as a function of radial wavenumber for <q(a)> = 1.4, r = 12 cm, for various frequencies. Power is normalized to the first bin.

more power at the second band . The peak in power at the second band increases at 1.2 MHz.

Figures 7.14 and 7.15 show the frequency integrated fluctuation level profiles and ratios between the amplitudes of "small" and "big" and "small" and "very big" probes, for both frequency ranges. Again, high frequency fluctuations are small and should not contribute to transport. At these frequencies, fluctuation amplitudes are small compared to mixing level estimates, which would give $\tilde{p}/p = 1/(kL_p) \geq$ (3-6) $x10^{-3}$ for the 3 mm probe and $\tilde{p}/p \geq (0.5\text{-}1.0)x10^{-3}$ for the 0.5 mm probe.

The electron temperature and density profiles were measured during this run and are shown in figure 7.16. We can see that low $<q_a>$ discharges have flatter profiles, and in this case $\eta_e \sim (0.3\text{-}0.5)$ in the scrape-off region ($r \sim 14$ cm, where $L_n \sim 9$ cm and $L_T \sim (18\text{-}30)$ cm) while in the edge it tends to diverge due to the very flat density profile.

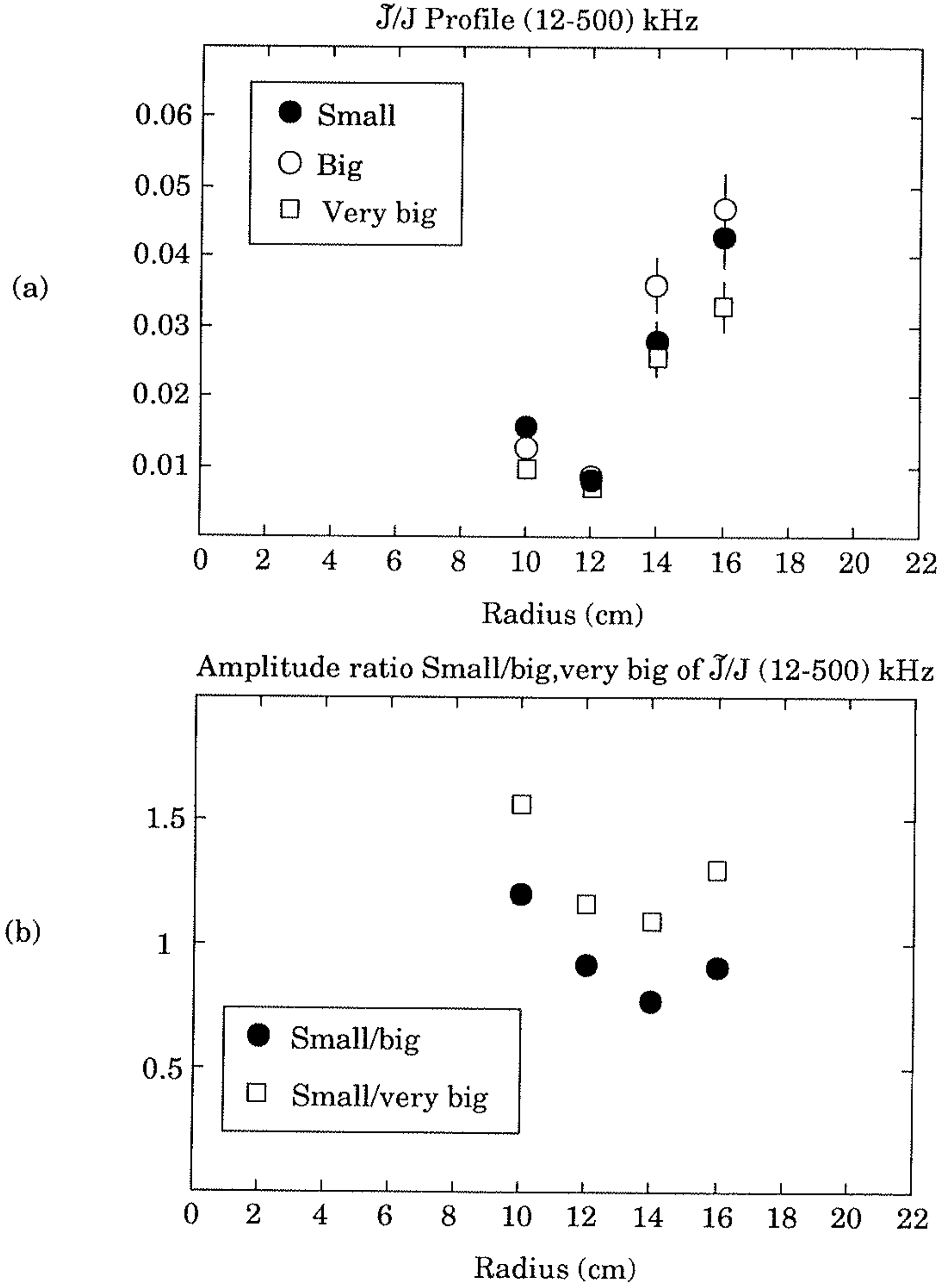

Fig.7.14 (a) Fluctuation amplitude profile (12-500) kHz for <q(a)> = 1.4 for the three tips. (b) Ratio of ampltiudes between small (0.5 mm), big (3 mm) and very big (1 cm) tips.

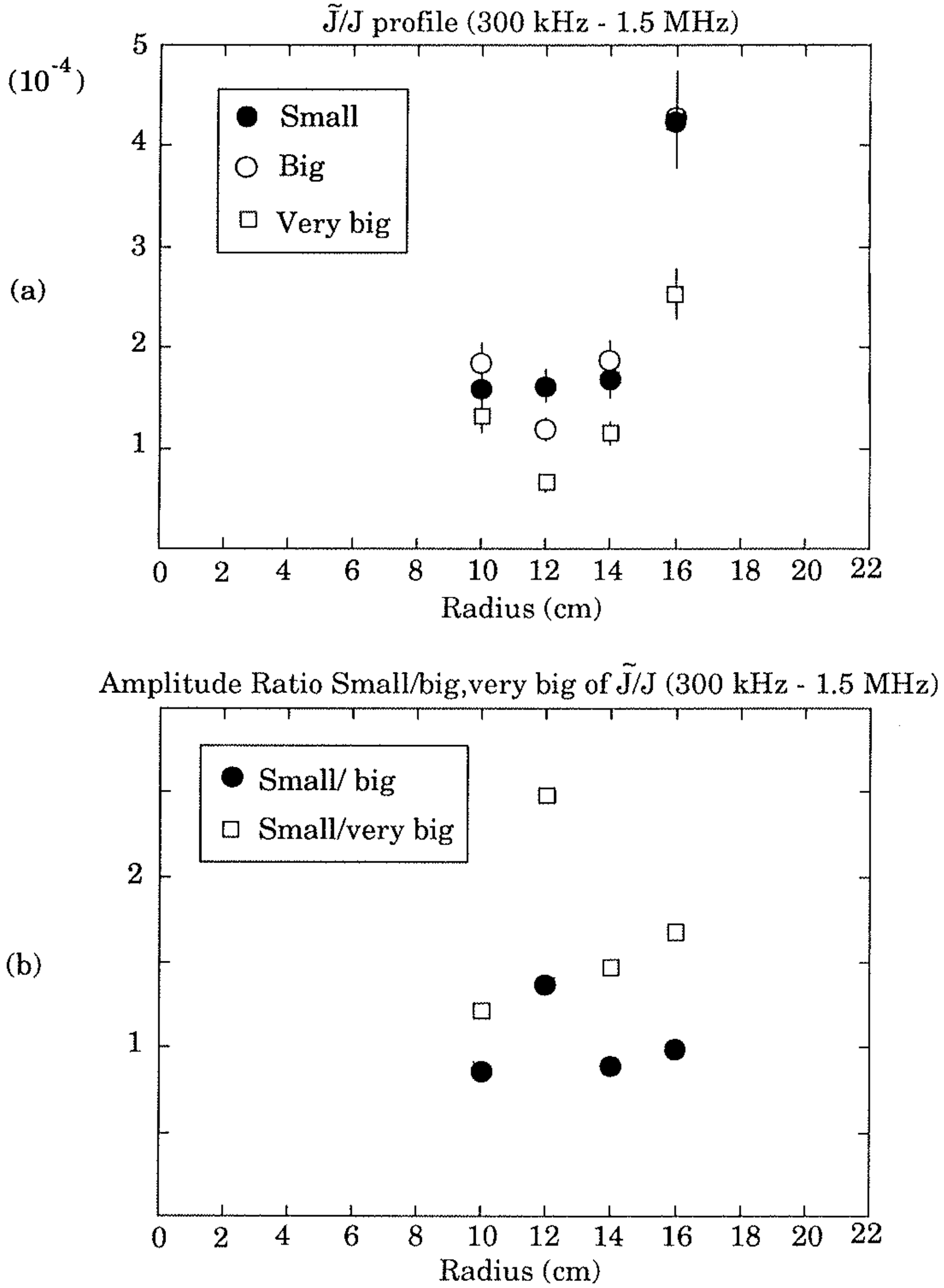

Fig. 7.15 (a) Fluctuation amplitude profile for the three tips, at <q(a)> = 1.4 from 300 kHz to 1 MHz. (b) Ratio of amplitudes between small (0.5 mm), big (3 mm) and very big (1 cm) tips.

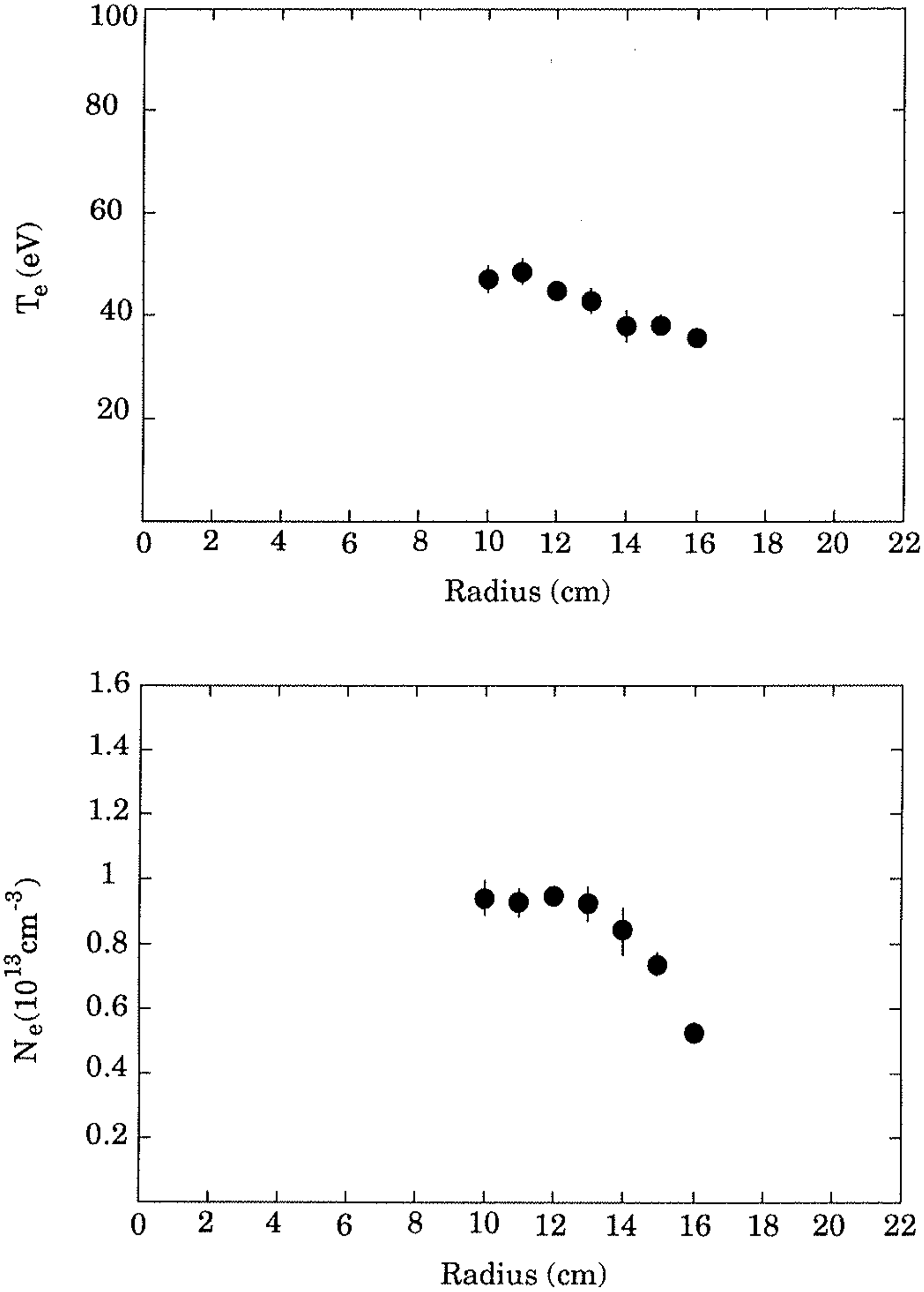

Fig. 7.16 Electron temperature and density profiles at t = 1.5 ms for <q(a)> = 1.4.

7.4 Conclusions

Small spatial scale electrostatic fluctuations have been detected in Tokapole-II. By comparing the power of different size probes, it has been found that an enhancement in power occurs for smaller probes in the scrape-off region at high frequencies ($300\ \text{kHz} < f < 1.5\ \text{MHz}$).

The enhancement is bigger at high $<q_a>$ discharges, where differences of up to a factor of 4 in amplitude were found between a 0.5 mm spherical probe and a 3 mm cylindrical one. This enhancement occurs at scales smaller than c/ω_{pe}, possibly including ρ_i scale instabilities. In low $<q_a>$ discharges the spherical 0.5 mm probe measures up to 20% more amplitude than the cylindrical 3 mm one, and up to 2.5 times more than a 1 cm cylindrical probe. With three different probe sizes it was possible to see that there is power at both c/ω_{pe} and smaller (ρ_i) scales.

In both $<q_a>$ cases, the fluctuation levels due to small scales were still too small compared with mixing length estimates, and certainly too small for transport, since the amplitude enhancements occur only at high frequencies where $\tilde{J}/J$ is in the 10^{-4} range.

Comparison with studies of small spatial scale magnetic fluctuations,[5] show that in that case the enhancement in power for smaller probes, occur at low $<q_a>$ discharges, and inside the separatrix, where β is largest, unlike the electrostatic case. This is consistent with the theoretical prediction that the magnetic component of microturbulence becomes more important as β increases.

References

1. Guzdar, P. N., Liu, C. S., Dong, J.Q., Lee, Y. C., Phys. Rev. Lett. **57** (1986), 2818
2. Ohkawa, T., Phys. Rev. Lett., **67A** (1978), 35
3. Lee, Y. C., Dong, J.Q., Guzdar, P. N., Liu, C. S., Phys, Fluids **30** (1987), 1331
4. Horton, W., Hong, B. G., Phys. Fluids **31** (1988), 2971
5. E. J. Haines, Ph. D. Thesis, University of Wisconsin-Madison (1991)
6. Horton, W., Hong, B. G., Tajima, T., Comments on Plasma Physics and Controlled Fusion **E 13** (4) (1990), 207
7. Bekki, N., Horton, W., Hong, B. G., Tajima, T., Institute for Fusion Studies Report # 264, University of Texas-Austin (February 1989)